

# Mechanical characterization of glassy polymers using instrumented indentation

**Citation for published version (APA):**

Pelletier, C. G. N. (2008). *Mechanical characterization of glassy polymers using instrumented indentation*. [Phd Thesis 1 (Research TU/e / Graduation TU/e), Mechanical Engineering]. Technische Universiteit Eindhoven. <https://doi.org/10.6100/IR632047>

**DOI:**

[10.6100/IR632047](https://doi.org/10.6100/IR632047)

**Document status and date:**

Published: 01/01/2008

**Document Version:**

Publisher's PDF, also known as Version of Record (includes final page, issue and volume numbers)

**Please check the document version of this publication:**

- A submitted manuscript is the version of the article upon submission and before peer-review. There can be important differences between the submitted version and the official published version of record. People interested in the research are advised to contact the author for the final version of the publication, or visit the DOI to the publisher's website.
- The final author version and the galley proof are versions of the publication after peer review.
- The final published version features the final layout of the paper including the volume, issue and page numbers.

[Link to publication](#)

**General rights**

Copyright and moral rights for the publications made accessible in the public portal are retained by the authors and/or other copyright owners and it is a condition of accessing publications that users recognise and abide by the legal requirements associated with these rights.

- Users may download and print one copy of any publication from the public portal for the purpose of private study or research.
- You may not further distribute the material or use it for any profit-making activity or commercial gain
- You may freely distribute the URL identifying the publication in the public portal.

If the publication is distributed under the terms of Article 25fa of the Dutch Copyright Act, indicated by the "Taverne" license above, please follow below link for the End User Agreement:

[www.tue.nl/taverne](http://www.tue.nl/taverne)

**Take down policy**

If you believe that this document breaches copyright please contact us at:

[openaccess@tue.nl](mailto:openaccess@tue.nl)

providing details and we will investigate your claim.

**Mechanical Characterization  
of Glassy Polymers  
using Instrumented Indentation**

Pelletier, Christophe G.N.

Mechanical Characterization of Glassy Polymers using Instrumented Indentation

Eindhoven: Eindhoven University Technology, 2008.

A catalogue record is available from the Eindhoven University of Technology Library.

ISBN: 978-90-386-1196-9

Reproduction: University Press Facilities, Eindhoven, The Netherlands

Cover design: Christophe G.N. Pelletier

Cover illustration: optical picture of a residual indentation print

This research was financially supported by the Netherlands Organization for Scientific Research (NWO); Project # EPC 5745.

# **Mechanical Characterization of Glassy Polymers using Instrumented Indentation**

PROEFSCHRIFT

ter verkrijging van de graad van doctor aan de  
Technische Universiteit Eindhoven, op gezag van de  
Rector Magnificus, prof.dr.ir. C.J. van Duijn, voor een  
commissie aangewezen door het College voor  
Promoties in het openbaar te verdedigen  
op donderdag 17 januari 2008 om 16.00 uur

door

**Christophe Gilbert Noël Pelletier**

geboren te Saint-Rémy, Frankrijk

Dit proefschrift is goedgekeurd door de promotoren:

prof.dr.ir. J.M.J. den Toonder

en

prof.dr.ir. H.E.H. Meijer

Copromotor:

dr.ir. L.E. Govaert





# Contents

---

<b>Summary.....</b>	<b>XI</b>
<b>1. Introduction.....</b>	<b>1</b>
1.1. Indentation .....	2
1.1.1. Instrumented indentation .....	3
1.1.2. Indentation analysis .....	4
1.2. Deformation of glassy polymers.....	6
1.3. The scope of this thesis .....	8
1.3.1. Misalignment .....	8
1.3.2. Plasticity.....	9
1.3.3. Viscoelasticity.....	9
<b>2. The influence of indenter-surface misalignment on the results of instrumented indentation tests .....</b>	<b>15</b>
2.1. Introduction.....	16
2.2. Experimental .....	18
2.2.1. Materials and techniques.....	18
2.2.2. Misalignment correction: procedure .....	19
2.3. Results and discussion .....	21
2.3.1. Frame compliance correction.....	21
2.3.2. Misalignment study.....	22
2.3.3. Possibility for post-indentation correction.....	28
2.4. Conclusions.....	29
<b>3. Numerical simulation of flat-tip micro-indentation of glassy polymers: influence of loading speed and thermodynamic state .....</b>	<b>35</b>
3.1. Introduction.....	36
3.2. Finite strain deformation of glassy polymers.....	37
3.2.1. Phenomenology.....	37
3.2.2. Numerical model, the “Eindhoven” model.....	39



3.3. Experimental .....	45
3.3.1. Materials and sample preparation .....	45
3.3.2. Techniques .....	46
3.3.3. Numerical simulations .....	47
3.4. Results and discussion .....	48
3.4.1. Thermorheologically simple behavior: PC .....	48
3.4.2. Thermorheologically complex behavior: PMMA.....	55
3.5. Conclusions.....	58

**4. Quantitative assessment and prediction of the contact area development during spherical tip indentation of glassy polymers ..... 65**

4.1. Introduction.....	66
4.2. Mechanical properties of glassy polymers: phenomenology.....	68
4.3. Modeling.....	68
4.3.1. Constitutive modeling.....	68
4.3.2. Indentation modeling .....	72
4.4. Materials and experimental methods .....	74
4.4.1. Materials .....	74
4.4.2. Optical indentation microscope .....	74
4.5. Results and discussion .....	75
4.5.1. Experimental determination of the contact area .....	75
4.5.2. Numerical simulation vs. experiments.....	75
4.5.3. Large deformation investigation: pile-up.....	78
4.5.4. Relaxation .....	80
4.6. Conclusions.....	81

**5. Viscoelastic film properties determined using indentation and conventional testing: a comparison.....85**

5.1. Introduction.....	86
5.2. Theory .....	86
5.3. Materials and methods .....	89
5.4. Results and discussion. ....	90

5.4.1. Macroscopic viscoelastic characterization.....	90
5.4.2. Linear viscoelastic indentation .....	93
5.5. Conclusions.....	97
<b>6. Conclusions and recommendations.....</b>	<b>103</b>
6.1. Conclusions.....	104
6.2. Recommendations.....	105
<b>Samenvatting.....</b>	<b>107</b>
<b>Acknowledgement.....</b>	<b>109</b>
<b>Curriculum Vitae.....</b>	<b>111</b>
<b>List of publications.....</b>	<b>113</b>



## Summary

---

### **Mechanical characterization of glassy polymers using instrumented indentation**

Instrumented indentation is a versatile technique to probe local mechanical properties of films and/or bulk materials. In principle, a well-defined body is pressed into the surface of a material while measuring load and penetration depth. The data obtained are subsequently analyzed to obtain mechanical quantities such as Young's modulus or yield strength. Especially in the case of polymers, however, this analysis is hampered by the fact that the exact contact area and the displacement into the surface are unknown. In addition, appropriate quantitative analysis methods for polymer indentation are still lacking. This thesis describes the development of a numerical-experimental methodology that allows for quantitative interpretation of instrumented-indentation tests on polymer systems.

In the first part of the thesis, we focus on the characterization of the large-strain deformation behavior of glassy polymers, in particular polycarbonate (PC) and polymethylmethacrylate (PMMA). We employ flat-tip indentation experiments since they possess a well-defined elastic-to-plastic transition visible in the indentation load-displacement curves. The flat-tip indentation technique is experimentally refined by the development of a universal alignment stage that allows us to reach perfect tip-surface alignment and thus achieve a constant contact area during the entire indentation run. Moreover, the set-up makes it possible to quantitatively analyze the (tremendous) influence of tip-sample misalignments that usually occur in standard indentation tests.

In the plastic regime, glassy polymers possess a rather complex intrinsic behavior, with a pronounced pressure and rate-dependence of the yield stress as well as a post yield region displaying both strain softening and strain hardening. We employ a state-of-the-art constitutive model, previously developed in our group, that quantitatively captures this intrinsic behavior, to numerically predict the indentation response. In the model, a single parameter, the state parameter  $S_a$ , is used to uniquely determine the initial yield stress of the material, incorporating all variations in its thermal history. Flat-tip micro-indentation tests were performed on two materials, polycarbonate (PC) and poly(methyl methacrylate) (PMMA), at various loading speeds and thermal histories. For PC the yield stress increases proportionally with the logarithm of strain-rate, whereas for PMMA, a characteristic change in slope can be observed at higher strain rates. We demonstrate that, given the proper definition of the viscosity function, the flat-tip indentation response at

different indentation speeds can be described accurately for both materials. Moreover, it is shown that the parameter set obtained for each material is also representative for the mechanical response on a *macroscopic* scale. This implies that the thermodynamic state of PC and PMMA can now be determined by fitting a single parameter on a single indentation test.

Large-depth indentation of glassy polymers is also studied employing an optical-indentation microscope that allows measuring the evolution of the contact area in-situ during spherical-tip indentation. It is demonstrated that the numerical model is able to correctly predict the development of the indentation contact area in both the elastic as well as the plastic regime, including the influences of the thermal history of the sample and the indentation speed. Moreover, it is shown that pile-up around the indenter results from localization effects and is thus promoted by the strain softening properties of the material.

The last part of the thesis deals with the characterization of the linear viscoelastic properties using instrumented indentation. We perform dynamic load indentation with a Berkovich tip on two acrylate films with different glass transition temperatures. The dynamic quantities thus obtained prove to be in agreement with data obtained from macroscopic DMTA in uniaxial extension. By employing the linear viscoelastic correspondence principle, the relaxation time spectra obtained can be used to quantitatively predict the creep and stress relaxation response measured in spherical-tip indentation.

**Chapter 1**  
**Introduction**

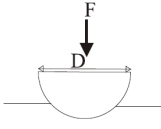
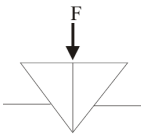
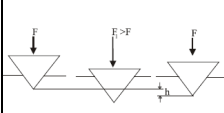
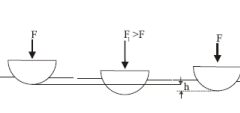
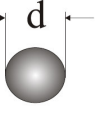
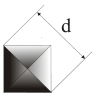
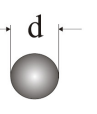
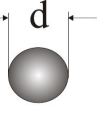
---

## 1.1. Indentation

An increased engineering requirement, at the beginning of the last century, led to a demand for a reproducible high quality steel. To satisfy this demand, the steel-producing industry needed initially a fast control quality test. This problem motivated Brinell to develop the first indentation test in 1900, which was the precursor of modern instrumented indentation. A spherical steel indenter was pressed onto the surface of a specimen. The aim of this test was to determine the hardness, defined as the material resistance to localized plastic deformation. Although the Brinell method was useful to probe the hardness of steel, this method also showed some serious limitations. Since the indenter was made of steel as well, only a narrow class of materials could be investigated, otherwise the deformation of the indenter itself induced a significant error in the measurement. In addition to this, due to the spherical shape of the tip, the Brinell test cannot be performed on thin material films and small samples.

The development of harder materials with a finer grain structure motivated Rockwell (1919) and Vickers (1925) to further develop the indentation-hardness test. Differences between the Brinell's, Rockwell's and Vickers method are summarized in Table 1.1.

**Table 1.1:** An overview of the different hardness measurement methods.

	Brinell	Vickers	Rockwell	
Indenter shape (side view)				
Indenter	Sphere of Steel	Diamond pyramid	Diamond cone	Sphere of Steel
Residual contact area (top view)				
Method description	Determination of the residual diameter (d)	Determination of the residual diagonal (d)	Determination of the difference in the permanent penetration (h)	
Hardness	$BNH = \frac{F}{\frac{\pi}{2} D (D - \sqrt{D^2 - d^2})}$	$VH = 1.854 \frac{F}{d}$	$R_{A \text{ or } C} = N - \frac{h}{S} \text{ with } N \text{ and } S \text{ constant}$	

Nowadays, indentation is widely used in quality control of steel. Its success results from the low cost of indentation devices, the simplicity of the test and the fact that no special sample preparation is needed. In addition to this, indentation has two other advantages: it is a nondestructive test, the specimen is neither fractured nor excessively deformed, and only a small amount of material is needed.

However, hardness is not an intrinsic material property since its value depends on the testing method. Therefore, many empirical or semi-empirical relationships between hardness and yield stress, which indeed is an intrinsic property, have been established for metals and ceramics. In the fully plastic regime, Tabor [1] experimentally found hardness to be proportional to yield stress by a constant factor, the so-called constraint factor, nearly equal to 3. Its precise value depends on the indenter shape and on the friction between indenter and sample [2]. Tabor's relation is valid for metals with high value of the ratio elastic modulus to yield stress. In case of elasto-plastic deformation, hardness can be related to the yield using the cavity expansion model developed by Johnson [2, 3]. The model supposes the existence of a spherical hydrostatic core under the tip, bounded by a concentric zone of plastic flow, beyond which the stress is purely elastic. It should be mentioned that these models described above are limited to materials which exhibit an elastic perfectly plastic deformation. They are thus not suitable when glassy polymers are indented since their intrinsic behavior is more complex.

### 1.1.1. Instrumented indentation

Instrumented indentation takes its origin in the indentation for hardness tests, and also here an indenter-tip of a known shape is pressed onto a material. Contrary to the hardness test, with instrumented indentation the load and the displacement are continuously recorded during the experiment, see Figure 1.1. The most commonly used tip shapes are: the Berkovich (tip-three side pyramid), the sphere, the cone and the flat-ended punch tip.

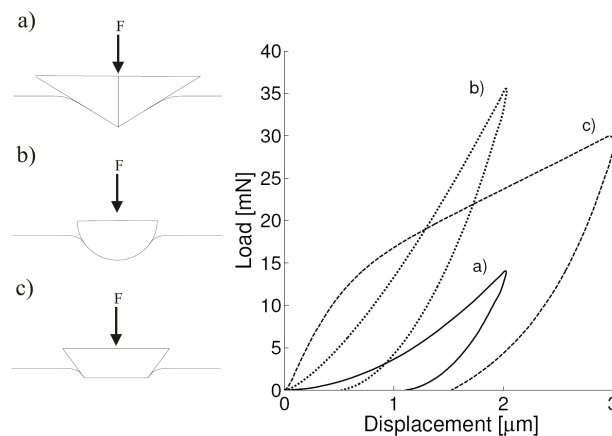


**Figure 1.1:** Typical load displacement curve for: a) a Berkovich tip (solid line); b) spherical tip (dotted line) and; c) flat punch (dashed line).



Although, the first instrumented indentation device was introduced as early as at the end of the 19<sup>th</sup> century by Martens [4], instrumented indentation was developed in the 70s [5, 6]. The main driving force is the constant reduction in size that has led to the increasing use of thin films or coatings in a range of industries. This reduction in film thickness leads sometimes to a change in the material's behavior from that of its bulk form. Since conventional macroscopic tests, like tensile or compression tests, are not feasible on thin films, instrumented indentation was then developed to enable quantitative mechanical testing of thin films. With this technique it is possible to determine elastic moduli [7-9], time dependence of polymers [10-12] and soft metals [13-15], fracture behavior [16-20] and plasticity of polymers [21-25] and metals [26-28]. However, it should be mentioned that the models used to determine the mechanical properties from instrumented indentation tests are not always widely accepted. The complexity of the stress field developed under the tip renders the data interpretation considerably difficult.

### 1.1.2. Indentation analysis

#### *Elasticity*

The nature and the distribution of stress in the linear elastic regime was first studied by Hertz in 1881 [29] and Boussinesq in 1885 [30] for a spherical indenter. The analytical solutions are restricted to a frictionless, continuous contact and limited to a small ratio contact radius to tip radius. Moreover, Hertz derived a load-displacement relationship from analytical solutions for stress and strain. Experimentally, this gives the possibility to determine the elastic modulus from the experimental data. Later, Sneddon [31] generalized load-displacement relationships for any axisymmetric punch.

In some cases, when sharp tips are used, plasticity occurs at the early stage of deformation and the linear elastic regime, thus, cannot be measured during loading. In that case the unloading curve can be used to determine the elastic modulus. The most widely used method is the one developed by Oliver and Pharr [7] for a Berkovich tip. The method is based on the following assumptions [32]:

- a dominant elastic deformation occurs upon unloading during which neither time dependence nor plasticity plays a role in the recovering work.
- the surface profile at the vicinity of the tip is assumed to always sink-in (see Figure 1.2) and the method thus cannot be applied to materials which exhibit pile-up, caused by plastic deformation. In general, the degree of pile-up is determined by the ratio of elastic modulus to yield stress, as well as strain hardening [33-35]. When the Oliver and Pharr method is applied to materials which exhibit pile-up, the contact area is underestimated and the elastic modulus is overestimated [33, 36].

For glassy polymers, these two assumptions render the determination of the elastic modulus by Oliver and Pharr method questionable [37-40].

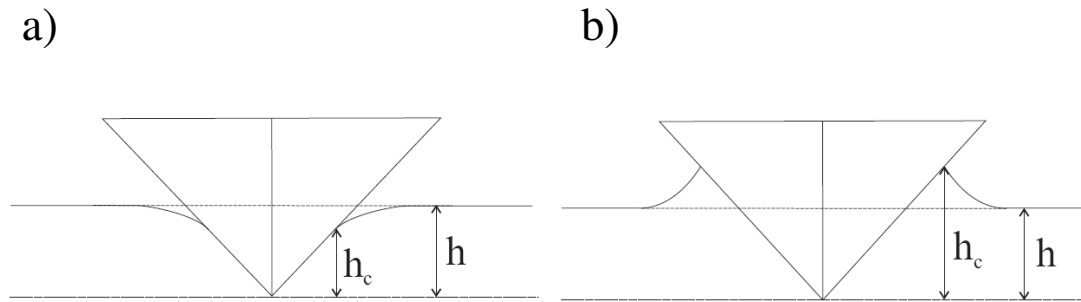


**Figure 1.2:** Surface profile at the vicinity of the tip: a) when the material sink-in the contact depth,  $h_c$ , is smaller than the measurement tip displacement,  $h$ ; b) when the material pile-up  $h_c$  is greater than  $h$ .

### *Viscoelasticity*

Since polymers exhibit an intermediate range of behavior between elastic solids and viscous liquids they display a strong time dependence, depending on the temperature and the experimental time-scale. This dependence can be expressed both in the time and the frequency domain. Linear viscoelastic indentation models were developed for quasi static loading [10, 41-44] and dynamic loading [12, 45-47]. Although most of the publications are focused on developing new models, only few studies [48, 49] are dedicated to the validation of existing models, achieved by comparing linear viscoelastic properties obtained by conventional mechanical tests with those obtained by instrumented indentation.

For quasi-static loading, the first linear viscoelastic indentation model was developed by Lee and Radok [41]. In their approach, the material constants in the elastic solutions of contact problems are replaced by the corresponding differential operators in the viscoelastic constitutive equation. The model was restricted to a monotonically increasing contact area, and later Ting [42, 43] and Graham [50, 51] proposed a more general solution.

In the frequency domain, the indenter-sample interaction is modeled by an arrangement of springs and dashpots [45]. Using this model, the contact stiffness and damping coefficient can be calculated from the experimental amplitude and phase difference between the load and displacement signals. The storage and loss modulus are then obtained from the contact stiffness and damping coefficient, respectively, using equations [45] based on the elastic solution developed by Oliver and Pharr [7].

### *Plasticity*

The determination of material properties in the elastoplastic or plastic regime presents a challenge, since no analytical models are available to determine either the contact area or the stress field developed under the indenter. Therefore, to obtain large strain mechanical properties of glassy polymers, numerical models are combined with experimental

instrumented indentation [21, 22]. This method requires a proper constitutive model which captures the complex intrinsic behavior of glassy polymers, and an effective inverse analysis method, which would make it possible to obtain the parameters in the constitutive model by fitting the load-displacement curve. In most cases, the number of parameters in the model, used to correctly capture the complex intrinsic behavior, makes the reverse analysis quite difficult. Zhang *et. al* [22] succeed to extract the parameters used in their model by fitting the indentation load displacement curve. Their model takes into account visco –elastoplastic deformation, the rate and pressure dependence of the yield stress, strain hardening deformation but does not incorporate strain softening. However, to reduce complexity in the inverse analysis, they further simplify their model by neglecting strain hardening and strain rate effects when they fit the indentation curves. In a similar approach, Anand *et al.* [25] combined the finite element analysis with instrumented indentation and they model the indentation response with the parameters determined from macroscopic compression tests. The load and displacement curves were not directly used to determine the mechanical properties of the glassy polymers.

## 1.2. Deformation of glassy polymers

Contrary to metals, glassy polymers exhibit a rather complex intrinsic behavior, defined as the true strain-stress response during homogenous deformation (see Figure 1.3). At small deformations, linear viscoelastic deformation is found and when also the time dependence is weak, the linear viscoelastic regime can be approximated by a linear elastic regime where the stress - strain relation is described by Hooke's law.

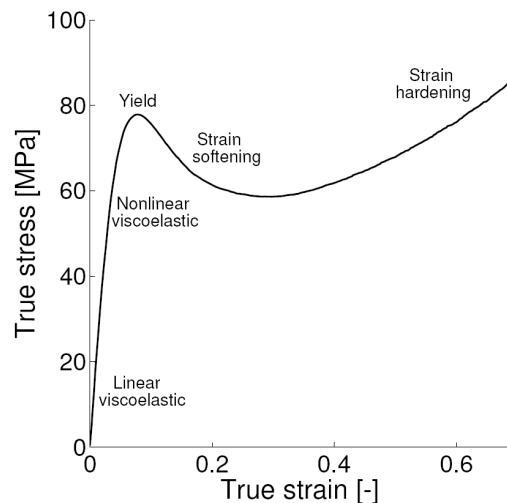


**Figure 1.3:** Typical true stress-strain curve obtained under compression test.

In the linear viscoelastic range, the stress and strain expression is formulated in terms of a Boltzmann single integral operator associated with a hereditary function. The relaxation times are then given by continuous relaxation spectra. Alternatively, the relaxation times can be given by discrete relaxation spectrum. In that case the stress and strain expression is formulated in terms of differential operators representing a combination of springs and dashpots.

In the non-linear viscoelastic range, the response of the material is dependent on the stress level. Most of the constitutive equations used here are generalizations of the linear Boltzmann integral [52]. Finally, in the linear and non-linear viscoelastic regime, the deformation is reversible, since no permanent deformation is observed after the load is released.

When the stress reaches a critical value, the yield stress, plastic deformation sets in and deformation is no longer reversible within the time scale of the experiments, see Figure 1.3. The yield stress exhibits a strain-rate and a pressure dependence. An increase of the strain rate leads to an increase in yield stress and the same behavior is observed when the hydrostatic pressure increases. Regarding the strain rate and temperature dependence of the yield stress two classes of materials can be distinguished:

- Thermo-rheologically simple materials for which the deformation kinetics are dominated by a single molecular process, i.e. the primary glass transition ( $\alpha$ -process). Here, the yield stress as a function of the logarithm of the strain rate shows a linear dependence.
- Thermo-rheologically complex materials for which the deformation kinetics are governed by multiple molecular processes ( $\alpha$ + $\beta$ -process where  $\beta$  refers to a secondary transition). In that case, the curves exhibit a change in the slope over a broad spectrum of strain rates.

Passing the yield stress, the material's resistance to plastic flow decreases due to structural changes: strain softening (Figure 1.3). The macroscopic response and the amount of softening of glassy polymers is dependent on the thermal-history. By annealing, yield stress, and thus strain softening, are increasing. On the contrary, by quenching, strain softening and yield stress decrease. The effect of the thermal-history can be completely erased by a mechanical pre-treatment: the effect is called mechanical rejuvenation and softening is completely removed. Finally with increasing strength during plastic deformation, molecules become oriented which gives rise to a subsequent increase of the stress at large deformation: strain hardening.

In the past few decades considerable attention has been dedicated to the development of constitutive relations for the large strain deformation of solid polymeric materials [53-61]. Common factors in these models are the application of rubber elasticity to model strain hardening and a stress dependent viscosity to capture the deformation kinetics. In a recent study, Klompen [61] developed a constitutive model which can perfectly describe the yield and post yield behavior of glassy polymers, see Figure 1.4. The model captures the rate dependence, as well as the thermal history dependence of the intrinsic behavior.

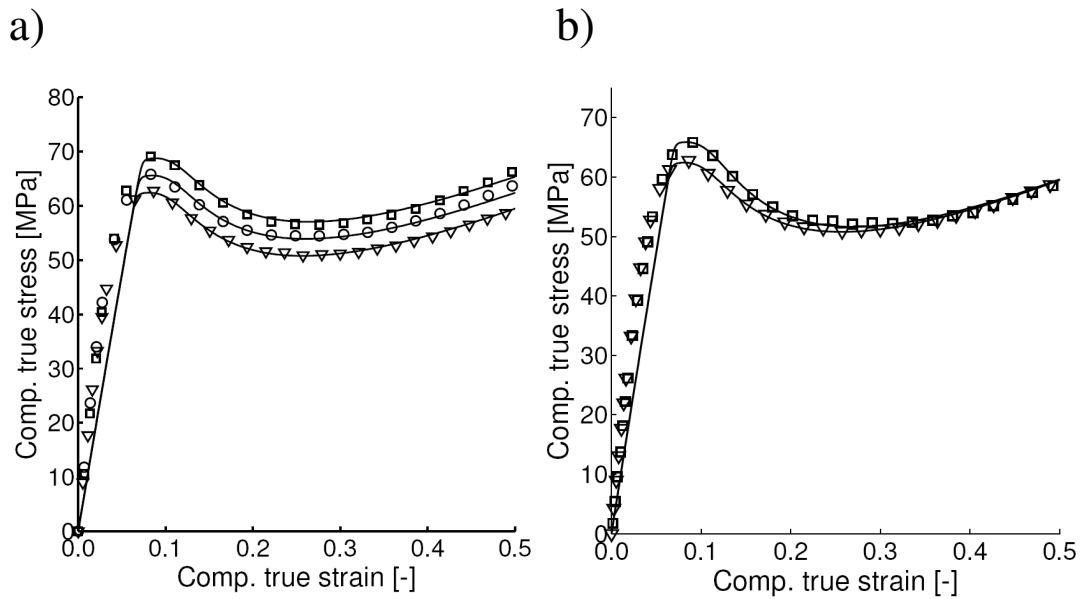


**Figure 1.4:** Experimental compression tests (open symbols) for PC compared with the numerical simulation (solid lines): a) for three different true strain rates:  $10^{-2} \text{ s}^{-1}$  ( $\square$ ),  $10^{-3} \text{ s}^{-1}$  ( $\circ$ ),  $10^{-4} \text{ s}^{-1}$  ( $\nabla$ ); b) for two different thermal histories: annealed ( $\square$ ) and as received ( $\nabla$ ). Data from Klompen [61].

### 1.3. The scope of this thesis

The goal of this thesis is to provide a method which enables determination of the material properties from instrumented indentation tests on glassy polymers. In particular, three main issues are addressed.

#### 1.3.1. Misalignment

All models used in instrumented indentation data analysis so far, assume that the sample is perfectly aligned with the tip, i.e. the normal to the sample surface is parallel to the axis of symmetry. In reality a perfect tip-sample alignment is rather difficult to achieve and this is especially true when the measurements are scaled down. Surprisingly no complete studies dedicated to the misalignment were produced up to now. Therefore, Chapter 2 presents a quantitative study of the influence of misalignment on the experimental load-displacement curve. Three different tip geometries are used: the Berkovich tip, the spherical tip and the flat punch. In addition we also present methods to correct for effects of misalignment.

### 1.3.2. Plasticity

To characterize mechanical properties of glassy polymers, we combine a finite element method with instrumented indentation analysis. Here, indentation tests and macroscopic tests are simulated with a consistent set of parameters and compared with the experiments. Chapter 3 presents the results for a thermorheologically simple and complex materials and for two different thermal histories for each class of materials.

Since the development of the contact area during indentation is unknown for a general elastoplastic deformation, this problem is separately studied in Chapter 4. First, the contact area is simulated and compared with experimental contact areas, measured *in situ* using an optical-indentation microscope. The parameters in the constitutive model are determined from macroscopic tensile tests. The results presented in Chapter 4, are obtained for different indentation speeds and thermal histories. Moreover, the development of the contact area is studied at large deformations by using the finite element analysis only. Pile-up is expected at such deformation and the fundamental parameters that control pile-up for glassy polymers are identified. Previous studies of pile-up [33, 35] were performed using constitutive models developed for metals and did not incorporate the rate dependence of the yield stress and the strain softening.

### 1.3.3. Viscoelasticity

Chapter 5 is focused on the validation of the existing linear viscoelastic indentation model in the time [10, 41-44] and frequency domain [12, 45-47]. This subject was, so far, not widely studied and only a few publications are found [48, 49]. We investigate two acrylate films with different glass transition temperatures.

In the frequency domain, the results obtained from the instrumented indentation are directly compared to those obtained with a classical rheological method, DMTA. The mechanical properties in the time domain are predicted from the DMTA by using linear viscoelastic theory and then compared with those obtained from the instrumented indentation.

## References

- [1] D. Tabor, *Hardness of metals*. 1951, Oxford: Clarendon press.
- [2] K.L. Johnson, *Contact mechanics*, Cambridge University Press. 1985, Cambridge.
- [3] K.L. Johnson, *The correlation of indentation experiments*. J.Mech. and Phys. Solid, 1970. **18**: p. 115-128.
- [4] A. Martens, *Handbuch der Materialienkunde für den Maschinenbau*. 1898, Berlin: Springer.

- 
- [5] V.P. Alechin and G.S. Berlin, *On the method for the micro mechanical test of materials using micro indentation (in Russian)*. Zavodskaja Laboratorija, 1972. **4**: p. 488.
- [6] F. Frohlich, P. Grau, and W. Grellmann, *Performance and analysis of recording microhardness*. Phys. Status Solidi (a), 1977. **42**: p. 79-89.
- [7] W.C. Oliver and G.M. Pharr, *An improved technique for determining hardness and elastic-modulus using load and displacement sensing indentation experiments*. J Mater. Res., 1992. **7**(6): p. 1564 - 1583.
- [8] M.F. Doerner and W.D. Nix, *A method for interpreting the data from Depth-Sensing Indentation Instruments*. J. Mat. Res., 1986. **1**: p. 601-609.
- [9] W.D. Nix, *Mechanical properties of thin films*. Metall. Trans. A., 1989. **20**: p. 2217-2245.
- [10] L. Cheng, X. Xia, W. Yu, L.E. Scriven, and W.W. Gerberich, *Flat punch indentation of viscoelastic material*. Journal of Polymer Science B: polymer physics, 2000. **38**(1): p. 10-22.
- [11] P.L. Larsson and S. Carlsson, *On microindentation of viscoelastic polymers*. Polymer Testing, 1998. **17**: p. 49-75.
- [12] J.L. Loubet, W.C. Oliver, and B.N. Lucas, *Measurement of the loss tangent of low-density polyethylene with nanoindentation technique*. J Mater. Res., 2000. **15**: p. 1195-1198.
- [13] S.A.S. Asif and J.B. Pethica, *Nanoindentation creep of a single-crystal tungsten and gallium arsenide*. Phil. Mag. A., 1997. **76**(6): p. 1105-1118.
- [14] S.A.S. Asif and J.B. Pethica, *Nano-scale indentation creep-testing at non-ambient temperature*. J. Adh., 1998. **67**(1-4): p. 153-165.
- [15] B.N. Lucas and O. W.C., *Indentation power-law creep of high purity indium*. Metall. Trans. A., 1999. **30**(3): p. 601-610.
- [16] B.R. Lawn, A.G. Evans, and D.B. Marshall, *Elastic/plastic indentation damage in ceramics: the median/radial crack system*. J. Am. Ceram. Soc., 1980. **63**: p. 574-581.
- [17] G.R. Anstis, P. Chantikul, B.R. Lawn, and D.B. Marshall, *A critical evaluation of indentation techniques for measuring fracture toughness: I Direct crack measurements*. J. Am. Ceram. Soc., 1981. **64**: p. 533-538.
- [18] M.T. Laugier, *Palmqvist indentation toughness in WC-CO composites*. J Mater. Sci. Lett., 1987. **6**: p. 897-900.
- [19] R. Dukino and M.V. Swain, *Comparative measurement of indentation fracture toughness with Berkovich and Vickers indenters*. J. Am. Ceram. Soc., 1992. **75**: p. 3299-3304.

- 
- [20] J.S. Field, M.V. Swain, and J.D. Dukino, *Determination of fracture toughness from the extra penetration produced by indentation pop-in*. J. Mater. Res., 2003. **18**: p. 1412-1416.
- [21] M.L. Oyen and R.F. Cook, *Load–displacement behavior during sharp indentation of viscous–elastic–plastic materials*. J. Mater. Res., 2003. **18**(1): p. 139-150.
- [22] C.Y. Zhang, Y.W. Zhang, K.Y. Zeng, and L. Sheng, *Characterization of mechanical properties of polymers by nanoindentation tests*. Phil. Mag., 2006. **86**(28): p. 4487-4506.
- [23] R. Rikards, A. Flores, F. Ania, V. Kushnevski, and F.J. Baltá Calleja, *Numerical-experimental method for the identification of plastic properties of polymers from microhardness tests*. Comput. Mater. Sci., 1998. **11**: p. 233-244.
- [24] J.L. Bucaille, E. Felder, and G. Hochstetter, *Identification of the viscoplastic behavior of a polycarbonate based on experiments and numerical modeling of the nano-indentation test*. J. Mater. Sci., 2002. **37**(18): p. 3999-4011.
- [25] L. Anand and N.M. Ames, *On modeling the micro-indentation response of an amorphous polymer*. Int. J. of Plasticity, 2006. **22**: p. 1123-1170.
- [26] J.S. Field and M.V. Swain, *A simple prediction model for spherical indentation*. J. Mater. Res., 1993. **8**(2): p. 297-306.
- [27] J.S. Field and M.V. Swain, *Determining the mechanical properties of small volumes of material from submicron spherical indenters*. J. Mat. Res., 1995. **10**(1): p. 101-112.
- [28] M.V. Swain, *Mechanical properties of small volumes of brittle materials with spherical tipped indenters*. Mat. Sci. and Eng. A, 1998. **253**: p. 160-166.
- [29] H. Hertz, *Über die Berührung Fester Elastischer Körper (On the contact of elastic solids)*. J. Reine Angew. Math., 1881. **92**: p. 156-171.
- [30] J. Boussinesq, *Application des potentiels à l'étude de l'équilibre et du mouvement des solides élastiques*. 1885, Paris: Gauthier-Villars.
- [31] I.N. Sneddon, *The relation between load and penetration in the axisymmetric Boussinesq problem for a punch of arbitrary profile*. Int. J. of Eng. Sci., 1965. **3**: p. 47-57.
- [32] W.C. Oliver and G.M. Pharr, *Measurement of hardness and elastic modulus by instrumented indentation: Advances in understanding and refinements to methodology*. J. Mat. Res., 2004. **19**(1): p. 3-20.
- [33] A. Bolshakov and G.M. Pharr, *Influence of pileup on the measurement of mechanical properties by load and depth sensing indentation techniques*. J. Mat. Res., 1998. **13**(4): p. 1049-1058.



- 
- [34] M. Mata, M. Anglada, and J. Alcalá, *Contact deformation regimes around sharp indentations and the concept of the characteristic strain*. J. Mat. Res., 2002. **17**: p. 964-976.
- [35] B. Taljat and G.M. Pharr, *Development of the pile-up during spherical indentation of elastic-plastic solids*. Int. J. of Solid and Structures, 2004. **41**: p. 3891-3904.
- [36] A.E. Giannakopoulos and S. Suresh, *Determination of elastoplastic properties by instrumented sharp indentation*. Scripta Mater., 1999. **40**(10): p. 1191-1198.
- [37] B.J. Briscoe and K.S. Sebastian, *The elastoplastic response of poly(methylmethacrylate) to indentation*. Proc. Royal Soc. London A., 1996. **452**: p. 439-457.
- [38] B.J. Briscoe, L. Fiori, and E. Pelillo, *Nano-indentation of polymeric surfaces*. J. Phys. D: Appl. Phys., 1998. **31**: p. 2395-2405.
- [39] M.R. VanLandingham, J.S. Villarrubia, W.F. Guthrie, and G.F. Meyers, *Nanoindentation of polymers: an overview*. Macromolecular Symposia, 2001. **167**: p. 15-44.
- [40] D. Tranchida, S. Piccarolo, J. Loos, and A. Alexeev, *Mechanical Characterization of Polymers on a Nanometer Scale through Nanoindentation. A Study on Pile-up and Viscoelasticity*. Macromol., 2007. **40**(4): p. 1259-1267.
- [41] E.H. Lee and J.R.M. Radok, *The contact problem for viscoelastic bodies*. Journal of Applied Mechanics, 1960. **30**: p. 438-444.
- [42] T.C.T. Ting, *The contact stresses between a rigid indenter and a viscoelastic half-space*. Journal of Applied Mechanics, 1966. **33**: p. 845-854.
- [43] T.C.T. Ting, *Contact problems in the linear theory of viscoelasticity*. Journal of Applied Mechanics, 1968. **35**: p. 248-254.
- [44] M.L. Oyen, *Analytical techniques for indentation of viscoelastic material*. Phil. Mag., 2006. **86**(33-35): p. 5625-5641.
- [45] S.A.S. Asif, K.J. Wahl, and R.J. Colton, *Nanoindentation and contact stiffness measurement using force modulation with a capacitive load-displacement transducer*. Rev. Sci. Instrum., 1999. **70**(5): p. 2408-2413.
- [46] J.L. Loubet, B.N. Lucas, and W.C. Oliver. *Conference proceedings: International workshop on instrumented indentation*. 1995. San Diego, NIST Spec. Publ. 896. p. 31-34.
- [47] B.N. Lucas, W.C. Oliver, and J.E. Swindeman. *The Dynamics of frequency specific depth-sensing indentation testing*. in *Spring MRS Meeting*. 1998. San Francisco, CA. **522**: p. 3-14.
- [48] M.R. Vanlandingham, N.-K. Chang, P.L. Drzal, C.C. White, and S.-H. Chang, *Viscoelastic characterization of polymers using instrumented indentation. I*.

- Quasi-static testing*. J. Polym. Sci.: Part B: Polym Physics, 2005. **43**: p. 1794-1811.
- [49] C.C. White, M.R. Vanlandingham, P.L. Drzal, N.-K. Chang, and S.-H. Chang, *Viscoelastic characterization of polymers using instrumented indentation. II. Dynamic testing*. J. Polym. Sci.: Part B: Polym Physics, 2005. **43**(1812-1824).
- [50] G.A.C. Graham, *The contact problem in the linear theory of viscoelasticity*. Int. J. of Eng. Sci., 1965. **3**: p. 27-46.
- [51] G.A.C. Graham, *The contact problem in the linear theory of viscoelasticity when the time dependent contact area has any number of maxima and minima*. Int. J. of Eng. Sci., 1967. **5**: p. 495-514.
- [52] I.M. Ward, *Mechanical properties of solid polymers*, John Wiley & Sons. 1983, Chichester.
- [53] M.C. Boyce, D.M. Parks, and A.S. Argon, *Large inelastic deformation of glassy polymers. Part 1: Rate dependent constitutive model*. Mech. of Mat., 1988. **7**: p. 15-33.
- [54] E.M. Arruda and M.C. Boyce, *Evolution of plastic anisotropy in amorphous polymers during finite straining*. Int. J. Plast., 1993. **9**: p. 697-720.
- [55] O.A. Hasan and M.C. Boyce, *A constitutive model for the nonlinear viscoelastic viscoplastic behaviour of glassy polymers*. Polym. Eng. Sci., 1995. **35**: p. 331-344.
- [56] C.P. Buckley and D.C. Jones, *Glass-rubber constitutive model for amorphous polymers near the glass transition*. Polymer, 1995. **36**: p. 3301-3312.
- [57] P.J. Dooling, C.P. Buckley, and S. Hinduja, *The onset of the nonlinear viscoelasticity in multiaxial creep of glassy polymers: a constitutive model and its application to PMMA*. Polym. Eng. Sci., 1998. **38**: p. 892-904.
- [58] C. Gerlach, C.P. Buckley, and D.P. Jones, *Development of an integrated approach to modelling of polymer film orientation processes*. Trans. Inst. Chem. Eng. Part A, 1998. **76**: p. 38-44.
- [59] T.A. Tervoort, E.T.J. Klompen, and L.E. Govaert, *A multi-mode approach to finite, three-dimensional, nonlinear viscoelastic behaviour of glassy polymer*. J. Rheol., 1996. **40**: p. 779-797.
- [60] L.E. Govaert, P.H.M. Timmermans, and W.A.M. Brekelmans, *The influence of intrinsic strain softening on strain localization in polycarbonate: modeling and experimental validation*. J. Eng. Mat. and Tech., 2000. **122**: p. 177-185.
- [61] E.T.J. Klompen, PhD thesis TU/e, *Mechanical properties of solid polymers*, 2005, [www.mate.tue.nl/mate/pdfs/4944.pdf](http://www.mate.tue.nl/mate/pdfs/4944.pdf)



## Chapter 2

# The influence of indenter-surface misalignment on the results of instrumented indentation tests\*

---

### Abstract

A quantitative study is presented on the influence of the sample misalignment on load-displacement curves measured in instrumented indentation. Three different tip geometries are considered: a Berkovich tip, a spherical tip and a flat-ended punch. A special alignment tool was developed, that allowed us to perfectly align the sample surface perpendicular to the loading-axis of the tip, regardless of the tip geometry and the origin of the misalignment. Moreover, this tool enabled us to systematically vary the angle of misalignment and study its effect on the indentation results.

It is shown that sample-misalignment angles smaller than  $1.2^\circ$  have no effect for the Berkovich and spherical tips, whereas flat-ended punch indentations are extremely sensitive to these small alignment errors. The strongest influence is observed in the linear elastic region, where the contact stiffness decreases markedly with increasing misalignment. In the plastic regime the sensitivity to misalignment disappears.

Finally we present a simple method to correct the influence of sample misalignment on the load-displacement curves obtained in flat-ended punch indentation.

\* This chapter is reproduced from: C.G.N. Pelletier, E.C.A. Dekkers, L.E. Govaert, J.M.J. den Toonder, H.E.H. Meijer, **The influence of indenter-surface misalignment on the results of instrumented indentation tests**, Polym. Test., **26**(7), 949-959, (2007)

## 2.1. Introduction

Instrumented indentation is now routinely employed to determine local mechanical properties of surfaces or thin films. Its main advantage is that it is not required to remove the film from its substrate, which provides the opportunity to probe the mechanical properties of thin layers of material in complex structures. The small amount of deformed volume allows assessment of the local mechanical properties and given the considerable improvement today in measuring and controlling loads and displacements at small scales, it is now possible to obtain mechanical properties at a sub-micron level.

During instrumented indentation tests, loads and displacements are constantly recorded. When the material response is linear elastic, analytical expressions can be derived for the relation between the indentation load and displacement. This subsequently enables the determination of the elastic modulus. These general expressions have the form [1-3]:

$$P = E_r M h^q \quad (2.1)$$

where  $P$  is the force applied,  $E_r$  the reduced modulus,  $h$  the indentation depth, and  $M$  and  $q$  are parameters determined by the tip geometry. For a spherical indenter with a radius  $R$ ,  $M = \frac{4}{3}\sqrt{R}$  and  $q=3/2$  [2]. For a flat punch indenter with a radius  $R$ ,  $M=2R$  and  $q=1$  [1].  $E_r$  is defined by:

$$\frac{1}{E_r} = \frac{1-\nu_s^2}{E_s} + \frac{1-\nu_i^2}{E_i} \quad (2.2)$$

where  $E_s$  and  $\nu_s$  are, respectively, the elastic modulus and the Poisson's ratio of the sample and  $E_i$  and  $\nu_i$  are those of the indenter. For polymer samples, the influence of the indenter can be neglected, since the diamond indenter is generally two orders of magnitude stiffer. In that case the reduced modulus reads:

$$E_r = \frac{E_s}{1-\nu_s^2} \quad (2.3)$$

In instrumented indentation usually three different tip geometries are employed: the Berkovich, spherical and flat-ended. Only in the case of the flat-ended punch the contact area between indenter and sample remains constant during the experiment. This

advantage has been fully employed to characterize linear viscoelastic properties under quasi-static [4] and dynamical excitation [5], plastic deformation [6, 7], and debonding [8]. However, despite its attractiveness, the flat punch geometry is not commonly used. The main reason for this is the difficulty to perfectly align the indenter with the sample, resulting in a non-constant contact area during indentation [9]. Moreover, in the case of small indenter sizes and/or small indentation depths, the misalignment can not be easily controlled and/or corrected.

In general, misalignment can be defined as a situation where the surface of the sample is not perpendicular to the symmetry axis of the tip. Based on this definition, we can distinguish two different types of misalignment, as depicted in Figure 2.1. The first case represents the sample misalignment (called misalignment type 1, Figure 2.1a). Here, the axis of symmetry of the tip is identical to the axis of force application, both not perpendicular to the sample surface. The second type of misalignment refers to an imperfect indenter/machine assembly (called misalignment type 2, Figure 2.1b). Here the axis of symmetry of the tip is not parallel to the load application axis whereas the latter is indeed perpendicular to the sample surface.

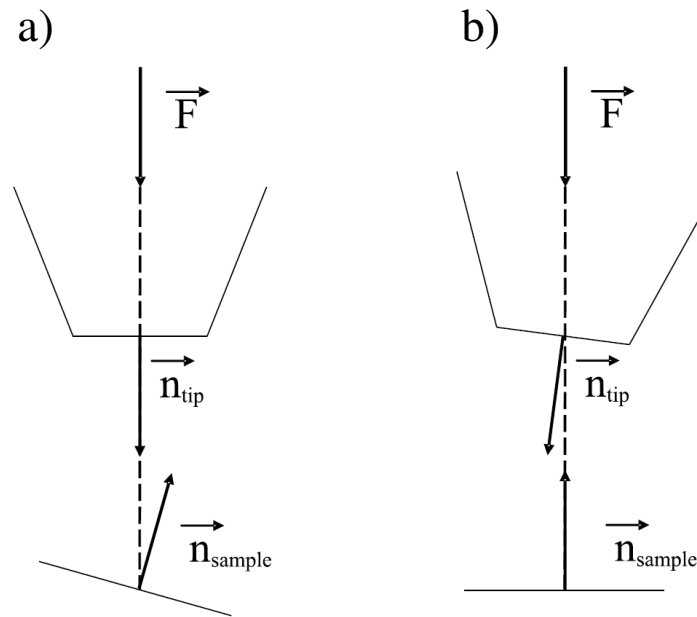


**Figure 2.1:** Representation of different types of misalignment: a) due to the sample and; b) due to the imperfect tip/machine assembly;  $\vec{F}$  represents the load application axis and  $\vec{n}$  the normal to the surface.

Misalignment, regardless of its origin, introduces an error in the force applied on the sample. Fortunately, this error is very small since it scales with the cosine of the misalignment angle (a misalignment angle of  $1^\circ$  introduces an error of 0.02% in the force applied on the sample). Therefore, this influence can be safely disregarded and

misalignment basically only induces changes in the development of the contact area during testing.

Here we present a study of the influence of misalignment on instrumented indentation using all three different tip geometries: Berkovich, spherical and flat-ended. For that we designed a special tool that not only allowed for perfect sample-tip alignment, but also provided the possibility to apply pre-defined misalignments. This allowed us to perform a systematic study on the effect of misalignment on the indentation load-displacement curves for the three tip geometries. The surface of the sample was first carefully aligned and then systematically tilted from that position. Finally, a “post-processing” method is presented that corrects for the influence of misalignment by directly modifying the load-displacement curves measured.

## 2.2. Experimental

### 2.2.1. Materials and techniques

The material used was polycarbonate (Makrolon, Bayer), obtained in the form of extruded sheet of 3 mm thickness. No further thermal treatment was applied to the samples. Prior to the indentation tests, the sheet roughness was determined by direct imaging using a commercial Atomic Force Microscope (Nanoscope IIIa, Digital Instruments, Santa Barbara, California) in tapping mode. A mean roughness,  $R_a$ , of about 5 nm was measured.

Indentation experiments were carried out using a nano-indenter XP (MTS Nano-Instruments, Oak Ridge, Tennessee). Three different tip geometries were used: a Berkovich tip, a spherical tip (radius,  $R = 25 \mu\text{m}$ ), and a flat-ended cone ( $R_{\text{flat}} = 5 \mu\text{m}$ ; cone angle,  $\varphi = 72^\circ$ ). All experiments were performed under displacement control with a speed of  $50 \text{ nm}\cdot\text{s}^{-1}$ . All tests were performed four times to check reproducibility.

Samples are considered well aligned when their surface is perpendicular to the axis of symmetry of the tip. To achieve this, a special alignment tool was designed, based on the construction mechanism of the elastic hinges (see Figure 2.2) and fabricated using electro-discharge wire cutting.

The alignment tool allows the rotation of the sample along two perpendicular axes. For each rotation axis, the mechanism used is the same and the rotation is realized by using elastic hinges with cylindrical cross sections [10-12]. Elastic hinges have the following advantages: they exhibit no hysteresis and no friction during bending, and they possess a high stiffness in the indentation loading direction and low stiffness perpendicular to that direction. The thickness of the elastic hinges was calculated to prevent plastic deformation up to a maximum rotation angle of  $\pm 0.7^\circ$  from the horizontal position (corresponding to a total angle of  $1.4^\circ$  in each direction). The rotation is activated by a micro spindle for each rotation axis. A displacement of  $10 \mu\text{m}$  of the spindle rotates the stage by  $0.1^\circ$ .

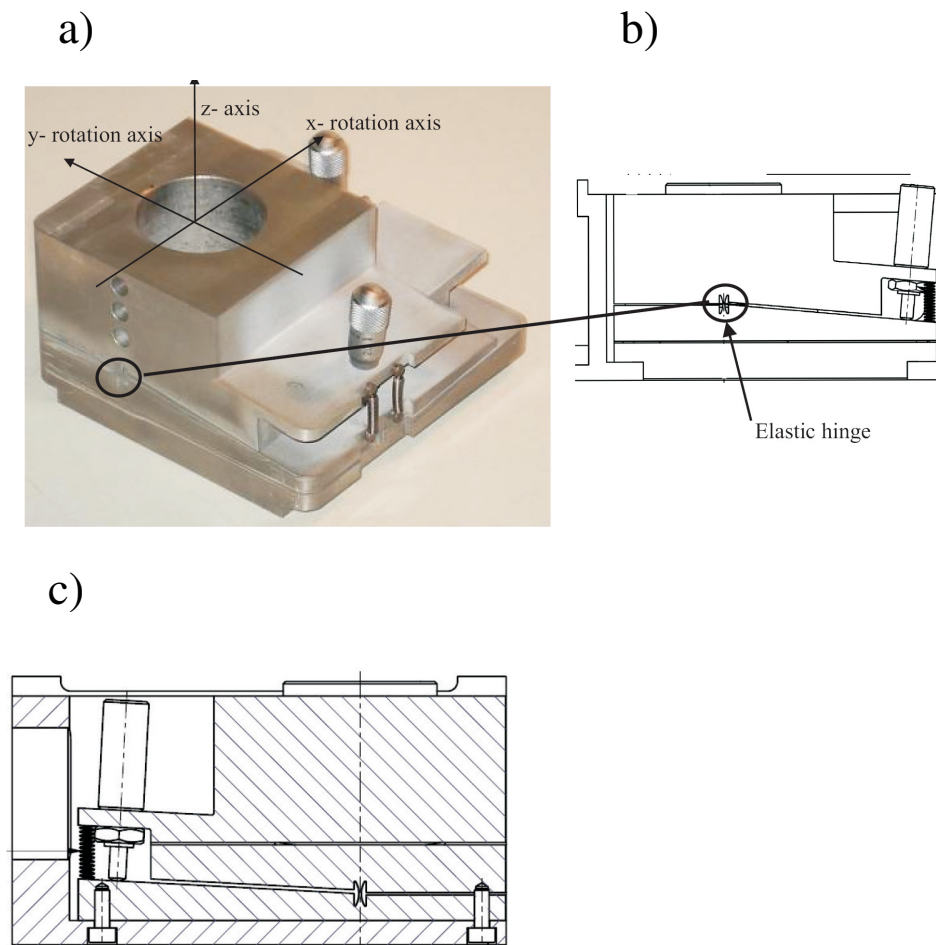


**Figure 2.2:** a) alignment tool designed to rotate the sample along two perpendicular axes using elastic hinges; b) cross section in the y-z plane showing the principle of one of the precise rotation mechanisms allowed by the elastic hinge; c) cross section in the x-z plane

### 2.2.2. Misalignment correction: procedure

First we deal with how to quantify and correct the misalignment that originates only from the sample (misalignment type 1). Please note, here we assume (for the moment) that the symmetry axis of the tip coincides with the loading axis. For all three tip geometries the same procedure is used. In the first set of tests, the samples are mounted on the alignment tool that is set in its neutral position. Subsequently four indentations are performed positioned on the four different corners of a square whose sides are parallel to both rotation axes (see Figure 2.3). The difference of the displacement at which the tip



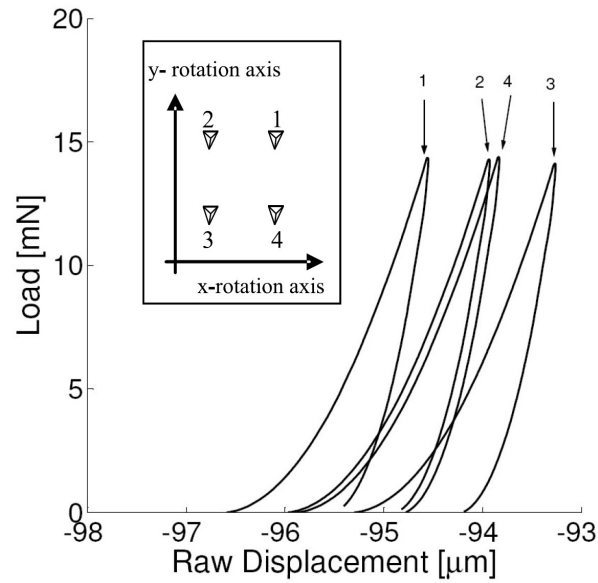


**Figure 2.3:** Four load-displacement curves obtained under sample misalignment conditions. The raw displacement values at which the tip touches the surface are used to quantify the angle between the surfaces of the tip and the sample.

contacts the surface of the sample gives the value  $h_{i-j}$ , which is the difference in the height between two indentation locations  $i$  and  $j$  along one rotation axis. With the distance ( $d$ ) between the two indentation points, the misalignment angle ( $\varphi$ ) equals:

$$\varphi = \arctg(h_{i-j} / d) \quad (2.4)$$

The differences  $h_{1-2}$  and  $h_{3-4}$  (compare Figure 2.3) determine the correction angle  $\varphi_y$  with respect to the  $y$ -axis, while  $h_{1-4}$  and  $h_{2-3}$  determine  $\varphi_x$ .

If the surface of the sample is sufficiently flat (which is easily verified), the height differences  $h_{1-2}$  and  $h_{3-4}$  will be equal, as will be the case for the height differences in along the other rotation axis ( $h_{1-4}$  and  $h_{2-3}$ ). Deviations will be indicative for a rough or wavy surface. From the values of the required correction angles  $\varphi_x$  and  $\varphi_y$ , the total misalignment angle,  $\varphi$ , between the normal to the surface and the loading axis can be deduced (derivation, see the Appendix):

$$\varphi = \arccos \left[ \frac{\cos(\varphi_x) \sin^2(\varphi_y)}{\cos(\varphi_y)} + \frac{\sin^2(\varphi_y) \sin^2(\varphi_x)}{\cos(\varphi_y) \cos(\varphi_x)} + \frac{\sin^2(\varphi_x) \cos(\varphi_y)}{\cos(\varphi_x)} + \cos(\varphi_y) \cos(\varphi_x) \right]^{-1} \quad (2.5)$$

It is mentioned here that the procedure described in first instance only holds for misalignment which originates from the sample. If additional misalignments are present during indentation, like misalignment of the tip relative to the direction of force measurement, the procedure is not valid anymore. For that, a different solution is proposed, see below.

## 2.3. Results and discussion

### 2.3.1. Frame compliance correction

Using the alignment tool during the indentation tests leads to a change of the original frame compliance. Therefore the new frame compliance was determined by indenting fused silica.

For the Berkovich tip, the frame compliance  $C_f$  was calculated using the Oliver and Pahr method [13] with the following relation:

$$C_f = C - \frac{\sqrt{\pi}}{2E_r} \frac{1}{\sqrt{A}} \quad (2.6)$$

where  $C$  is the total compliance (determined from the experimental load-displacement curve),  $A$  is the contact area and  $E_r$  is the reduced modulus defined by Equation 2.3. In that case the frame compliance was determined to be  $430 \text{ nm}\cdot\text{N}^{-1}$  for the alignment tool (instead of  $153 \text{ nm}\cdot\text{N}^{-1}$  obtained with the conventional sample holder).

For the spherical tip, the frame compliance  $C_f$  was calculated using two indentation points on the load –displacement curve in the elastic regime [14] :

$$C_f = \frac{\begin{bmatrix} h_1 - \left(\frac{P_1}{P_2}\right)^{2/3} & h_2 \end{bmatrix}}{\begin{bmatrix} P_1 - \left(\frac{P_1}{P_2}\right)^{2/3} & P_2 \end{bmatrix}} \quad (2.7)$$

where  $h$  is the indenter displacement into the surface,  $P$  is the load, and the indices 1 and 2 indicate two points on the curve. This procedure does not require knowledge of the reduced modulus and the tip radius. Using this indenter and this method, the same frame compliance was found as for the Berkovich tip:  $430 \text{ nm}\cdot\text{N}^{-1}$ .

For the flat-punch indentation, the frame compliance  $C_f$  was calculated in the elastic regime by using:

$$C_f = \frac{h}{P} - \frac{1}{2RE_r} \quad (2.8)$$

where  $h$  is the tip displacement into the surface,  $P$  is the load,  $R$  is the tip radius and  $E_r$  is the reduced modulus of the fused silica defined by Equation 2.3. A frame compliance of  $546 \text{ nm}\cdot\text{N}^{-1}$  was found for flat punch indentation with the alignment tool. The difference in the frame compliance found for Berkovich and spherical tip on the one hand ( $430 \text{ nm}\cdot\text{N}^{-1}$ ) and the flat punch on the other, originates from the difference in tip holder construction. For the typical indentation loads and depths used in the present study, the frame compliance differences will lead only to minor correction effects of the results.

### 2.3.2. Misalignment study

#### *Berkovich tip*

To measure and correct the sample misalignment, the procedure described in the Section (2.2) is applied. Figures 2.4a and 2.4b give the load-raw displacement curves of each test. Figure 2.4a shows results without correction of the sample misalignment and the data are used to probe the misalignment. As can be seen in Figure 2.4a, the tip touches the surface at different height positions since they are shifted.

Figure 2.4b shows results where correction was applied by rotating the sample after determining the misalignment angles,  $\varphi_x$  and  $\varphi_y$ , from Figure 2.4a. The load-displacement curves overlap, indicating that the sample surface is indeed horizontal now.

To investigate the influence of misalignment on load-displacement curves, the corrected sample is now deliberately tilted over an angle of  $0.4^\circ$ ,  $0.8^\circ$  (solely along the x-axis) and  $1.2^\circ$  ( $0.9^\circ$  along the x-axis and  $0.8^\circ$  along the y-axis) with respect to its perfectly aligned position. Figure 2.4c shows the load-displacement curves under each misalignment angle, averaged over four independent tests. The results show perfect overlapping of the curves obtained under different angles, illustrating that for the Berkovich tip misalignment has no effect on indentation, at least in this range of angles investigated. As a consequence, the contact stiffness (defined as  $S = dP / dh$ ) is also independent from misalignment, see Figure 2.4d.

Elastic modulus and hardness are calculated from the load-displacement curves, by the method proposed by Oliver and Pharr [15] and the hardness determined from the unloading curve shows a constant value of 0.2 GPa. For the elastic modulus, two variants of basically the same method were used: (i) the continuous stiffness measurement (CSM) technique [13] and (ii) calculation of the elastic modulus and hardness from the results at

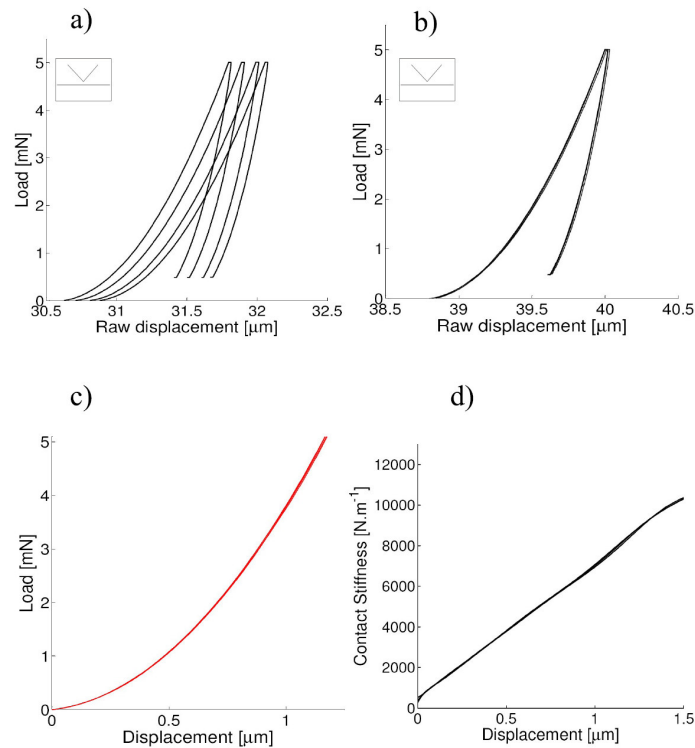


**Figure 2.4:** For Berkovich tip: a) load raw displacement curve when no sample misalignment correction was applied; b) after correction of the sample misalignment using the alignment tool; c) effect of the sample misalignment on the load displacement curves for an angle of  $0^\circ$ ,  $0.4^\circ$ ,  $0.8^\circ$ ,  $1.2^\circ$ ; d) contact stiffness for an angle of  $0^\circ$ ,  $0.4^\circ$ ,  $0.8^\circ$ ,  $1.2^\circ$ .

the beginning of unloading [13]. Both methods lead to the same value of the elastic modulus of 2.8 GPa regardless of the misalignment angle. Thus, it can be concluded that, using the Berkovich tip, misalignment has no influence on the hardness and elastic modulus determined.

Please note that the value of the elastic modulus of polycarbonate found by indentation is higher than the value commonly measured in tensile tests (which equals 2.2- 2.4 GPa). As just proven, this difference can not be assigned to misalignment of the sample but is due to the occurrence of pile-up, which is not considered in the Oliver and Pharr method [16] (developed using the experimental data measured on fused silica, where no pile up occurs). Consequently, when pile-up occurs the contact area is underestimated, leading to the observed overestimation in elastic modulus.

A change in the residual contact area profile with misalignment angle was also observed by Oliver and Pharr [13], but the conclusion here, that this does not influence modulus determination is in agreement with results obtained by Shafirstein *et al.* [17]. In their work, misalignment was achieved by indenting a 10 mm diameter single crystal alumina ball using a Berkovich tip. Later, the indentations were examined by SEM and

the angle between the surface of the sample and the indenter normal was calculated by the geometry of the indentations. The authors could determine that the surface misalignment has no effect on the hardness and elastic modulus for surface angles lower than  $8^\circ$ . They also observed that, by an increasing angle, the residual contact area became increasingly elongated.

### *Spherical tip*

Next we investigate the influence of misalignment on the load-displacement curves using a spherical tip. Figure 2.5a shows the results used to probe misalignment, again demonstrating that curves are shifted. After quantifying and correcting the sample position for misalignment, the load displacement curves plotted for each test indeed overlap, see Figure 2.5b.

Figures 2.5c and 2.5d present the results of tests where the sample was systematically tilted to a misalignment angle up to  $1.2^\circ$ . Both the load-displacement as well as the contact stiffness displacement curves are completely identical for all tests, indicating that misalignment has also no influence for this tip geometry at least in the range of  $\phi$ 's experimentally investigated.

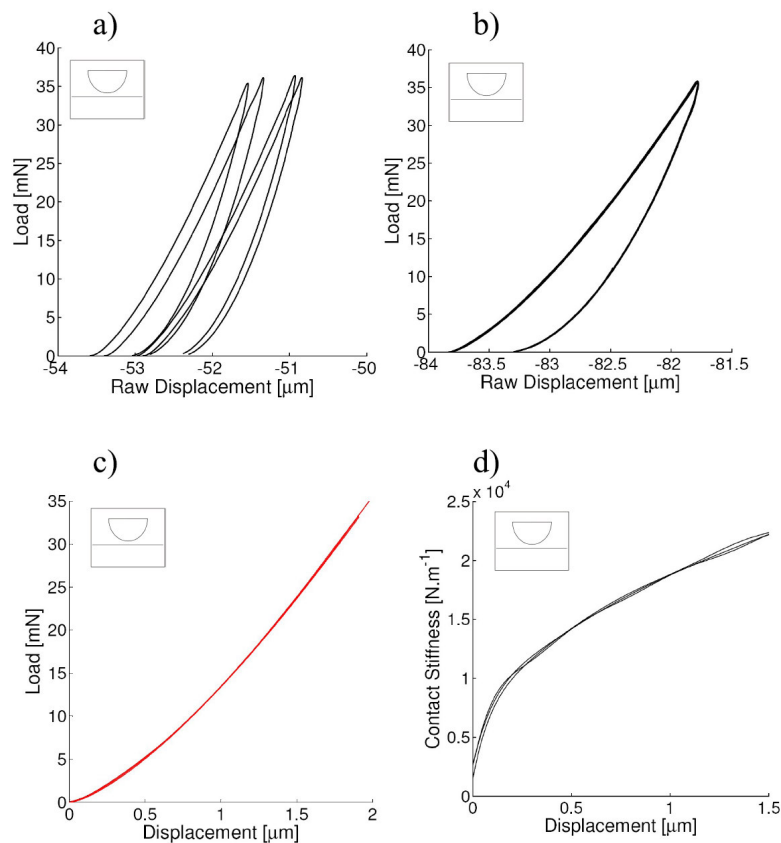


**Figure 2.5:** As Figure 2.4 now for spherical tip.

### Flat-ended punch

Finally the flat punch indenter is investigated; see Figures 2.6a and 2.6b. Figure 2.6a presents the uncorrected case, with shifted load-displacement curves. After the correction procedure, all curves overlap, see Figure 2.6b. Although this indicates that the sample surface is perfectly aligned with respect to the indenter surface, it is observed that the load-displacement curves initially do not show the linear dependency as expected from Equation 2.1, see Figure 2.6b zoom. This indicates the presence of a misalignment type 2, where the tip surface is not perpendicular to the loading axis, implying that an additional alignment procedure is needed.

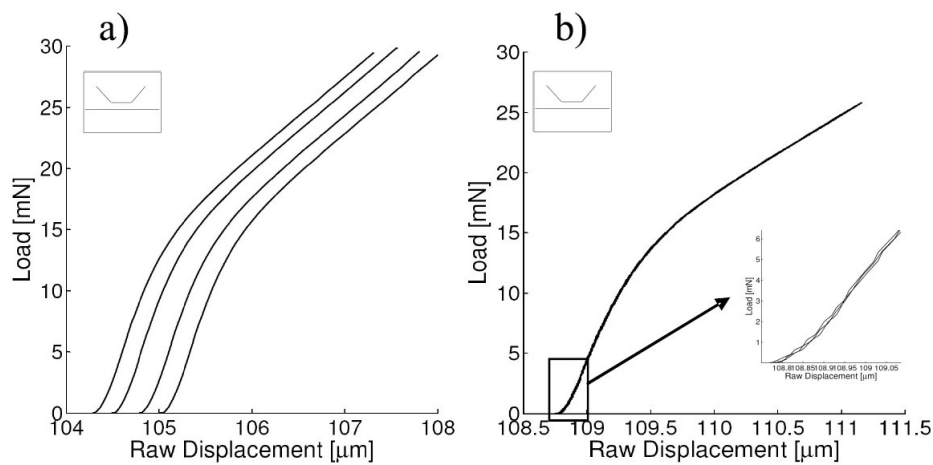


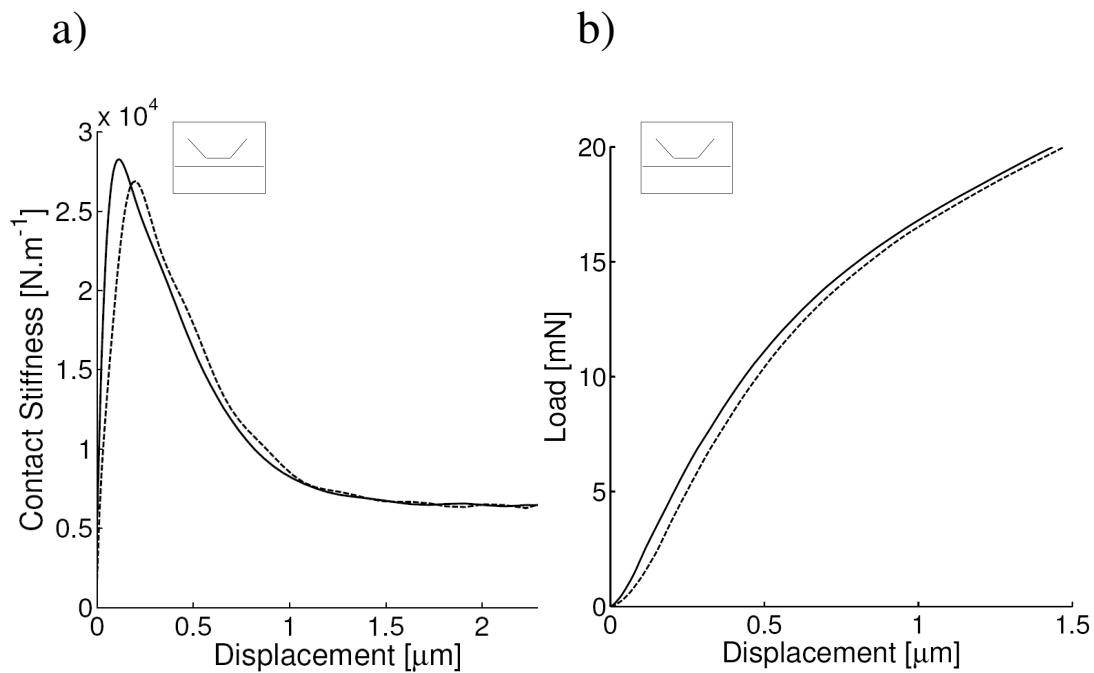
**Figure 2.6:** For flat punch: a) load raw displacement curves when no sample misalignment correction was applied; b) after correction of the sample misalignment using the alignment tool.

The procedure used is based on the fact that the contact stiffness will be maximal in the situation where tip and sample surfaces are parallel. To obtain the maximum contact stiffness a trial and error process is followed where the surface of the sample is first tilted along one rotation axis, plotting the contact stiffness as function of the rotation. This is repeated until the maximum contact stiffness is reached for a certain angle. Next the same procedure is applied along the other rotation axis. The correction values required prove to be always in the range of  $0.2^\circ$  to  $1.2^\circ$  (defined by Equation 2.5)<sup>1</sup>. Figure 2.7a, presents the difference in contact stiffness using procedure 1 (dashed line), only correcting for sample misalignment, and using procedure 2 (solid line), correcting for the total misalignment. It can be observed that procedure 1 does not lead to the highest value of the contact stiffness, whereas procedure 2 does.

Figure 2.7b presents the load displacement curves obtained after procedure 1 (dashed line) and after procedure 2 (solid line). The curves are shifted to lower

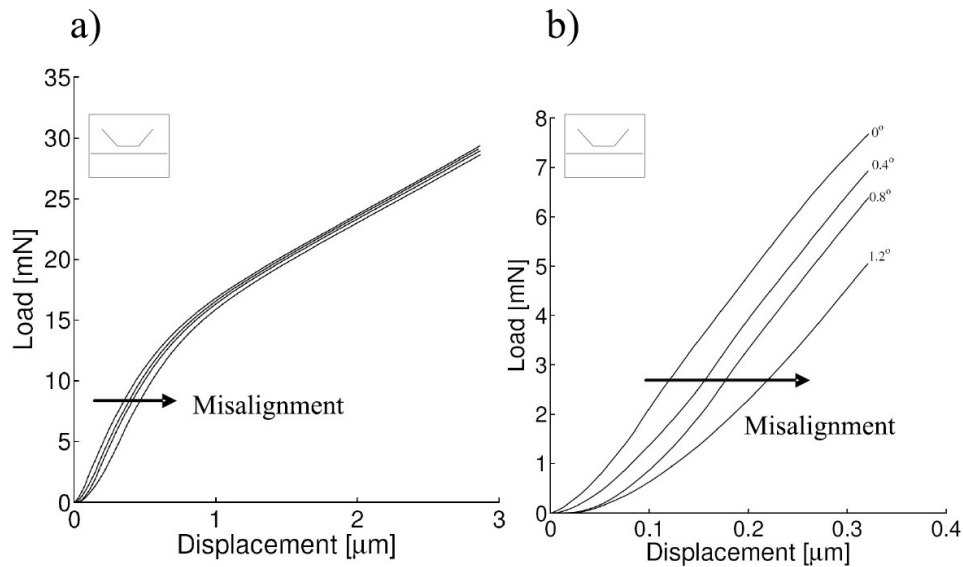
<sup>1</sup> If the tip is removed and replaced in the nanoindenter, misalignment will always be different and a new angle value at which the maximum stiffness is reached will be obtained.

indentation depth and possess a larger linear range when the surfaces of the sample and the tip are parallel. However, even in this situation, the load-displacement curve still exhibits a small non-linearity at indentation depths up to 30 nm. Besides the fact that this could be related to imperfections of the tip's geometry, it could also originate from an intrinsic scale effect. In the latter case the mechanical properties of the material change when approaching a free surface. This phenomena has been observed earlier, and is thought to be related to a decrease of the glass-transition temperature in the vicinity of a free surface [18-20].



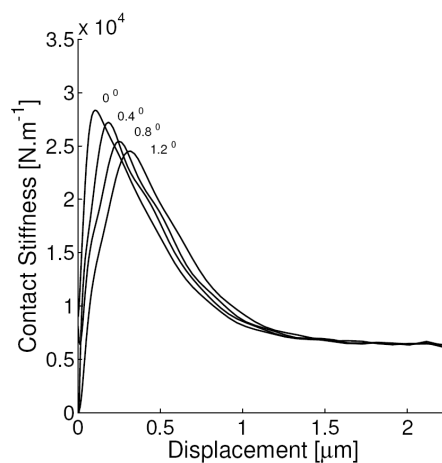
**Figure 2.7:** Comparison between the sample misalignment correction only (dashed line) and the total misalignment correction (solid line): a) for contact stiffness as function of the depth and b) for the load-displacement curve.

Figure 2.8a shows the influence of a stepwise misalignment of the flat indenter on the load-displacement curves. An increasing misalignment angle leads to a shift of the curves to higher displacements (as previously observed). In the case of misalignment, the edge of the tip first touches the surface and at this stage, this is not yet a flat punch indentation. Therefore, Equation 2.1 is no longer applicable. With ongoing indentation, the contact area increases until a full contact between the two surfaces is obtained. When the misalignment angle increases, full contact is reached at larger depth.



**Figure 2.8:** Effect of the sample misalignment for the flat ended punch indentation for angles of  $0^\circ$ ,  $0.4^\circ$ ,  $0.8^\circ$ ,  $1.2^\circ$ : a) load-displacement curves; b) zoom of the load displacement at low indentation depth where the sample misalignment has a strong effect.

Next, the contact stiffness is plotted, as a function of indentation depth, for different misalignment angles, Figure 2.9. At large displacements, in the plastic regime, all the curves obtained for different misalignment angles (from  $0^\circ$  until  $1.2^\circ$ ) are actually overlapping and in this plastic region misalignment has no effect on the contact stiffness. In contrast, in the elastic regime, an increase in misalignment angle results in a clear decrease in stiffness.



**Figure 2.9:** Contact stiffness as function of the displacement for the flat ended punch indentation under sample misalignment angles of  $0^\circ$ ,  $0.4^\circ$ ,  $0.8^\circ$ ,  $1.2^\circ$



To quantify the effect, we plot the elastic modulus as function of the misalignment angle, Figure 2.10. Using the Equation 2.1, the elastic modulus is calculated from the maximum stiffness,  $S_{max}$  from Figure 2.9, by:

$$E = \frac{S_{max}(1-\nu^2)}{2R} \quad (2.9)$$

where  $R$  is the tip's radius and  $\nu$  is Poisson's ratio. A linear relation is found and, for a misalignment angle of  $0^\circ$  and a tip's radius of  $5 \mu\text{m}$ , a value of 2.4 GPa is found for the elastic modulus which agrees well with the commonly accepted value for polycarbonate (2.2 -2.4 GPa) as determined in tensile testing.

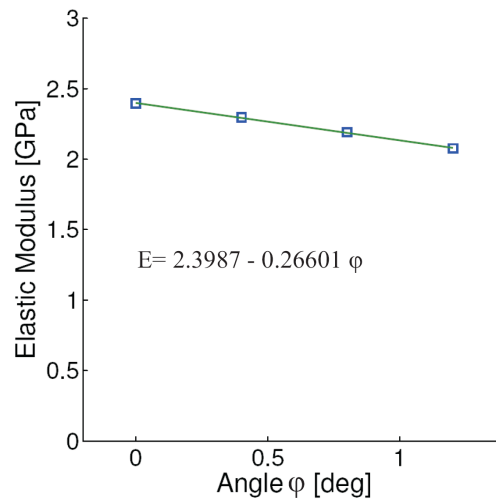


**Figure 2.10:** Linear dependency of the elastic modulus with the misalignment angle on polycarbonate.

### 2.3.3. Possibility for post-indentation correction

At large indentation depth, the contact stiffness is not influenced by misalignment and is constant with the depth and, moreover, from the point of maximum stiffness, curves are only horizontally shifted, see Figure 2.9. Based on these observations, we try to correct for the shift in the indentation depth by applying a linear interpolation. For that, we linearize the load-displacement curves, determine the cut-off on the displacement axis at zero load, and shift all curves with this value to the left, see Figure 2.11a. The result of this correction method is presented in Figure 2.11b. It can be observed that now, in the

plastic regime, all curves overlap, indicating that the misalignment has been effectively corrected for in the rather straight forward manner.

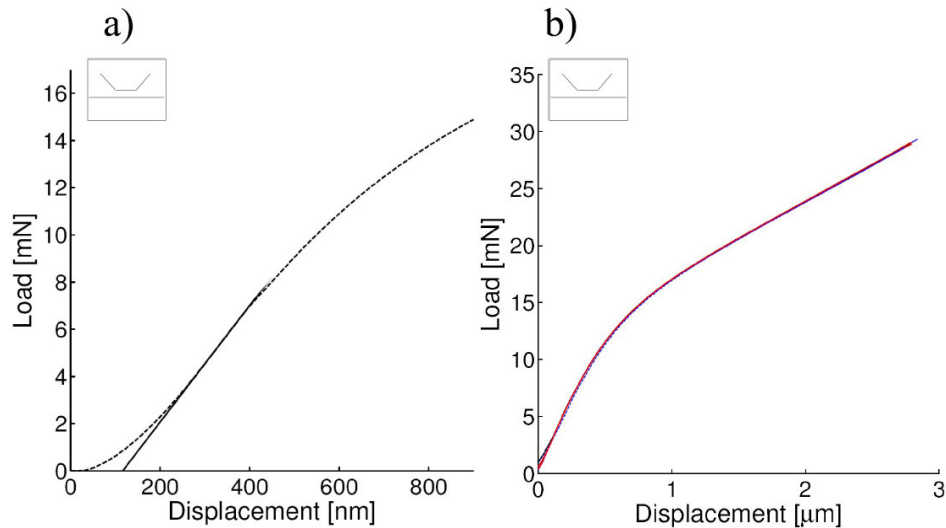


**Figure 2.11:** Method for correcting misalignment, without using the alignment tool: a) a linear fit of the experimental load-displacement curve used to obtain the correction factor; b) load-displacement curves under different misalignment, see Figure 2.8, after correction.

## 2.4. Conclusions

Using our specially designed alignment tool, we carried out a quantitative study of the effect of misalignment on load-displacement curves for three different tip geometries, a Berkovich tip, a spherical tip and a flat-ended punch. It was found that, for angles smaller than  $1.2^\circ$ , sample misalignment has no effect for the Berkovich and the spherical tip. In contrast, flat-ended punch indentation is very sensitive to misalignment. In the linear elastic regime, the contact stiffness decreases with an increasing misalignment angle whereas there is no influence of misalignment on the stiffness at large deformation (in the plastic regime). It was also found that the elastic modulus, calculated from the maximum stiffness, shows a linear dependency on the misalignment angle.

By using the designed alignment tool, we were able to perfectly align samples and tips regardless of the different tip geometry and origin of the misalignment. Finally, we developed a method to correct misalignment effects in flat punch indentation by directly modifying the load-displacement curves.

## References

- [1] I.N. Sneddon, *The relation between load and penetration in the axisymmetric Boussinesq problem for a punch of arbitrary profile*. Int. J. of Eng. Sci., 1965. **3**: p. 47-57.
- [2] H. Hertz, *Über die Berührung Fester Elastischer Körper (On the contact of elastic solids)*. J. Reine Angew. Math., 1881. **92**: p. 156-171.
- [3] K.L. Johnson, *Contact mechanics*, Cambridge University Press. 1985, Cambridge.
- [4] L. Cheng, X. Xia, W. Yu, L.E. Scriven, and W.W. Gerberich, *Flat punch indentation of viscoelastic material*. Journal of Polymer Science B: polymer physics, 2000. **38**(1): p. 10-22.
- [5] Y. Lu and D.M. Shinozaki, *Microindentation testing of inhomogeneous microstructures in welded polyethylene*. Polymer Eng. and Sci., 1997. **37**(11): p. 1815-1824.
- [6] Y. Lu and D.M. Shinozaki, *Deep penetration micro-indentation testing of high density polyethylene*. Mat. Sci. and Eng. A, 1998. **249**: p. 134-144.
- [7] S.C. Wright, Y. Huang, and N.A. Fleck, *Deep penetration of polycarbonate by a cylindrical punch*. Mech. of Mat., 1992. **13**: p. 277-284.
- [8] Y. Lu and D.M. Shinozaki, *Microindentation induced debonding of polymer thin films from rigid substrates*. J. Mater. Sci., 2002. **37**: p. 1283-1293.
- [9] N.X. Randall, R. Christoph, S. Droz, and C. Julia-Schmutz, *Localised micro-hardness measurements with a combined scanning force microscope / nanoindentation system*. Thin Solid Films, 1996. **290-291**: p. 348-354.
- [10] P.H. Sydenham, *Elastic design of fine mechanism in instruments*. J. Phys. E: Sci. Instrum., 1984. **17**: p. 922-930.
- [11] S.T. Smith, V.G. Badami, J.S. Dale, and Y. Xu, *Elliptical flexure hinges*. Rev. Sci. Instrum., 1997. **68**(3): p. 1474-1483.
- [12] Y.M. Tseytlin, *Notch flexure hinges: An effective theory*. Rev. Sci. Instrum., 2002. **73**(9): p. 3363-3368.
- [13] W.C. Oliver and G.M. Pharr, *Measurement of hardness and elastic modulus by instrumented indentation: Advances in understanding and refinements to methodology*. J. Mat. Res., 2004. **19**(1): p. 3-20.
- [14] A.C. Fischer-Cripps, *Nanoindentation*. Second ed. 2004: Springer.
- [15] W.C. Oliver and G.M. Pharr, *An improved technique for determining hardness and elastic-modulus using load and displacement sensing indentation experiments*. J Mater. Res., 1992. **7**(6): p. 1564 - 1583.

- 
- [16] A. Bolshakov and G.M. Pharr, *Influence of pileup on the measurement of mechanical properties by load and depth sensing indentation techniques*. J. Mat. Res., 1998. **13**(4): p. 1049-1058.
- [17] G. Shafirstein, M.G. Gee, S. Osgerby, and S.R.J. Saunders. *Error analysis in nanoindentation*. in Thin Films: Stresses and Mechanical Properties V. 1995. **356**: p. 717-721.
- [18] J.A. Forest, K. Dalnoki-Veress, J.R. Dutcher, A.C. Rowat, and J.R. Stevens. *Disordered Materials and Interfaces*. 1995, Mat. Res. Soc. Symp. Proc., Materials Research Society Pittsburg PA. **407**: p. 131-136.
- [19] J.A. Forest and J. Mattsson, *Reductions of the glass transition temperature in thin polymer films: Probing the length scale of cooperative dynamics*. Phys. Rev. E, 2000. **61**(1): p. R53-R56.
- [20] H.G.H. Van Melick, A.R. van Dijken, J.M.J. den Toonder, L.E. Govaert, and H.E.H. Meijer, *Near-surface mechanical properties of amorphous polymers*. Phil. Mag. A., 2002. **82**(10): p. 2093-2102.

## Appendix

To calculate the total misalignment angle we consider the normal to the surface for the misaligned case to be  $\vec{n} = (n_x, n_y, n_z)$ . After correction of the misalignment, by rotation along the y-axis (by an angle  $\varphi_y$ ) and subsequently along the x-axis (by an angle  $\varphi_x$ ) the normal of the surface should be parallel to the loading axis, which is assumed to be in the z-direction, i.e.  $\vec{n}' = (0,0,1)$ . The rotation can be described by a rotation matrix  $\mathbf{R}$ :

$$\vec{n}' = \mathbf{R}_x \cdot \mathbf{R}_y \cdot \vec{n} = \mathbf{R} \cdot \vec{n}. \quad (2.10)$$

where  $\mathbf{R}_x$  and  $\mathbf{R}_y$  describe the rotation along the x- and y-axis, respectively. It can be shown that the  $\mathbf{R}$  can be expressed as follows, in terms of the rotation angles  $\varphi_x$  and  $\varphi_y$ :

$$\mathbf{R} = \begin{pmatrix} \cos(\varphi_y) & 0 & -\sin(\varphi_y) \\ \sin(\varphi_y)\sin(\varphi_x) & \cos(\varphi_x) & \sin(\varphi_x)\cos(\varphi_y) \\ \cos(\varphi_x)\sin(\varphi_y) & -\sin(\varphi_x) & \cos(\varphi_y)\cos(\varphi_x) \end{pmatrix} \quad (2.11)$$

The combination of Equations 2.10 and 2.11 results in:

$$0 = \cos(\varphi_y) n_x - \sin(\varphi_y) n_z \quad (2.12a)$$

$$0 = \sin(\varphi_y) \sin(\varphi_x) n_x + \cos(\varphi_x) n_y + \sin(\varphi_x) \cos(\varphi_y) n_z \quad (2.12b)$$

$$1 = \cos(\varphi_x) \sin(\varphi_y) n_x - \sin(\varphi_x) n_y + \cos(\varphi_x) \cos(\varphi_y) n_z \quad (2.12c)$$

Elimination of  $n_x$  and  $n_y$  from these equations yields:

$$n_z = \left( \frac{\cos(\varphi_x) \sin^2(\varphi_y)}{\cos(\varphi_y)} + \frac{\sin^2(\varphi_y) \sin^2(\varphi_x)}{\cos(\varphi_y) \cos(\varphi_x)} + \frac{\sin^2(\varphi_x) \cos(\varphi_y)}{\cos(\varphi_x)} + \cos(\varphi_y) \cos(\varphi_x) \right)^{-1} \quad (2.13)$$

The projection of  $\vec{n}$  on the z-axis gives:

$$n_z = \|\vec{n}\| \cdot \cos(\varphi) \quad (2.14)$$

with  $\|\vec{n}\| = \sqrt{n_x^2 + n_y^2 + n_z^2} = 1$  and  $\varphi$  is the total misalignment angle between  $\vec{n}'$  and  $\vec{n}$ .

From equations 2.13 and 2.14 we finally obtain:

$$\varphi = \arccos \left[ \frac{\cos(\varphi_x) \sin^2(\varphi_y)}{\cos(\varphi_y)} + \frac{\sin^2(\varphi_y) \sin^2(\varphi_x)}{\cos(\varphi_y) \cos(\varphi_x)} + \frac{\sin^2(\varphi_x) \cos(\varphi_y)}{\cos(\varphi_x)} + \cos(\varphi_y) \cos(\varphi_x) \right]^{-1} \quad (2.15)$$

It can be proven that the reversal of the order of the rotation operations along the x- and y-axis (see Equation 1) leads to the same result.



## Chapter 3

# Numerical simulation of flat-tip micro-indentation of glassy polymers: influence of loading speed and thermodynamic state

---

### Abstract

Flat-tip micro-indentation tests were performed on quenched and annealed polymer glasses at various loading speeds. The results were analyzed using an elasto-viscoplastic constitutive model that captures the deformation characteristics of a polymer glass: a strain-rate dependent yield stress, strain softening and strain hardening. The advantage of this model is that changes in yield stress due to physical aging are captured in a single parameter.

The two materials studied (polycarbonate (PC) and poly(methyl methacrylate) (PMMA)), were both selected for the specific rate-dependence of the yield stress they display at room temperature. For PC the yield stress increases proportionally with the logarithm of strain-rate, whereas for PMMA, a characteristic change in slope can be observed at higher strain rates.

We demonstrate that, given the proper definition of the viscosity function, the flat-tip indentation response at different indentation speeds can be described accurately for both materials. Moreover, it is shown that the parameter set obtained for each material is also representative for the mechanical response on a *macroscopic* scale. This implies that the thermodynamic state of PC and PMMA can now be determined by fitting a single parameter on a single indentation test.



### 3.1. Introduction

Instrumented indentation is a versatile technique to probe local mechanical properties of films and/or bulk materials [1, 2]. In principle, a well-defined body is pressed into the surface of a material while measuring both applied load and penetration depth. The data obtained can subsequently be analyzed to determine the mechanical properties of the indented material. Especially with respect to elastic modulus quantitative analytical analysis methods are available [3, 4]. With the aid of the elastic-viscoelastic correspondence principle these methods are also applicable to quantitatively assess the viscoelastic properties [5-9]. With respect to the large strain mechanical properties the analysis of indentation data is less straight forward. Even for the determination of the yield strength a direct analytical method or analysis is not available, and an estimate can only be obtained using empirical scaling laws. Although these have been proven to be quite useful, the scaling factor between hardness and yield strength is not universal for all materials [10-12].

The availability of numerical, FEM-based analysis methods created new possibilities. Supported by the development of appropriate finite-strain constitutive relations a detailed analysis of local deformation and stress fields became feasible. An excellent example is the work in Larsson's group on Vickers [13] and Berkovich [14] indentation of elasto-plastic materials. In the case of polymeric materials, the analysis of such contact problem is complicated by their complex large strain behavior, characterized by a pronounced strain-rate and pressure dependence of the yield stress and a post-yield response that is governed by a combination of strain softening and strain hardening. Especially in the case of polymer glasses considerable effort has been directed towards the development of 3D constitutive models that are capable to capture the experimentally observed behavior, e.g. in the group of Mary Boyce at MIT [15-17], the group of Paul Buckley in Oxford [18-20], and in our Eindhoven group [21-23]. These developments enabled a quantitative analysis of localization and failure in glassy polymers [22, 24-29], and revealed the crucial influence of the intrinsic post-yield characteristics on macroscopic strain localization.

Van Melick *et al.* [28] were the first to apply such a constitutive model to spherical-tip indentation of polystyrene (PS), in order to analyze radial craze formation. They demonstrated that the load-penetration depth curves could be well reproduced for different indentation speeds by numerical simulations using the "Eindhoven" model [21]. In a subsequent study, Swaddiwudhipong *et al.* [30] showed that the same model was unable to describe the Berkovich indentation response of polycarbonate (PC). To reproduce the response at different indentation speeds correctly, they required an additional strain gradient effect. It should be noted, however, that they adopted the parameters for polycarbonate from Govaert *et al.* [21] without verifying whether this set was appropriate for the thermodynamic state of their own polycarbonate samples. In a more recent study, Anand and Ames [31] presented an extension of the BPA-model [16], which proved successful in describing the conical-tip indentation of PMMA, albeit at a single indentation rate.

In the present study, we demonstrate that the "Eindhoven" model [22] is also capable to quantitatively describe the indentation response of PC and PMMA over a

range of indentation speeds. A flat-ended cone is chosen as indenter body, since this specific tip geometry results in a load-penetration depth curve in which elastic and plastic ranges are clearly distinguishable. At low indentation depth the response is governed by elastic deformation, whereas at large depths plastic deformation sets in, leading to a marked change in slope and resulting in a characteristic knee-shaped load-displacement curve [11, 32, 33]. Moreover, we show that an excellent description of the experimental indentation results is accomplished by using a parameter set which also quantitatively describes the materials mechanical response in *macroscopic* testing.

## 3.2. Finite strain deformation of glassy polymers

### 3.2.1. Phenomenology

To study the intrinsic stress-strain response of polymers, an experimental set-up is required in which the sample can deform homogeneously up to large plastic deformations. Examples of such techniques are uniaxial compression tests [15, 34] or video-controlled tensile tests [35]. An illustrative example of the intrinsic stress-strain response of a polymer glass is presented in Figure 3.1a. Typical features of the post-yield plastic deformation at large strains are strain softening, the decrease in true stress that is observed after passing the yield point, and strain hardening at large deformations. Strain hardening is generally interpreted as the result of a stress contribution of the orienting molecular network [15, 34, 36, 37]. Strain softening is closely related to the fact that polymer glasses are not in a state of thermodynamic equilibrium. Over time the glass will strive towards equilibrium, a process usually referred to as physical aging [38], and, as a result, its mechanical properties change. This is demonstrated in Figure 3.1a which compares the intrinsic response of two samples with different thermodynamic state. It is clear that physical aging results in an increase of both modulus and yield stress, but upon plastic deformation the differences between curves of originally different thermodynamic state disappear and eventually they fully coincide at a strain of approximately 0.3. Apparently all influence of thermal history is erased at that strain and both samples are transformed to a similar state, the so-called mechanically rejuvenated state. From Figure 3.1a it is clear that an increase in yield stress, due to a thermal treatment, directly implies an increase in strain softening. The influence of molecular weight on the intrinsic response is usually small and negligible [20, 22], which makes thermal history the key factor in influencing the intrinsic properties of a specific polymer glass. The thermal history is also reflected in the long-term failure behavior of polymer glasses. This was demonstrated for PC, where an annealing treatment, leading to an increase in yield stress, improved the life-time under constant stress by orders of magnitude [39].

The intrinsic stress-strain response of glassy polymers also displays a pronounced dependence on the time-scale of the experiment. This is illustrated in Figure 3.1b, where the strain rate dependence of the compressive stress-strain response of poly(methylmethacrylate) (PMMA) is shown [40]. It is clear that with increasing strain rate the overall stress level in the yield and post-yield range increases. Also the amount of strain softening and strain hardening appears subject to change. At strain rates over  $3 \cdot 10^{-2}$

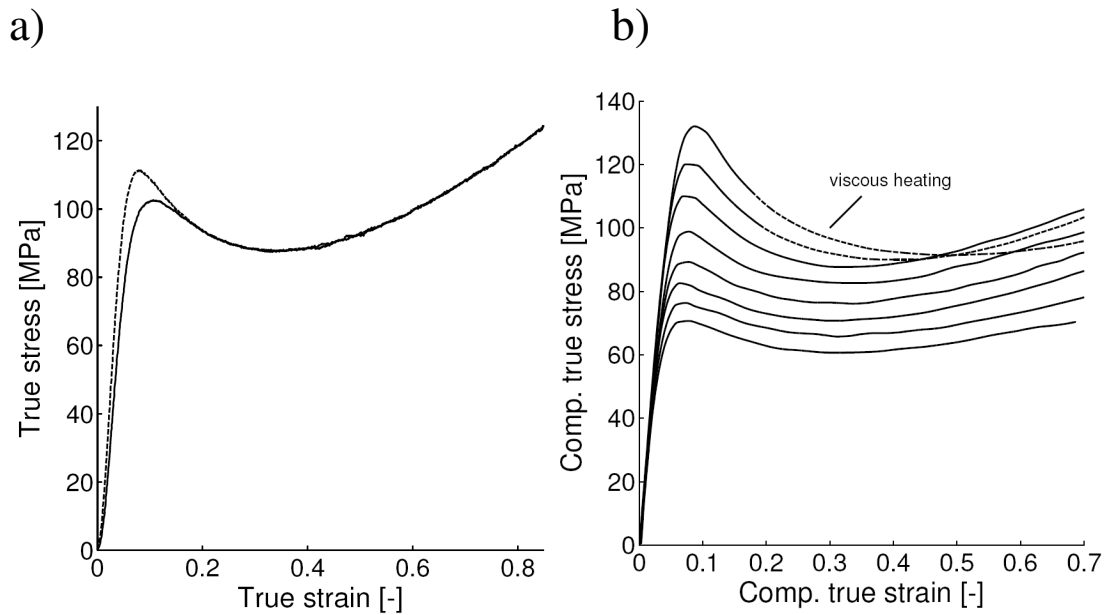


**Figure 3.1:** Stress-strain response of PMMA in uniaxial compression, a) influence of thermal history where the sample was annealed (dashed line) and quenched (solid line) and b) influence of strain rate.

$s^{-1}$  the material heats up as a result of viscous dissipation, and, as a result, strain hardening disappears [41].

The strain rate dependence of the yield stress is shown in Figure 3.2a for PMMA and polycarbonate (PC). For the latter the yield stress increases linearly with the logarithm of the strain rate, which indicates that in this range of strain rates the deformation of PC is governed by a single molecular relaxation process [42, 43], the amorphous  $\alpha$ -transition (main-chain segmental motion). Although the present work only focuses on the isothermal response, it is relevant to note that the  $\alpha$ -stress contribution displays an Arrhenius type of temperature dependence that leads to a horizontal shift of the yield stress characteristic along the logarithmic strain rate axis: a behavior that is generally referred to as thermo-rheologically *simple*.

In the case of PMMA, the strain-rate dependence of the yield stress displays a clear change in slope which was shown to be related to the onset of a stress contribution of a second molecular process, the  $\beta$ -transition [44, 45]; a secondary glass transition related to side-chain mobility. A successful description of such a yield response is obtained using a Ree-Eyring approximation, where, as schematically represented in Figure 3.2b, it is assumed that each process can be described with an Eyring flow rule, whereas the stress contributions of both molecular mechanisms are additive [46]. In the case of PMMA, it should be noted that each process possesses its own characteristic activation energy, implying that curves measured at different temperatures will no longer coincide by horizontal shifting. A correct translation to other temperatures can only be

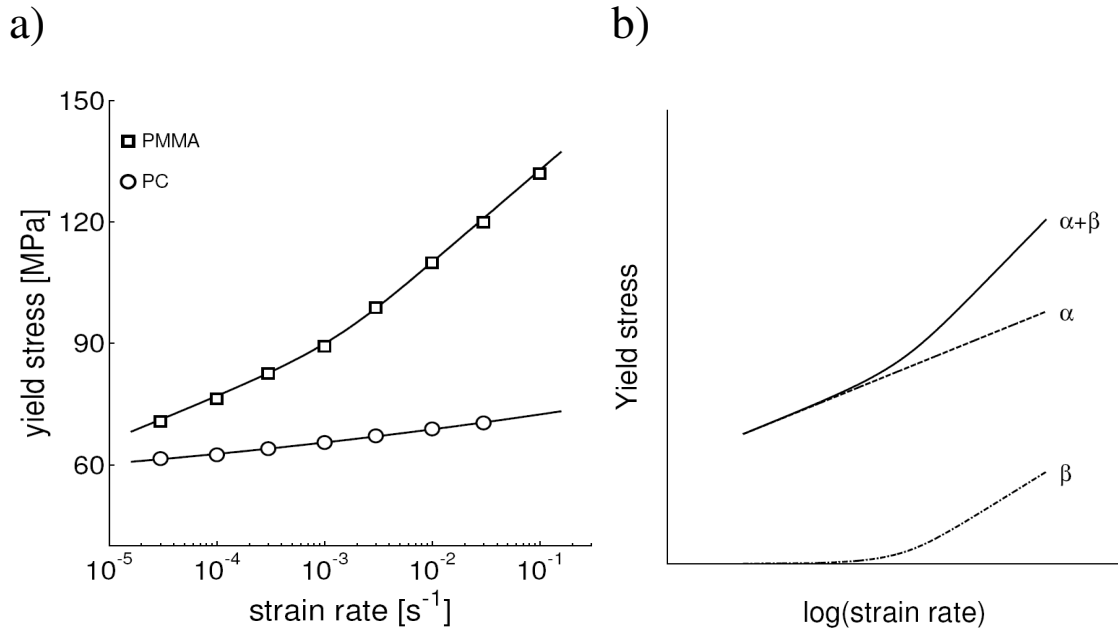


**Figure 3.2:** a) yield stress of PMMA and PC in uniaxial compression as a function of strain rate; b) decomposition of the strain rate dependence of the yield stress of into two separate molecular contributions [45].

achieved by application of rate-temperature superposition on each contribution separately: this behavior is generally referred to as thermo-rheologically *complex*.

### 3.2.2. Numerical model, the “Eindhoven” model

In the present study we employ a 3D elasto-viscoplastic constitutive model that accurately captures the deformation characteristics of polymer glasses [21, 23, 39, 47]. The basis of this constitutive model is the decomposition of the total stress into two separate contributions, as first proposed by Haward and Thackray [36]:

$$\boldsymbol{\sigma} = \boldsymbol{\sigma}_s + \boldsymbol{\sigma}_r \quad (3.1)$$

here  $\boldsymbol{\sigma}_r$  denotes the strain hardening contribution that is attributed to molecular orientation of the entangled network, and in this case described with a Neo-Hookean elastic expression [21, 37]:

$$\boldsymbol{\sigma}_r = G_r \tilde{\mathbf{B}}^d \quad (3.2)$$

where  $G_r$  is the strain hardening modulus and  $\tilde{\mathbf{B}}^d$  the deviatoric part of the isochoric left-Cauchy-Green strain tensor.

The driving stress  $\boldsymbol{\sigma}_s$  is attributed to intermolecular interactions on a segmental scale [23, 39] and is split up in a hydrostatic ( $\boldsymbol{\sigma}_s^h$ ) and a deviatoric part ( $\boldsymbol{\sigma}_s^d$ ) [47, 48] :

$$\boldsymbol{\sigma}_s = \boldsymbol{\sigma}_s^h + \boldsymbol{\sigma}_s^d = K(J-1)\mathbf{I} + G\tilde{\mathbf{B}}_e^d \quad (3.3)$$

where  $K$  is the bulk modulus,  $J$  is the relative volume change,  $G$  is the shear modulus, and  $\tilde{\mathbf{B}}_e^d$  is the deviatoric part of the isochoric elastic left Cauchy-Green strain tensor. The evolution of  $J$  and  $\tilde{\mathbf{B}}_e$  are implicitly given by:

$$\dot{J} = J \cdot \text{tr}(\mathbf{D}) \quad (3.4)$$

$$\overset{\circ}{\tilde{\mathbf{B}}}_e = (\mathbf{D}^d - \mathbf{D}_{pl}^d) \cdot \tilde{\mathbf{B}}_e + \tilde{\mathbf{B}}_e \cdot (\mathbf{D}^d - \mathbf{D}_{pl}^d) \quad (3.5)$$

where  $\overset{\circ}{\tilde{\mathbf{B}}}_e$  is the Jaumann derivative of  $\tilde{\mathbf{B}}_e$ ,  $\mathbf{D}^d$  is the deviatoric part of the rate of deformation tensor. Crucial for an adequate evolution of the driving stress is the plastic part of the rate of deformation tensor  $\mathbf{D}_{pl}$ , which is related to the deviatoric driving stress by a non-Newtonian flow rule:

$$\mathbf{D}_{pl} = \frac{\boldsymbol{\sigma}_s^d}{2\eta(\bar{\tau}, p, S_a)} \quad (3.6)$$

A correct expression for the solid state viscosity  $\eta$  is essential in obtaining an accurate description of the 3D stress-strain response. For glassy polymers, this choice mainly depends on the number of molecular relaxation mechanisms that contribute to the stress. In the simplest case only a single molecular mechanism is active, the  $\alpha$ -process (main-chain segmental motion), and an expression for  $\eta$  can be obtained by taking the pressure-modified Eyring flow equation [22, 49, 50] as a starting point. In the isothermal case this leads to:

$$\dot{\gamma}_{pl}(\bar{\tau}, p, S) = \underbrace{\dot{\gamma}_{0,\alpha r}}_{\text{I}} \cdot \underbrace{\sinh(\bar{\tau}/\tau_{0,\alpha})}_{\text{II}} \cdot \underbrace{\exp(-\mu p/\tau_{0,\alpha}) \cdot \exp(-S)}_{\text{III}} \quad (3.7)$$

where  $\dot{\gamma}_{pl}$  represents the equivalent plastic shear rate [51]. The part marked (I), where  $\bar{\tau}$  is the equivalent shear stress [52], represents the stress dependence of the viscosity governed by the parameter  $\tau_{0,\alpha}$ . Part (II), where  $p$  is the hydrostatic pressure [53], yields the pressure dependency governed by the parameter  $\mu$ . Part (III) represents the dependence of the viscosity on the thermodynamic state of the material expressed by the state parameter  $S$ . Finally  $\dot{\gamma}_{0,\alpha r}$  is a pre-exponential factor representative for the rejuvenated, unaged state, where the index  $\alpha$  refers to the identity of the contributing molecular process.

Equation 3.7 leads to the following expression for the stress-dependence of the solid state viscosity:

$$\eta_{\alpha}(\bar{\tau}, p, S) = \frac{\bar{\tau}}{\dot{\gamma}_{pl}(\bar{\tau}, p, S)} = \eta_{0,\alpha r} \cdot \left[ \frac{\bar{\tau}/\tau_{0,\alpha}}{\sinh(\bar{\tau}/\tau_{0,\alpha})} \right] \cdot \exp(\mu p/\tau_{0,\alpha}) \cdot \exp(S) \quad (3.8)$$

where  $\eta_{0,\alpha r}$  ( $= \tau_{0,\alpha}/\dot{\gamma}_{0,\alpha r}$ ) is the zero-viscosity for the rejuvenated state. The part between brackets can be regarded as a stress-dependent shift factor that equals 1 at equivalent shear stresses lower than  $\tau_{0,\alpha}$  and decreases exponentially with increasing equivalent shear stress.

The dependence of the viscosity on physical aging and rejuvenation (strain softening) is included by defining [22]:

$$S = S_a(t) \cdot R_{\gamma}(\bar{\gamma}_{pl}) \quad (3.9)$$

Here the parameter  $S_a$  can be regarded as a state parameter that uniquely determines the current state of the material. Evolution of  $S_a$  with time allows us to capture the time dependent change of mechanical properties as a result of physical aging [22]. In the present investigation, however, we will only consider materials with different initial  $S_a$  values (obtained by application of different thermal histories). The function  $R_{\gamma}$  describes the strain softening process, the erasure of thermal history with plastic deformation. It is expressed as:

$$R_\gamma(\bar{\gamma}_{pl}) = \frac{\left(1 + (r_0 \cdot \exp(\bar{\gamma}_{pl}))^{r_1}\right)^{\frac{r_2-1}{r_1}}}{\left(1 + r_0^{r_1}\right)^{\frac{r_2-1}{r_1}}} \quad (3.10)$$

where  $r_0$ ,  $r_1$  and  $r_2$  are fitting parameters, and  $\bar{\gamma}_{pl}$  denotes the equivalent plastic strain. The initial value of  $R_\gamma(0)=1$ , and with increasing equivalent plastic strain  $R_\gamma$  decreases to zero.

The essence of the influences of physical aging and strain softening, modeled within the state parameter  $S$  (Equation 3.8), is illustrated in Figure 3.3a which shows the strain-rate dependence of the yield stress resulting from Equations 3.8 and 3.9. In the reference state, i.e. the fully rejuvenated state, the parameter  $S_a$  is initially equal to zero. With physical aging (also during processing) the value of  $S_a$  increases, which leads to a shift of the yield stress versus strain rate characteristic along the logarithmic strain rate axis. At a constant strain rate, the result is an increase in yield stress compared to that of the rejuvenated state. Upon deformation, the increasing equivalent plastic strain  $\bar{\gamma}_{pl}$  triggers strain softening (Equation 3.10) and the yield stress shifts back to that of the rejuvenated state. As a result, the yield stress drops with increasing strain and the intrinsic stress-strain curve evolves back to that of the rejuvenated state (see Figure 3.3b).

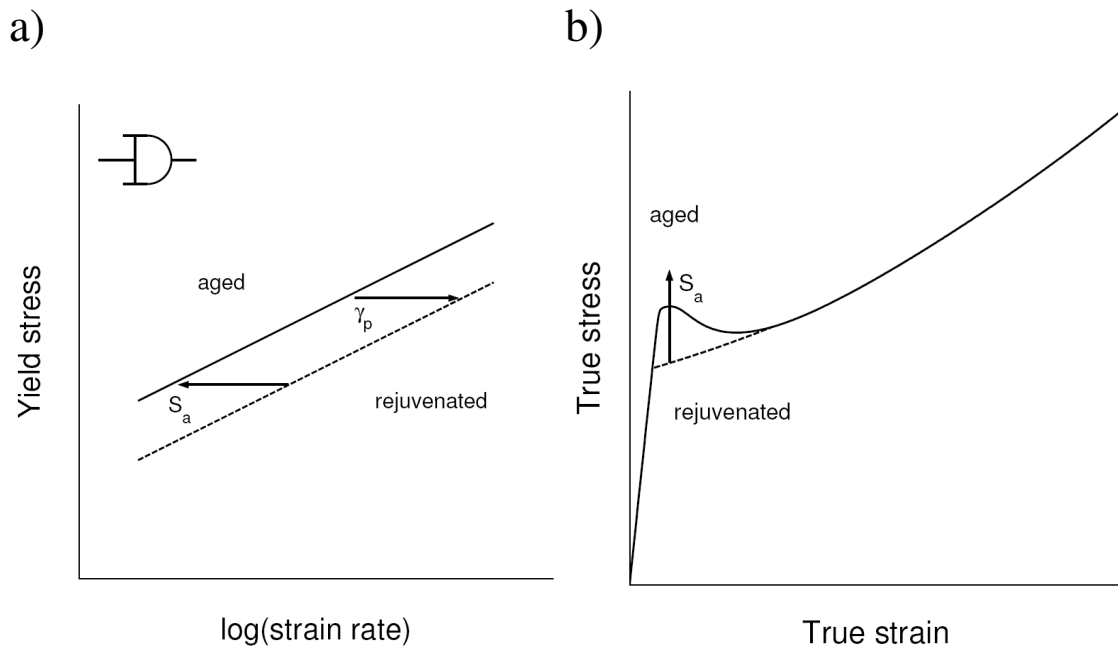


**Figure 3.3:** a) schematic representation of the influence of the thermal history and strain softening on the strain-rate dependence of the yield stress; b) model prediction of the intrinsic stress-strain curve indicating the influence of the physical aging.

It is important to note that the parameters in the model (see Table 3.1 [39]) proved to be independent of the molecular weight distribution of the polymers, PC in this example, and the key parameter, needed to adjust for differences in thermal history (illustrated in Figure 3.1), is the initial value of the state parameter  $S$ :  $S_a$ . This parameter can, in principle, be determined directly from the yield stress value of a single tensile test [22, 39], or, if the thermal history during processing is known, it can be calculated directly [54, 55].

Equations 3.7 and 3.8 both describe a linear increase of the yield stress with the logarithm of the strain rate, a situation that can be observed for all glassy polymers, albeit over a limited range of temperatures and strain rates. When studied over a sufficiently large range of temperatures and strain rates, most glassy polymers reveal a change of slope that is related to the stress contribution of a secondary relaxation mechanism (generally referred to as the  $\beta$ -process) [43, 45, 56]. A successful description of such a yield response can be obtained using the Ree-Eyring model [46], where it is assumed that both molecular relaxation mechanisms act in parallel, implying that the stress contributions of both are additive:

$$\tau_{tot} = \tau_{\alpha} + \tau_{\beta} \quad (3.11)$$

This approach has been successfully employed to describe the strain rate dependence of the yield stress of various amorphous and semi-crystalline polymers [44, 45, 56-59]. An expression for the individual stress contributions can be obtained by rewriting the pressure-modified Eyring flow expression (Equation 3.7) in terms of equivalent shear stress:

$$\bar{\tau}_{tot} = \tau_{0,\alpha} \cdot \sinh^{-1} \left( \frac{\dot{\bar{\gamma}}_{pl}}{\dot{\bar{\gamma}}_{0,\alpha r}} \cdot \exp \left( \frac{\mu_{\alpha} P}{\tau_{0,\alpha}} \right) \cdot \exp(S_a) \right) + \tau_{0,\beta} \cdot \sinh^{-1} \left( \frac{\dot{\bar{\gamma}}_{pl}}{\dot{\bar{\gamma}}_{0,\beta e}} \cdot \exp \left( \frac{\mu_{\alpha} P}{\tau_{0,\alpha}} \right) \right) \quad (3.12)$$

While the expression for the  $\beta$ -contribution is equivalent to that of the  $\alpha$ -process, there are two amendments. To a first approximation we assume that the pressure dependence of the  $\beta$ -contribution is identical to that of the  $\alpha$ -process. Moreover, since for the materials under investigation (PC and PMMA) the  $\beta$ -contribution is already in its equilibrium state [60] and does not change position during aging, there appears no use for a state parameter  $S_{a,\beta}$ . The state is fixed by the equilibrium value of  $\dot{\bar{\gamma}}_{0,\beta}$ ;  $\dot{\bar{\gamma}}_{0,\beta e}$ .

Here we follow an alternative route, where we capture the slope change in a single viscosity expression. To accomplish this we first approach the response of the material in the  $\alpha+\beta$ -range, where both the  $\alpha$ - and the  $\beta$ -process contribute to the stress, as a single flow process:



$$\dot{\gamma}_{pl}(\bar{\tau}, p) = \dot{\gamma}_{0,\alpha+\beta} \cdot \sinh\left(\frac{\bar{\tau}}{\tau_{0,\alpha+\beta}}\right) \cdot \exp\left(\frac{\mu_\alpha p}{\tau_{0,\alpha}}\right) \quad (3.13)$$

where again it is assumed that the pressure dependence of the  $\alpha+\beta$  process is identical to that of the  $\alpha$ -process. Changes in thermodynamic state are captured in the pre-exponential factor  $\dot{\gamma}_{0,\alpha+\beta}$ . Equation 3.13 leads to an expression for the stress- and temperature dependence of the solid state viscosity in the  $\alpha+\beta$ -range :

$$\eta_{\alpha+\beta}(\bar{\tau}, p) = \frac{\bar{\tau}}{\dot{\gamma}_{pl}(\bar{\tau}, p)} = \eta_{0,\alpha+\beta} \cdot \left[ \frac{\bar{\tau}/\tau_{0,\alpha+\beta}}{\sinh(\bar{\tau}/\tau_{0,\alpha+\beta})} \right] \cdot \exp(\mu_\alpha p/\tau_{0,\alpha}) \quad (3.14)$$

where:

$$\eta_{0,\alpha+\beta}(S_a) = \frac{\tau_{0,\alpha+\beta}}{\dot{\gamma}_{0,\alpha+\beta}(S_a)}; \tau_{0,\alpha+\beta} = \tau_{0,\alpha} + \tau_{0,\beta}; \quad (3.15)$$

and

$$\dot{\gamma}_{0,\alpha+\beta}(S_a) = \exp\left(\frac{\tau_{0,\alpha} [\ln(\dot{\gamma}_{0,\alpha r}) - S_a] + \tau_{0,\beta} \ln(\dot{\gamma}_{0,\beta e})}{\tau_{0,\alpha+\beta}}\right) \quad (3.16)$$

To obtain a single viscosity function that covers both the  $\alpha$ -range as well as the  $\alpha+\beta$ -range, we define the total viscosity as:

$$\begin{aligned} \eta_{tot}(\bar{\tau}, p) &= \eta_\alpha + \eta_{\alpha+\beta} \\ &= \eta_{0,\alpha r} \cdot \left[ \frac{\bar{\tau}/\tau_{0,\alpha}}{\sinh(\bar{\tau}/\tau_{0,\alpha})} + \frac{\eta_{0,\alpha+\beta}(S_a)}{\eta_{0,\alpha r} \cdot \exp(S_a)} \cdot \frac{\bar{\tau}/\tau_{0,\alpha+\beta}}{\sinh(\bar{\tau}/\tau_{0,\alpha+\beta})} \right] \\ &\quad \cdot \exp(\mu_\alpha p/\tau_{0,\alpha}) \cdot \exp(S_a \cdot R_\gamma(\bar{\gamma}_p)) \end{aligned} \quad (3.17)$$

A schematic representation of this decomposition is given in Figure 3.4a. The expression between brackets in Equation 3.17 is again a stress-dependent shift factor. Its value equals 1 at shear stresses well below  $\tau_0$ , and decreases towards zero with increasing shear stress. An essential consequence of Equation 3.17 is that the  $\alpha$ - and the  $\beta$ -contribution both display identical softening. As illustrated in Figure 3.4b, upon plastic deformation, the yield stress characteristic shifts horizontally along the logarithmic strain rate without any shape change.

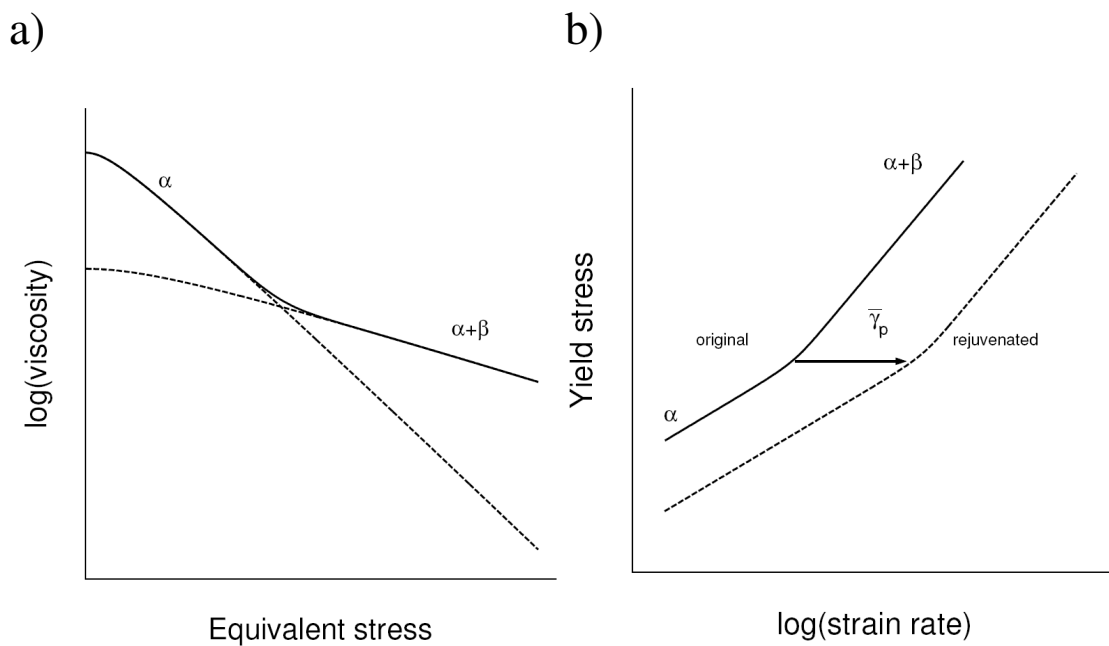


**Figure 3.4:** a) schematical representation of the decomposition of the stress-dependence of the viscosity of a thermo-rheologically complex material into two separate parts; the  $\alpha$  and the  $\alpha+\beta$  viscosity function; b) influence of strain softening on the strain-rate dependence of the yield stress.

### 3.3. Experimental

#### 3.3.1. Materials and sample preparation

##### *Materials*

The materials used in this study are polycarbonate, PC, (Makrolon<sup>®</sup>, Bayer), obtained in the form of extruded sheet of 3 mm thickness, and poly(methylmetacrylate), PMMA (Perspex<sup>®</sup>, ICI) obtained in the form of extruded rod of 6 mm diameter.

*Sample preparation: PC*

For planar extension tests, rectangular samples with a dogbone-shaped cross-section were milled from the sheet, see Govaert *et al.* [50], with in the testing region a thickness of 1.7 mm over a length of 10 mm and a width of 50 mm. Because of the large width-to-length ratio the contraction of the material is constrained, creating a plane strain condition [61]. For simple shear tests, samples similar to those used in the planar tests were used, now with a width of 100 mm instead of 50 mm. With a gauge length of 10 mm, this results in an aspect ratio of 10. To avoid any influence of orientation effects due to the extrusion process all samples were taken from the same direction. For the uniaxial tensile tests, samples according to ASTM D638 were milled from the extruded sheet. To avoid an influence of a processing-induced yield stress distribution over the thickness of the samples [55], the tensile bars were milled to a thickness of 1.7 mm, i.e. identical to that of the test section of the samples for planar extension and shear.

To enable a direct comparison between the indentation tests and the conventional macroscopic tests, indentation experiments were performed on a cross-section of a planar extension sample. A small specimen was cut from the gauge-section of the sample and subsequently the cross-sectional surface was microtomed (cryogenic cut) to obtain a smooth surface. Flat punch indentation tests were then performed in the middle of the sample area. For other indentation tests, samples of a size of 10 mm x 10 mm were cut from the extruded PC sheet.

To change the thermodynamic state of the material, some of the samples were annealed at 120 °C for 48 hours in an air circulated oven and subsequently slowly air-cooled to room temperature.

*Sample preparation: PMMA*

Cylindrical samples of  $\varnothing 6 \times 6$  mm were cut from the extruded rod. The end-faces of the cylinders were machined to optical quality employing a precision turning process with a diamond tool. Indentation and uniaxial compression tests were performed on the same samples. To vary their thermodynamic state, some samples were annealed at 120 °C for 5 days in an air circulated oven and subsequently slowly air-cooled to room temperature.

### 3.3.2. Techniques

Indentation experiments were performed using a nano-indenter XP (MTS Nano-Instruments, Oak Ridge, Tennessee) under displacement control. The geometry of the tip was a flat-ended cone, chosen for the fact that the elastic and the plastic regions in the load-displacement curve can be clearly distinguished. Unfortunately this flat-tip geometry has the drawback that the force-displacement response is very sensitive to tip-sample misalignment. This problem was solved by sample re-alignment using a specially designed alignment tool. Details on the alignment procedure can be found in chapter 2 of this thesis and in reference [62]. The geometry of the tip was characterized using SEM and AFM and proved to have a tip-diameter of 10  $\mu\text{m}$  (Figure 3.5a), a cone angle of 72° (see Figure 3.5b higher SEM picture), and an edge radius of 1  $\mu\text{m}$  (Figure 3.5b lower picture).

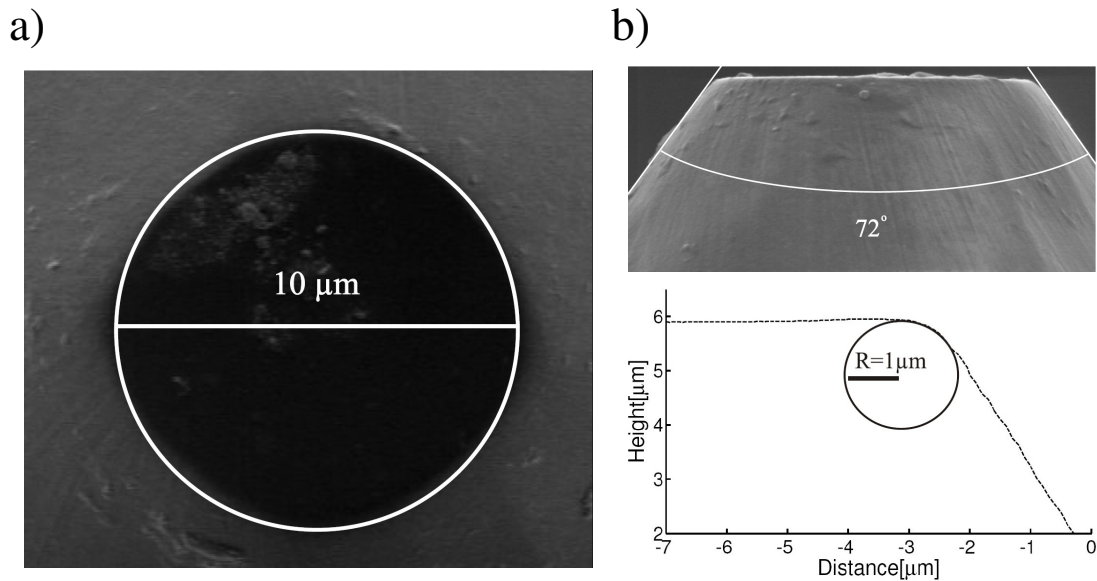


**Figure 3.5:** Characterization of the tip: a) top view SEM picture, b) side view SEM picture (higher picture) with tip profile obtained by AFM (lower picture).

Uniaxial compression tests were performed on a servo-hydraulic MTS Elastomer Testing System 810. The specimens were cylindrical shaped and compressed under true strain control, at constant true strain rates of  $10^{-4}$  to  $10^{-2} \text{ s}^{-1}$  between two parallel, flat steel plates. Friction between samples and plates was reduced by an empirically optimized method. Onto the sample ends a thin film (3M 5480, PTFE skived film tape) was applied, and the contact area between steel and tape was lubricated using a 1:1 mixture of liquid soap and water. During the test no bulging of the sample was observed, indicating that the friction was sufficiently reduced.

Uniaxial and planar tensile tests were performed on a Zwick Z010 tensile tester, at constant linear strain-rates of  $10^{-5}$ - $10^{-1} \text{ s}^{-1}$ . Shear tests were performed on a Zwick 1475 at shear rates ranging from  $10^{-5}$ - $10^{-2} \text{ s}^{-1}$ . Stress-strain curves were recorded and, where appropriate, true stresses were calculated assuming a constant sample volume.

### 3.3.3. Numerical simulations

Axisymmetric simulations were performed using the Marc/Mentat finite element package. The contact between indenter and sample was assumed to be frictionless. In the axisymmetric model, the polymer sample was chosen large enough to prevent the edges from influencing the stress-distribution, and the indenter was modeled as a solid body; the flat-ended cone with the geometrical specifications as determined by SEM and AFM (see Figure 3.5) was used.

The finite element mesh used for the simulation is shown in Figure 3.6. To exclude any mesh-dependence a stepwise element refinement was performed until the

solution converged to a steady, mesh independent, result. In order to prevent excessive computation times the mesh refinement was restricted to areas of interest (see Figure 3.6).

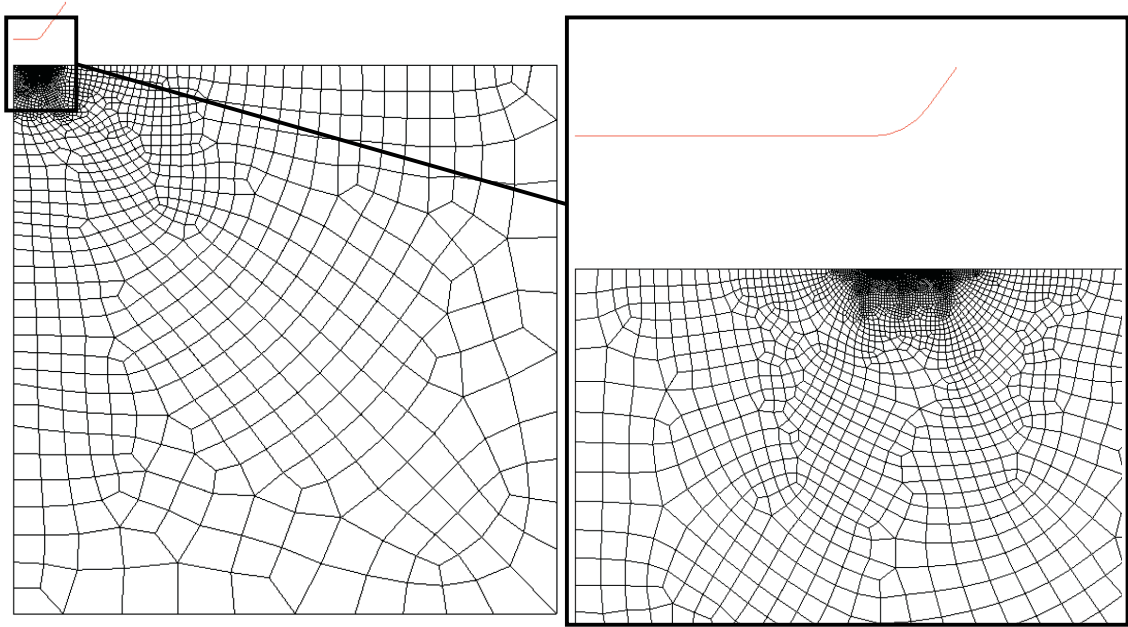


**Figure 3.6:** Mesh used to simulate the indentation tests.

## 3.4. Results and discussion

### 3.4.1. Thermorheologically simple behavior: PC

#### *Material characterization*

In the case of PC, only a single molecular process contributes to the yield stress which implies that the viscosity function defined in Equation 3.8 can be applied. Besides the parameters in this expression ( $\eta_{0, \alpha r}$ ,  $\tau_{0, \alpha s}$ ,  $\mu$ ,  $r_0$ ,  $r_1$ ,  $r_2$ ), the model requires the determination of the strain hardening modulus  $G_r$ , the elastic shear modulus  $G$  and the bulk modulus  $K$ . Most of these parameters can be determined from fitting the results of uniaxial compression tests at different strain rates. A proven strategy is to start by fitting the response of a rejuvenated material ( $S_a = 0$ ) in the strain hardening regime of the experimental curves, which yields the values for  $\tau_{0, \alpha s}$ ,  $\eta_{0, \alpha r}$  and  $G_r$ . Softening can be added by using the aged curve of the sample and  $r_0$ ,  $r_1$ ,  $r_2$  and  $S_a$  can be determined.

Next, we need the values of the elastic bulk modulus  $K$ , the shear modulus  $G$ , and the pressure dependence  $\mu_\alpha$ . The value of  $K$  is calculated from the values of the elastic modulus  $E$  and the Poisson ratio  $\nu$ . The latter were determined in a uniaxial tensile test,

yielding values of 2250 MPa for the elastic modulus  $E$  and a value of 0.4 for the Poisson ratio  $\nu$  [47]. Using the interrelations:

$$K = \frac{E}{3(1-2\nu)} \quad (3.18)$$

a value of 3750 MPa is found for the bulk modulus  $K$ . In the present, single mode, approach, the elastic shear modulus  $G$  is first chosen slightly too low such that the predicted yield strain approximately equals the experimentally observed one; this facilitates the characterization of the post-yield response. For polycarbonate a value of  $G = 320$  MPa proves optimal.

An excellent method to obtain the pressure dependence  $\mu$  is by performing experiments directly under superimposed hydrostatic pressure [63-65]. Therefore,  $\mu$  is determined by numerically predicting the yield data obtained from compression tests at different true strain rates and, finally, from the tensile tests under superimposed hydrostatic pressure, as reported by Christiansen *et al.*[63]. Figures 3.7a and 3.7b show that an excellent description is obtained using the material parameters given in Table 3.1 with an initial  $S_a$ -value of 27.0 for the compression, and 34.0 for the yield experiments, representing the difference in thermal history between the two material sets used.

**Table 3.1:** Material parameters used in the numerical simulation of macroscopic tests on PC.

$K$ [MPa]	$G$ [MPa]	$G_r$ [MPa]	$\eta_{o,r}$ [MPa s]	$\tau_o$ [MPa]	$\mu$	$S_a$ [-]
3750	321	26	$2.1 \cdot 10^{11}$	0.7	0.08	-

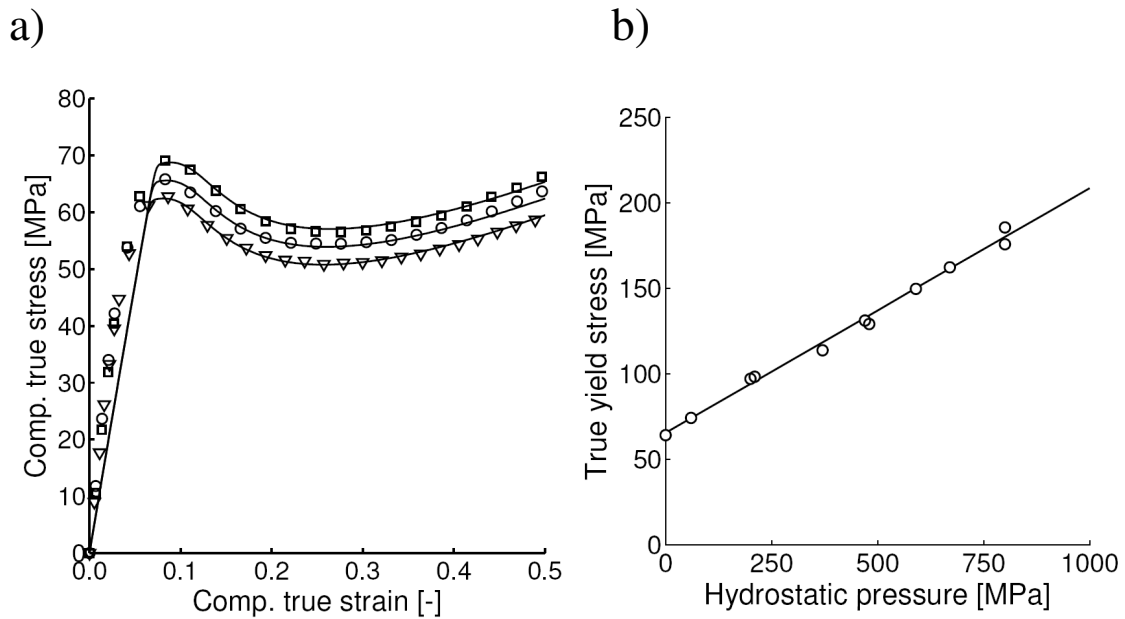


**Figure 3.7:** a) compression tests, experiments (open symbols) compared with the numerical simulation (solid lines) using material parameters presented in Table 3.1 for three different true strain rates:  $10^{-2} \text{ s}^{-1}$  ( $\square$ ),  $10^{-3} \text{ s}^{-1}$  ( $\circ$ ),  $10^{-4} \text{ s}^{-1}$  ( $\nabla$ ); b) yield stress versus superimposed hydrostatic pressure, model prediction (solid line) compared to experimental results (symbols) by Christiansen *et al.* [63] at a strain rate of  $1.7 \cdot 10^{-4} \text{ s}^{-1}$ .

### Macro-scale simulations

Since both rejuvenation and aging kinetics proved to be independent of the molecular weight of the polymer, the only unknown parameter in the model is the initial value of the state parameter,  $S_a$ , which can be directly determined from the yield stress measured in a single simple tensile test at a single strain rate. This is demonstrated in Figure 3.8a, which shows the results of uniaxial tensile tests at a strain rate of  $10^{-3} \text{ s}^{-1}$  for the as-received polymer sheet as well as for a sample annealed for 48 hrs at  $120 \text{ }^\circ\text{C}$ . As a result of this thermal treatment the yield stress of the material has increased substantially [22, 66, 67]. In both cases the samples are observed to neck shortly after the yield stress has been reached, initiated by intrinsic strain softening and qualitatively captured by the model.

For both thermodynamic states the  $S_a$ -value is determined by matching the experimental yield stress with the yield stress of a FEM-simulation using an axisymmetric model of a tensile bar with a small imperfection in the middle (for details see van Melick *et al.* [68]). The simulations, shown in Figure 3.8a, yield  $S_a = 31.7$  for the as-received material and  $S_a = 39$  for the annealed material. With these final values a complete parameter set for both materials is obtained.

To demonstrate the capability of the material to describe the mechanical response in different loading conditions we present in Figure 3.8b the strain rate dependence of the

yield stress of the as-received material in planar extension, shear and uniaxial extension. The solid lines are predictions of the model, using the parameter set presented in Table 3.1 with the  $S_a$ -value of 31.7 that was determined in Figure 3.8a. The predictions are obtained by performing FEM-simulations on the actual sample geometries (see also [39]). It is clear that an accurate, quantitative description is obtained. In the next section we investigate the predictive capabilities of the model in micro-indentation.

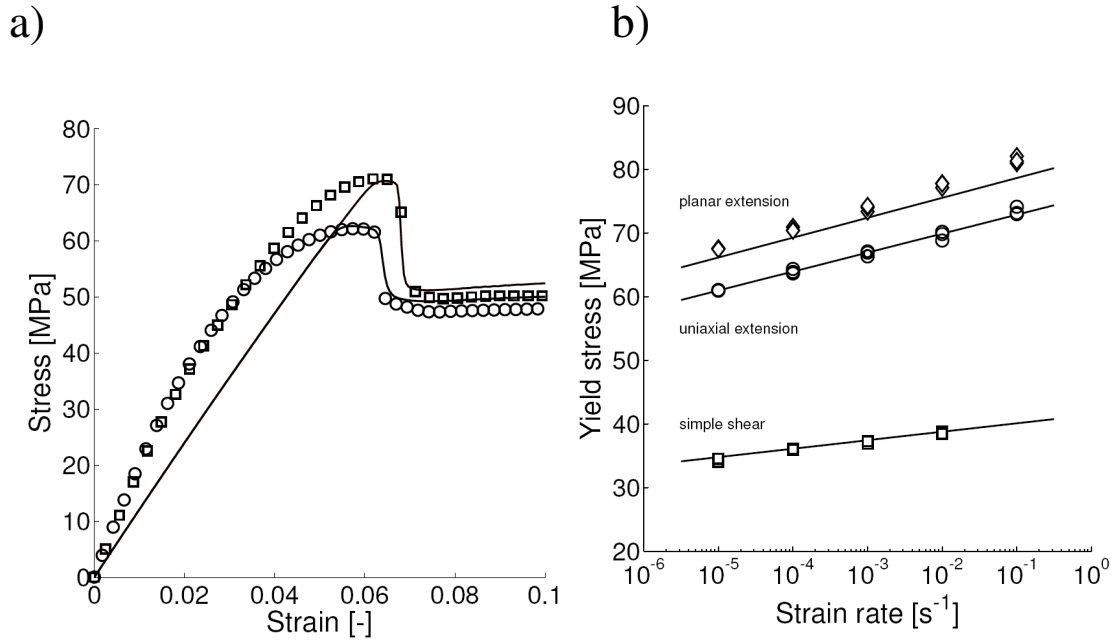


**Figure 3.8:** Experiments (open symbol) compared with the numerical simulation (solid line) on PC a) for tensile tests at a strain rate of  $10^{-3} s^{-1}$  for two different thermal histories with for the as-received  $S_a=31.7$  (○) and for the annealed material  $S_a=39$  (□) and b) predicted yield stress at different strain rates,  $S_a = 31.7$ , for planar extension (□), uniaxial extension (○) and shear (△).

### Micro-scale simulations

Before we apply the model to numerical simulations of the micro-indentation tests, we first have to address an imperfection within the model. In the fitting procedure described above, we employ a shear modulus of 320 MPa which implies an elastic modulus of 900 MPa, considerably smaller than the 2250 MPa observed in uniaxial extension. The reason was the use of the one mode model (only with its linear initial response) and the wish to accurately capture the post yield behavior at the expense in the elastic regime. In the case of indentation, where the elastic deformation also significantly contributes at larger depth, the low value of the modulus leads to a drastic underestimation of the materials resistance. The best method to improve the description of the pre-yield behavior is a multimode extension of the present approach. In a previous study we already demonstrated that the pre-yield response can be accurately captured by a parallel



arrangement of eighteen modes [23]. Unfortunately, this solution tremendously increases the computation time required. Instead, we chose to simply increase the shear modulus  $G$  until the initial slope of the compressive stress-strain curves is properly described. This is achieved with  $G = 784$  MPa. To ensure that the yield and post-yield response remains identical, this change of  $G$  subsequently requires an adaption of the rejuvenated zero viscosity  $\eta_{0,cr}$ . The resulting new data set is given in Table 3.2. The consequences of these changes are demonstrated in Figure 3.9. Figure 3.9a shows the influence of an increase of the shear modulus  $G$  on the compressive stress-strain curve. The initial modulus increases and the strain-at-yield decreases, leading to a shift of the yield and post-yield response to lower strain values. As mentioned before, the value of the yield stress as well as the shape of the post yield behavior remains the same.

**Table 3.2:** Material parameters with increased  $G$ , used in the numerical simulation of indentation tests on PC.

$K$ [MPa]	$G$ [MPa]	$G_r$ [MPa]	$\eta_{0,r}$ [MPa·s]	$\tau_o$ [MPa]	$\mu$	$S_a$ [-]
3750	784	26	$2.8 \cdot 10^{12}$	0.7	0.08	-

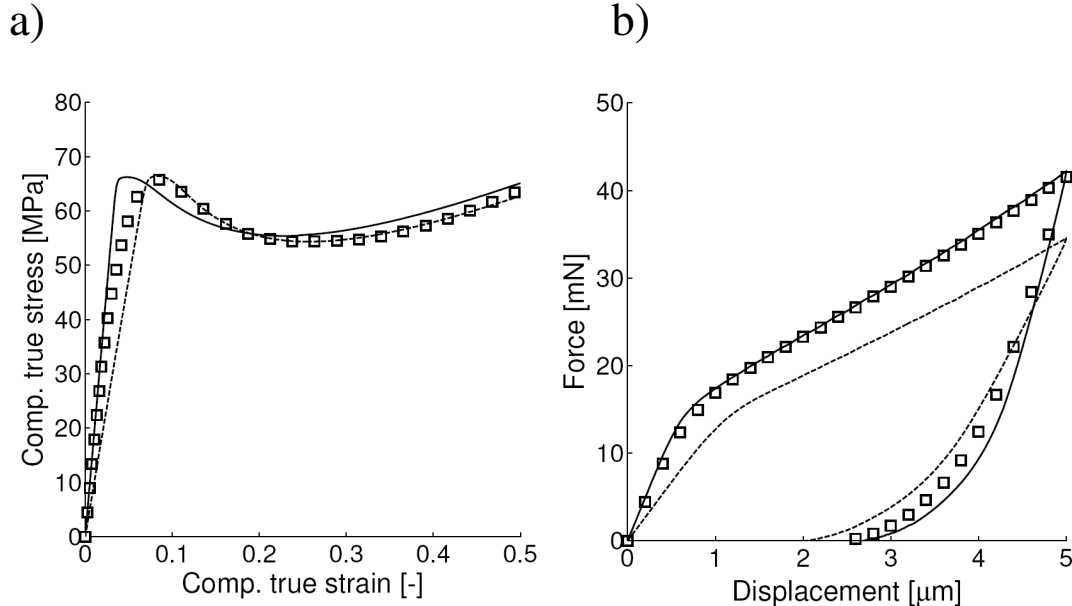


**Figure 3.9:** Effect of the elastic modulus a) simulated compression tests for two different values of the elastic modulus:  $G = 321$  MPa (dashed line) and  $G = 784$  MPa (solid line) compared with the experiments ( $\circ$ ) and; b) for the indentation tests.

The influence on the indentation curves is shown in Figure 3.9b where experimental data on the as-received material are compared to numerical simulations using the  $S_a$ -value of 31.7 determined above (Figure 3.8a). From Figure 3.9b it becomes clear that a correct modulus leads to an accurate, quantitative prediction of the loading path of the indentation test, whereas the low modulus value leads to a large underestimation of the indentation resistance. Figure 3.9b also shows that the current approach is reasonably successful in capturing the unloading path. We expect that this prediction could even be improved if a multimode version of the model would be employed.

In Figure 3.10d a characteristic loading curve of an indentation measurement is shown. Three points are marked: A, B and C. In Figures 3.10a-10c graphical representations of the development of the plastic deformation under the tip are given for these three points. From the numerical evaluations it is derived that the plastic deformation starts at the edge of the indenter, as can be seen in Figure 3.10a, and grows in the form of a hemisphere towards the symmetry axis. This is a result of the fact that stress localizes at the edge of the indenter. Around point B, see Figure 3.10b, the plastic deformation zone concludes the formation of the hemisphere. From point C on, see Figure 3.10c, this hemisphere starts to expand in thickness. These results correspond well to experimental observations made by others [11].

The amount of detail given by our approach is further demonstrated in Figure 3.11, which shows the influence of thermodynamic state (Figure 3.11a) and strain rate (Figure 3.11b) on the response in flat-tip indentation tests. In Figure 3.11a the results are presented of micro-indentation experiments (at a rate of  $50 \text{ nm}\cdot\text{s}^{-1}$ ) on both the as-received and the annealed PC-sheet. It is clear that the numerical simulations, employing the  $S_a$ -values determined in Figure 3.8a, quantitatively predict the load-displacement curves. The agreement is that well that the flat-tip indentation test can be used to determine the  $S_a$ -value of a PC with an unknown thermal history. To achieve this, the load-displacement curve has to be fitted with numerical simulations. For PC the  $S_a$ -value can be determined in this way in practice with accuracy of  $\pm 1$  (corresponding to a yield stress inaccuracy of  $\pm 1 \text{ MPa}$ ).

The feasibility to characterize the  $S_a$ -value from an indentation test is demonstrated in Figure 3.11b, which presents micro-indentation results at different indentation rates ( $5 \text{ nm}\cdot\text{s}^{-1}$ ,  $50 \text{ nm}\cdot\text{s}^{-1}$ , and  $200 \text{ nm}\cdot\text{s}^{-1}$ ). The material indented is a PC which was annealed for a few hours at  $120 \text{ }^\circ\text{C}$ . An  $S_a$ -value of 34 is determined by fitting the numerical prediction to the load-displacement curve of  $5 \text{ nm}\cdot\text{s}^{-1}$ . The loading curves of the other indentation rates are subsequently simulated with this value. The result is clear; the influence of strain rate is also quantitatively predicted by our model.

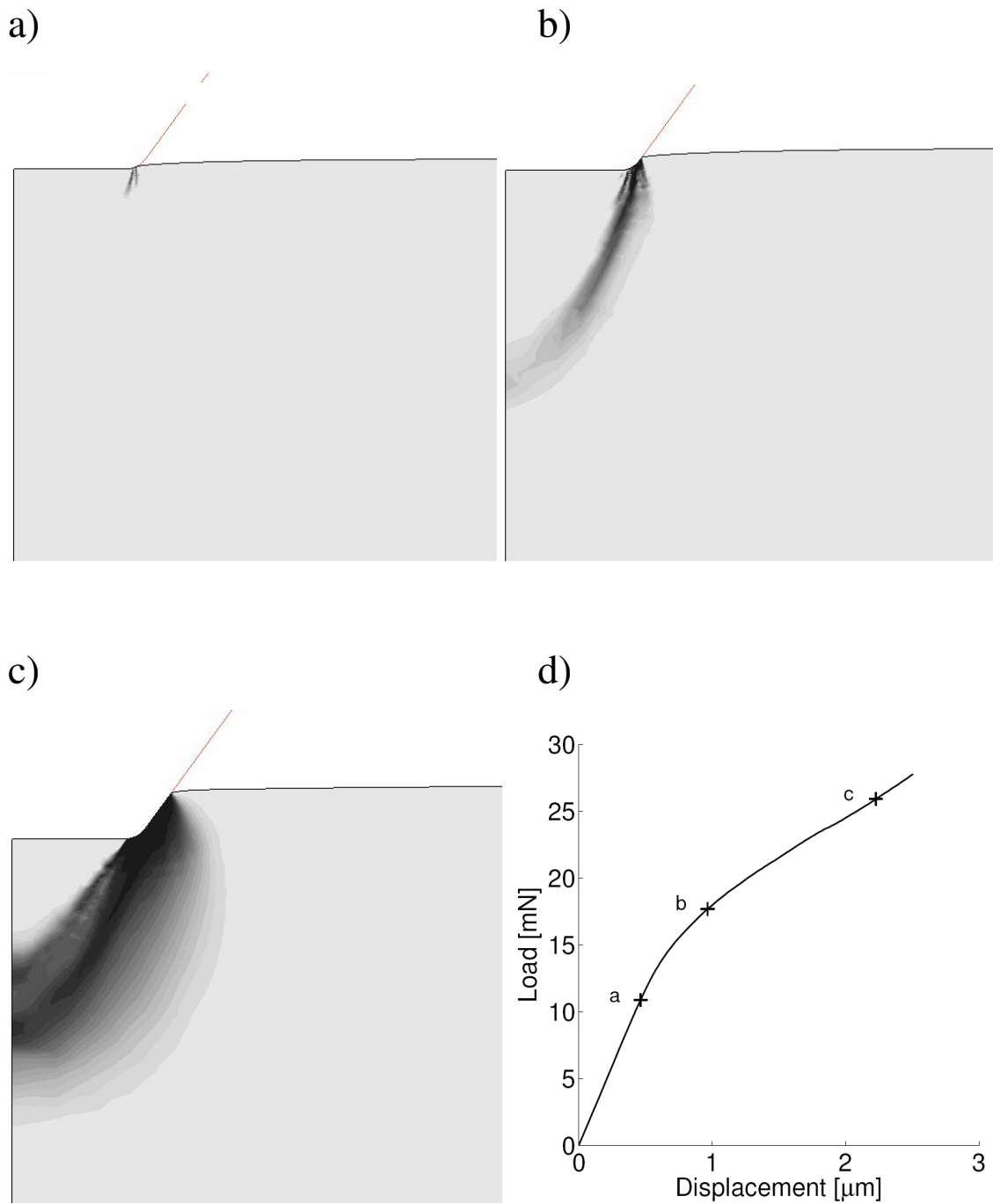


**Figure 3.10:** Simulation of the development of the plastic deformation at different indentation depth for PC: a) at 460nm; b) 965 nm; c) 2.2 μm; d) the load displacement curve where points a b c indicate at which deformation the simulated plastic deformation are captured.

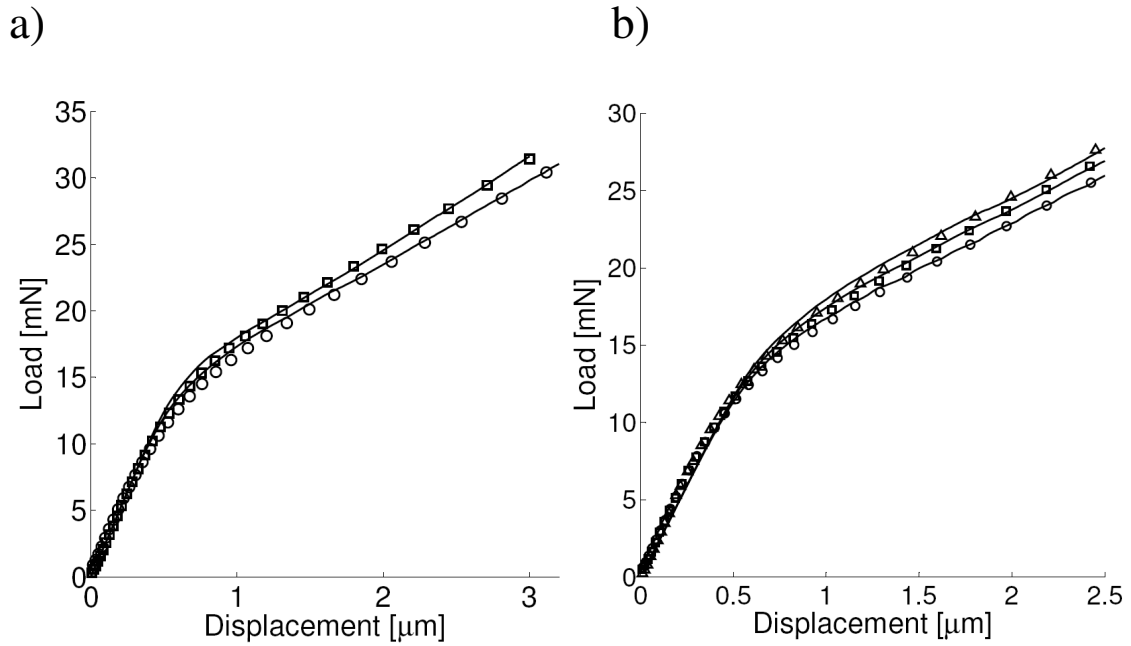


**Figure 3.11:** Flat punch indentation experiments (open symbols) compared with the numerical prediction (solid line): a) as-received ( $S_a = 31.7$ ) ( $\circ$ ) and for annealed ( $S_a = 39$ ) ( $\square$ ) PC at an indentation speed of  $50 \text{ nm}\cdot\text{s}^{-1}$  and b) for speeds of  $5 \text{ nm}\cdot\text{s}^{-1}$  ( $\circ$ ),  $50 \text{ nm}\cdot\text{s}^{-1}$  ( $\square$ ) and  $200 \text{ nm}\cdot\text{s}^{-1}$  ( $\triangle$ ) on the as-received PC ( $S_a=34$ ).

### 3.4.2. Thermorheologically complex behavior: PMMA

#### *Material characterization*

In the case of PMMA, there are two molecular processes that contribute to the yield stress which implies that the viscosity function defined in Equation 3.17 must be applied. This means that, besides the parameters already discussed in the previous section ( $\eta_{0,\alpha}$ ,  $\tau_{0,\alpha}$ ,  $\mu$ ,  $r_0$ ,  $r_1$ ,  $r_2$ ,  $G_r$ ,  $G$ , and  $K$ ), we also have to determine the values of  $\eta_{0,\alpha+\beta}$  and  $\tau_{0,\alpha+\beta}$ . For the characterization we make use of the fact that the  $\beta$ -contribution is only present at high strain rates and, therefore, the stress-strain response in the low strain rate range will be determined by the  $\alpha$ -process only. As a consequence, we can use the same characterization strategy at low strain rates as employed in the previous section for PC. For the elastic properties of PMMA we used a bulk modulus  $K$  of 3 GPa [69], the appropriate value of the shear modulus  $G$  is determined to be 760 MPa from the initial slope of the compressive stress-strain curves. To facilitate the fitting procedure we initially adopt a lower value for  $G$  (630 MPa). After characterization of the  $\alpha$ -parameters, the values for  $\eta_{0,\alpha+\beta}$  and  $\tau_{0,\alpha+\beta}$  were subsequently determined by fitting numerical predictions to the compressive stress-strain curves obtained at higher strain rates ( $\alpha+\beta$  region).

To obtain the true value of the pressure-dependence parameter  $\mu_\alpha$  we use a method inspired by the work of Bardia and Narasimhan [70], who employed an spherical indentation test to characterize the pressure sensitivity index of the Drucker–Prager constitutive model. Here we follow a similar route. Since the compression tests and the indentation tests are performed on the same sample, the  $S_a$  value is identical in both cases. In the  $\alpha$ -range, the only unknown parameter is therefore the pressure dependence  $\mu_\alpha$ . We again generate different parameter sets by fitting the compression data for different values of  $\mu_\alpha$ . Note that each set describes the compressive stress-strain curves equally well (Figure 3.12a). With these data sets we subsequently predict the load-deformation curve for an indentation rate of  $5 \text{ nm}\cdot\text{s}^{-1}$  (see Figure 3.12b) and found that a value of  $\mu_\alpha = 0.13$  is in good agreement with the experiments. The complete data sets, used for the predictions in Figures 3.12, are tabulated in Table 3.3 (compression) and Table 3.4 (indentation). The corresponding  $S_a$ -value is determined to be 7.8.

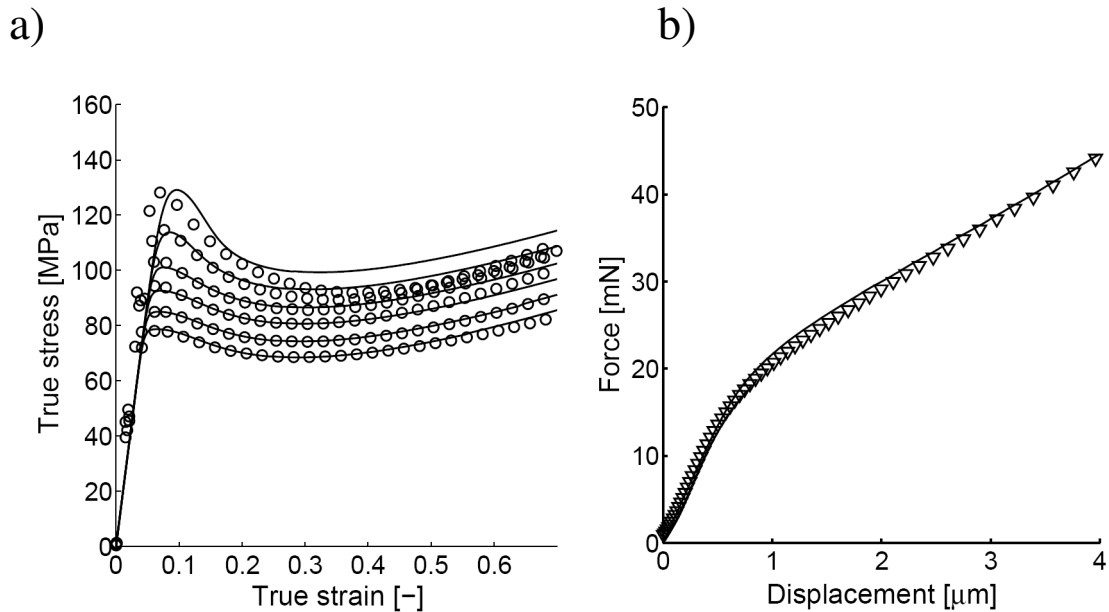


**Figure 3.12:** Experiments (open symbols) compared to numerical simulation (solid lines) for: a) compression tests ( $\circ$ ) performed on PMMA at a strain rate of  $10^{-4} \text{ s}^{-1}$ ,  $3\cdot 10^{-4} \text{ s}^{-1}$ ,  $10^{-3} \text{ s}^{-1}$ ,  $3\cdot 10^{-3} \text{ s}^{-1}$ ,  $10^{-2} \text{ s}^{-1}$ ,  $3\cdot 10^{-2} \text{ s}^{-1}$  and; b) flat indentation performed at  $5 \text{ nm}\cdot\text{s}^{-1}$  ( $\nabla$ ).

**Table 3.3:** Parameters used in the numerical simulation of compression tests on PMMA.

$K$ [MPa]	$G$ [MPa]	$G_r$ [MPa]	$\tau_{0,\alpha}$ [MPa]	$\tau_{0,\alpha+\beta}$ [MPa]	$\eta_{0,\alpha}$ [MPa·s]	$\eta_{0,\alpha+\beta}$ [MPa·s]
3000	628	26	2.71	7.05	$8.13 \cdot 10^6$	$2.12 \cdot 10^5$

$\mu$	$S_a$	$r_o$	$r_1$	$r_2$
0.13	7.8	0.96	30	-3.5

Finally, indentation tests are performed at indentation rates of  $5 \text{ nm}\cdot\text{s}^{-1}$ ,  $10 \text{ nm}\cdot\text{s}^{-1}$ ,  $20 \text{ nm}\cdot\text{s}^{-1}$  and  $40 \text{ nm}\cdot\text{s}^{-1}$ . The results are compared to numerical predictions (employing the parameters listed in Table 3.4) in Figure 3.13a. It is clear that the numerical predictions are in excellent agreement with the pronounced rate-dependence observed in the experimental force-displacement curves. To demonstrate the presence of a  $\beta$ -contribution in the indentation response, we perform simulations of indentation test at rates of  $0.1 \text{ nm}\cdot\text{s}^{-1}$  and  $40 \text{ nm}\cdot\text{s}^{-1}$  with, as well as without, a  $\beta$ -contribution (without implies  $\eta_{0,\alpha+\beta}=0$ ). The results are presented in Figure 3.13b and show that at a low indentation rate ( $0.1 \text{ nm}\cdot\text{s}^{-1}$ ) the  $\beta$ -contribution is negligible, whereas at higher rates a significant contribution is visible.

**Table 3.4:** Parameter set with corrected  $G$ , used in the numerical simulation of indentation tests on PMMA.

$K$ [MPa]	$G$ [MPa]	$G_r$ [MPa]	$\tau_{0,\alpha}$ [MPa]	$\tau_{0,\alpha+\beta}$ [MPa]	$\eta_{0,\alpha}$ [MPa·s]	$\eta_{0,\alpha+\beta}$ [MPa·s]
3000	759	26	2.71	7.05	$9.27 \cdot 10^6$	$2.22 \cdot 10^5$

$\mu$	$S_a$	$r_o$	$r_1$	$r_2$
0.13	7.8	0.96	30	-3.5

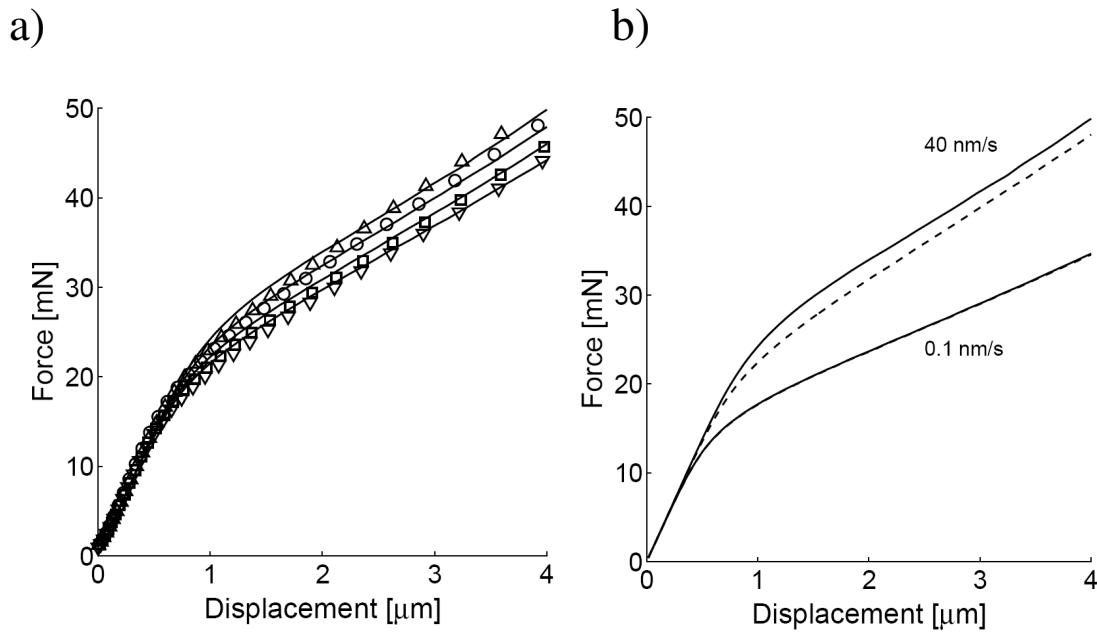


**Figure 3.13:** a) flat punch indentation performed on PMMA at a speed of  $5 \text{ nm}\cdot\text{s}^{-1}$  ( $\nabla$ ),  $10 \text{ nm}\cdot\text{s}^{-1}$  ( $\square$ ),  $20 \text{ nm}\cdot\text{s}^{-1}$  ( $\circ$ ),  $40 \text{ nm}\cdot\text{s}^{-1}$  ( $\triangle$ ) compared with the numerical simulations (solid lines) and b) numerical simulation performed using a model which takes into account the  $\alpha$  contribution (dashed lines) only and the  $\alpha + \beta$  contribution (solid lines) at two different speeds  $0.1 \text{ nm}\cdot\text{s}^{-1}$  and  $40 \text{ nm}\cdot\text{s}^{-1}$ .

### 3.5. Conclusions

In the plastic regime, glassy polymers possess a rather complex intrinsic behavior, with a pronounced pressure- and rate-dependence of the yield stress as well as a post yield region displaying both strain softening and strain hardening. We employ a state-of-the-art constitutive model, previously developed in our group, which describes this intrinsic behavior, to numerically predict the indentation response. In the model, a single parameter, the state parameter  $S_a$ , is used to uniquely determine the initial yield stress of the material, and to capture all variations in its thermal history. We demonstrate that this model can capture the rate-, and history-dependence of PC and PMMA on both the macroscopic and microscopic scale. The excellent accuracy of the description also creates the possibility to accurately extract the state parameter  $S_a$  directly from micro-indentation experiments. This offers interesting possibilities with respect to quality control of load-bearing polymer products. Moreover, it was found that the pressure dependence of the yield stress can also be obtained by combining indentation tests and compression tests on the same samples.

## References

- [1] M.R. VanLandingham, J.S. Villarrubia, W.F. Guthrie, and G.F. Meyers, *Nanoindentation of polymers: an overview*. Macromolecular Symposia, 2001. **167**: p. 15-44.
- [2] W.C. Oliver and G.M. Pharr, *Measurement of hardness and elastic modulus by instrumented indentation: Advances in understanding and refinements to methodology*. J. Mat. Res., 2004. **19**(1): p. 3-20.
- [3] H. Hertz, *Uber die Berhrung Fester Elastischer Korper (On the contact of elastic solids)*. J. Reine Angew. Math., 1881. **92**: p. 156-171.
- [4] W.C. Oliver and G.M. Pharr, *An improved technique for determining hardness and elastic-modulus using load and displacement sensing indentation experiments*. J Mater. Res., 1992. **7**(6): p. 1564 - 1583.
- [5] L. Cheng, X. Xia, L.E. Scriven, and W.W. Gerberich, *Spherical-tip indentation of viscoelastic material*. Mech. of Mat., 2005. **37**: p. 213-226.
- [6] L. Cheng, X. Xia, W. Yu, L.E. Scriven, and W.W. Gerberich, *Flat punch indentation of viscoelastic material*. Journal of Polymer Science B: polymer physics, 2000. **38**(1): p. 10-22.
- [7] J.M.J. den Toonder, Y. Ramone, A.R. van Dijken, J.G.J. Beijer, and G.Q. Zhang, *Viscoelastic characterization of Low-Dielectric-Constant SiLK films using nano-indentation*. Proceedings of the 3rd International Conference on Benefiting from Thermal and Mechanical Simulation in (Micro)-Electronics, 2002: p. 270-280.
- [8] J.M.J. den Toonder, Y. Ramone, A.R. van Dijken, J.G.J. Beijer, and G.Q. Zhang, *Viscoelastic characterization of low-dielectric-constant SiLK films using nano-indentation in combination with finite element modeling*. Journal of Electronic Packaging, 2005. **127**: p. 267-285.
- [9] P.L. Larsson and S. Carlsson, *On microindentation of viscoelastic polymers*. Polymer Testing, 1998. **17**: p. 49-75.
- [10] K.L. Johnson, *The correlation of indentation experiments*. J.Mech. and Phys. Solid, 1970. **18**: p. 115-128.
- [11] Y. Lu and D.M. Shinozaki, *Microindentation induced debonding of polymer thin films from rigid substrates*. J. Mater. Sci., 2002. **37**: p. 1283-1293.
- [12] D. Tabor, *Hardness of metals*. 1951, Oxford: Clarendon press.
- [13] A.E. Giannakopoulos, P.L. Larsson, and R. Vestergaard, *Analysis of Vickers indentation*. Int. J. Solids Structures, 1994. **31**(19): p. 2679-2708.



- 
- [14] P.L. Larsson, A.E. Giannakopoulos, E. Söderlund, D.J. Rowcliffe, and R. Vestergaard, *Analysis of Berkovich indentation*. Int. J. Solids Structures, 1996. **33**(2): p. 221-248.
- [15] E.M. Arruda and M.C. Boyce, *Evolution of plastic anisotropy in amorphous polymers during finite straining*. Int. J. Plast., 1993. **9**: p. 697-720.
- [16] M.C. Boyce, D.M. Parks, and A.S. Argon, *Large inelastic deformation of glassy polymers. Part 1: Rate dependent constitutive model*. Mech. of Mat., 1988. **7**: p. 15-33.
- [17] O.A. Hasan, M.C. Boyce, X.S. Li, and S. Berko, *An investigation of the yield and post-yield behavior and corresponding structure of poly(methylmethacrylate)*. J. Polym. Sci., Part B, Polym. Phys., 1993. **31**(2): p. 185-197.
- [18] C.P. Buckley, P.J. Dooling, J. Harding, and C. Ruiz, *Deformation of thermosetting resins at impact rates of strain. Part 2: constitutive model with rejuvenation*. J. Mech. and Phys. Solid, 2004. **52**(10): p. 2355-2377.
- [19] C.P. Buckley and D.C. Jones, *Glass-rubber constitutive model for amorphous polymers near the glass transition*. Polymer, 1995. **36**: p. 3301-3312.
- [20] J.J. Wu and C.P. Buckley, *Plastic deformation of glassy polystyrene: A unified model of yield and the role of chain length*. J. Polym. Sci. Part B. Polym. Phys., 2004. **42**(11): p. 2027-2040.
- [21] L.E. Govaert, P.H.M. Timmermans, and W.A.M. Brekelmans, *The influence of intrinsic strain softening on strain localization in polycarbonate: modeling and experimental validation*. J. Eng. Mat. and Tech., 2000. **122**: p. 177-185.
- [22] E.T.J. Klompen, T.A.P. Engels, L.E. Govaert, and H.E.H. Meijer, *Modelling of the post-yield response of glassy polymers: influence of thermomechanical history*. Macromol., 2005. **38**: p. 6997-7008.
- [23] T.A. Tervoort, E.T.J. Klompen, and L.E. Govaert, *A multi-mode approach to finite, three-dimensional, nonlinear viscoelastic behaviour of glassy polymer*. J. Rheol., 1996. **40**: p. 779-797.
- [24] M.C. Boyce and E.M. Arruda, *An experimental and analytical investigation of the large strain compressive and tensile response of glassy polymers*. Polym. Eng. Sci., 1990. **30**(20): p. 1288-1298.
- [25] M.C. Boyce, E.M. Arruda, and R. Jayachandran, *The large strain compression, tension, and simple shear of polycarbonate*. Polym. Eng. Sci., 1994. **34**(9): p. 716-725.
- [26] P.D. Wu and E. van der Giessen, *On neck propagation in amorphous glassy polymers under plane strain tension*. Int. J. Plast., 1995. **11**: p. 211-235.
- [27] H.E.H. Meijer and L.E. Govaert, *Multi-Scale Analysis of Mechanical Properties of Amorphous Polymer Systems*. Macromol. Chem. Phys., 2003. **204**: p. 274-288.

- 
- [28] H.G.H. Van Melick, O.F.J.T. Bressers, J.M.J. den Toonder, L.E. Govaert, and H.E.H. Meijer, *A micro-indentation method for probing the craze-initiation stress in glassy polymers*. *Polymer*, 2003. **44**: p. 2481-2491.
- [29] H.G.H. van Melick, L.E. Govaert, and H.E.H. Meijer, *Prediction of brittle-to-ductile transitions in polystyrene*. *Polymer*, 2003. **44**: p. 457-465.
- [30] S. Swaddiwudhipong, L.H. Poh, J. Hua, Z.S. Liu, and K.K. Tho, *Modeling nano-indentation tests of glassy polymers using finite elements with strain gradient plasticity*. *Mater. Sci. Eng. A*, 2005. **404**: p. 179-187.
- [31] L. Anand and N.M. Ames, *On modeling the micro-indentation response of an amorphous polymer*. *Int. J. of Plasticity*, 2006. **22**: p. 1123-1170.
- [32] Y. Lu and D.M. Shinozaki, *Deep penetration micro-indentation testing of high density polyethylene*. *Mat. Sci. and Eng. A*, 1998. **249**: p. 134-144.
- [33] S.C. Wright, Y. Huang, and N.A. Fleck, *Deep penetration of polycarbonate by a cylindrical punch*. *Mech. of Mat.*, 1992. **13**: p. 277-284.
- [34] H.G.H. van Melick, L.E. Govaert, and H.E.H. Meijer, *On the origin of Strain hardening in glassy polymers*. *Polymer*, 2003. **44**: p. 2493-2502.
- [35] C. G'Sell, J.M. Hiver, A. Dahoun, and A. Souahi, *Video-controlled tensile testing of polymers and metals beyond the necking point*. *J. Mater. Sci.*, 1992. **27**(18): p. 5031-5039.
- [36] R.N. Haward and G. Thackray, *Use of a mathematical model to describe isothermal stress-strain curves in glassy thermoplastics*. *Proc. Royal Soc. London A.*, 1967. **302**: p. 453-472.
- [37] T.A. Tervoort and L.E. Govaert, *Strain hardening behavior of polycarbonate in the glassy state*. *J. Rheol.*, 2000. **44**(6): p. 1263 - 1277.
- [38] J.M. Hutchinson, *Physical aging of polymers*. *Prog. Polym. Sci.*, 1995. **20**: p. 703-760.
- [39] E.T.J. Klompen, T.A.P. Engels, L.C.A. van Breemen, P.J.G. Schreurs, L.E. Govaert, and H.E.H. Meijer, *Quantitative Prediction of Long-Term Failure of Polycarbonate*. *Macromol.*, 2005. **38**: p. 7009-7017.
- [40] E.T.J. Klompen, PhD thesis, *Mechanical properties of solid polymers*, 2005, [www.mate.tue.nl/mate/pdfs/4944.pdf](http://www.mate.tue.nl/mate/pdfs/4944.pdf)
- [41] E.M. Arruda, M.C. Boyce, and R. Jayachandran, *Effects of strain rate, temperature and thermomechanical coupling on the finite strain deformation of glassy polymers*. *Mech. of Mat.*, 1995. **19**: p. 193-212.
- [42] C. Bauwens-Crowet, J.C. Bauwens, and G. Homes, *Tensile Yield-Stress Behavior of Glassy Polymers*. *J. Polym. Sci.*, 1969. **7**: p. 735-742.

- [43] E.T.J. Klompen and L.E. Govaert, *Nonlinear viscoelastic behaviour of thermorheologically complex materials: a modeling approach*. Mech. Time-depend. Mater., 1999. **3**: p. 49-69.
- [44] J.A. Roetling, *Yield stress behavior of poly(ethyl methacrylate) in the glass transition region*. Polymer, 1965. **6**(11): p. 615-619.
- [45] J.A. Roetling, *Yield stress of polymethylmethacrylate*. Polymer, 1966. **6**(6): p. 311-317.
- [46] T. Ree and H. Eyring, *Theory of non-Newtonian flow I. Solid plastic system*. J. Appl. Phys., 1955. **26**: p. 793-800.
- [47] T.A. Tervoort, R.J.M. Smit, W.A.M. Brekelmans, and L.E. Govaert, *A constitutive equation for the elasto-viscoplastic deformation of glassy polymers*. Mech. Time-Dep. Mater., 1998. **1**(3): p. 269-291.
- [48] F.P.T. Baaijens, *Calculation of residual stresses in injection molded products*. Rheol. Acta, 1991. **30**: p. 284-299.
- [49] R.A. Duckett, B.C. Goswami, L.S.A. Smith, I.M. Ward, and A.M. Zihlif, *The yielding and crazing behaviour of polycarbonate in torsion under superposed hydrostatic pressure*. Brit. Polym. J., 1978. **10**: p. 11-16.
- [50] L.E. Govaert, H.J. Schellens, H.J.M. Thomassen, R.J.M. Smit, L. Terzoli, and T. Peijs, *A micromechanical approach to time-dependent failure in off-axis loaded polymer composites*. Composites:Part A, 2001. **32**: p. 1697-1711.
- [51] Defined by  $\dot{\gamma}_p = \sqrt{\text{tr}(\mathbf{D}_p \cdot \mathbf{D}_p)}$
- [52] Defined by  $\bar{\tau} = \sqrt{\frac{1}{2} \text{tr}(\boldsymbol{\sigma}_s^d \boldsymbol{\sigma}_s^d)}$
- [53] Defined by  $\dot{\gamma}_p = \sqrt{\text{tr}(\mathbf{D}_p \cdot \mathbf{D}_p)}$
- [54] T.A.P. Engels, L.E. Govaert, G.W.M. Peters, and H.E.H. Meijer, *Processing induced properties in glassy polymers: application of structural relaxation to yield stress development*. J. Polym. Sci., Part B :Polym. Phys., 2006. **44**(8): p. 1212-1225.
- [55] L.E. Govaert, T.A.P. Engels, E.T.J. Klompen, G.W.M. Peters, and H.E.H. Meijer, *Processing-induced properties in glassy polymers: development of the yield stress in polycarbonate*. International Polymer Processing XX, 2005. **2**: p. 170-177.
- [56] C. Bauwens-Crowet, J.C. Bauwens, and G. Homes, *The temperature dependence of yield stress of polycarbonate in uniaxial compression and tensile tests*. J. Mater. Sci., 1972. **7**: p. 176-183.
- [57] C. Bauwens-Crowet, *The compression yield behaviour of polymethyl methacrylate over a wide range of temperatures and strain-rates*. J. Mater. Sci., 1973. **8**: p. 968-979.

- [58] L.E. Govaert, P.J. de Vries, P.J. Fennis, W.F. Nijenhuis, and J.P. Keustersmans, *Influence of strain rate, temperature and humidity on the tensile yield behaviour of aliphatic polyketone*. *Polymer*, 2000. **41**(5): p. 1959-1962.
- [59] J.A. Roetling, *Yield-stress behavior of isotactic polypropylene*. *Polymer*, 1966. **7**(7): p. 303-306.
- [60] C. Bauwens-Crowet and J.C. Bauwens, *Effect of thermal history on the tensile yield stress of polycarbonate in the beta-transition range*. *Polymer*, 1983. **24**: p. 921-924.
- [61] W. Whitney and R.D. Andrews, *Yielding of glassy polymers. Volume effects*. *J. Polym. Sci., Polym. Symp.*, 1967. **16**(5): p. 2981-2990.
- [62] C.G.N. Pelletier, E.C.A. Dekkers, L.E. Govaert, J.M.J. Den Toonder, and H.E.H. Meijer, *The influence of indenter-surface misalignment on the results of instrumented indentation tests*. *Polym. Test.*, 2007. **26**(7): p. 949-959.
- [63] A.W. Christiansen, E. Baer, and S.V. Radcliffe, *The mechanical behaviour of glassy polymers under high pressure*. *Phil. Mag.*, 1971. **24**: p. 451-467.
- [64] J.A. Sauer, D.R. Mears, and K.D. Pae, *Eur. Polym. J.*, 1970. **6**: p. 1015-1032.
- [65] W.A. Spitzig and O. Richmond, *Effect of the hydrostatic pressure on the deformation behavior of polyethylene and polycarbonate in tension and compression*. *Polym. Eng. Sci.*, 1979. **19**: p. 1129-1139.
- [66] C. Bauwens-Crowet and J.C. Bauwens, *Annealing of polycarbonate below the glass transition: quantitative interpretation of the effect on yield stress and differential scanning calorimetry measurements*. *Polymer*, 1982. **23**: p. 1599-1604.
- [67] J.H. Golden, B.L. Hammant, and E.A. Hazell, *The effect of thermal pre-treatment on the strength of polycarbonate*. *J. Appl. Polym. Sci.*, 1967. **11**: p. 1571-1579.
- [68] H.G.H. Van Melick, L.E. Govaert, and H.E.H. Meijer, *Localization phenomena in glassy polymers: influence of thermal and mechanical history*. *Polymer*, 2003. **44**: p. 3579-3591.
- [69] I.W. Gilmour, A. Trainor, and R.N. Haward, *Elastic moduli of glassy polymers at low strains*. *J. Appl. Polym. Sci.*, 1979. **23**: p. 3129-3138.
- [70] P. Bardia and R. Narasimhan, *Characterization of pressure-sensitive yielding in polymers*. *Strain*, 2006. **42**: p. 187-196.



## Chapter 4

# Quantitative assessment and prediction of the contact area development during spherical tip indentation of glassy polymers\*

---

### Abstract

In this chapter we study the development of the contact area during indentation of polycarbonate. The contact area was measured *in situ* using an instrumented indentation microscope and compared with numerical simulations using an elasto-plastic constitutive model. The parameters in the model were obtained using macroscopic tests. Indentations were performed on samples with different thermal histories and at different speeds. For all cases, the numerical model correctly predicted the development of the contact area during indentation. For increasing strain rates, the contact area decreases at equal indentation depths. Annealing the samples results in a smaller contact area at equal indentation depth. Using only numerical simulations, it was also shown that pile-up around the indenter results from localization effects and is thus promoted by strain softening properties of the indented material. Strain hardening, on the other hand, tends to promote sink-in.

Finally, we performed simulations of load-relaxation during indentation. The results indicate that about 40% of the total observed relaxation may be assigned to plastic effects.

\* This chapter is reproduced from: C.G.N Pelletier, J.M.J. den Toonder, L.E. Govaert, N. Hakiri, M. Sakai, **Quantitative assessment and prediction of the contact area development during spherical tip indentation of glassy polymers**, submitted to Philosophical Magazine.

## 4.1. Introduction

Nowadays, indentation is a fairly mature technique to probe mechanical properties of small volumes of materials and especially thin films. The main requirement for an indentation sample is that the indented surface should be sufficiently smooth to obtain reproducible results, but no further special sample preparation is needed. During indentation, the applied load and the tip displacement are continuously recorded. From such data mechanical properties, like the elastic modulus or the yield stress of the materials, can be extracted using various methods depending on the deformation regime and tip's geometry. In all indentation analysis models, the accuracy of the estimated mechanical properties is strongly related to the accurate determination of the contact area between the indenter tip and the material surface, which is not always straightforward. The main difficulty is, that for most materials the contact area cannot be estimated directly from the measured tip indenter displacement. Figure 4.1 illustrates the fact that the measured displacement of the tip ( $h$ ) is in practice hardly ever equal to the contact depth ( $h_c$ ).  $h_c$  is the depth over which the tip and the surface make contact, and knowing the tip's geometrical shape this determines the (projected) contact area. At the vicinity of the tip, the surface can sink-in (on the right in Figure 4.1) or pile-up (on the left in Figure 4.1).

For the special case of frictionless contact of a spherical indenter with a flat linearly elastic half space, the surface will sink-in in such a way that the contact depth ( $h_c$ ) is equal to half of the tip displacement  $h$ . For small displacements with respect to the tip size (radius), the projected contact area for spherical indentation is given by [1]:

$$A_p = \pi a^2 \approx \pi R h \quad (4.1)$$

where  $A_p$  is the projected area,  $a$  is the contact radius,  $R$  is the tip radius and  $h$  is the tip displacement defined by:

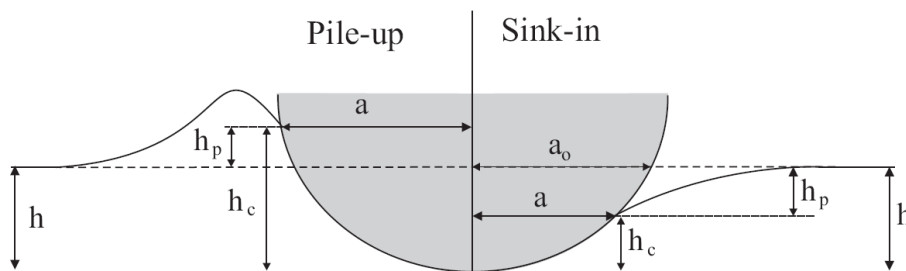


**Figure 4.1:** Contact profile developed during indentation where  $h$  is the indentation depth,  $h_c$  is the contact depth,  $a$  is the contact radius.

$$h = h_p + h_c \quad (4.2)$$

where  $h_c$  is the contact depth and  $h_p$  the difference between the displacement and the contact depth (see Figure 4.1).

In the general case, the projected contact area is defined as a function of the contact depth by a simple geometric relation:

$$A_p = \pi a^2 = \pi (2R - h_c)h_c \quad (4.3)$$

where  $h_c$  is the contact depth. Unfortunately, when in addition to elastic deformation, also plastic deformation occurs, no analytical solution exists that describes the relationship between the actual contact depth and the experimentally measured tip displacement. Therefore the contact area cannot be determined directly from the load-displacement curves, which makes it impossible to determine the mechanical properties without assumptions or approximations about the contact area.

Popular methods to determine mechanical properties from indentation were proposed by Oliver and Pharr for a Berkovich tip [2] and by Field and Swain for a spherical tip [3]. Essentially, the method is based on elastic contact theory of symmetric indenters. Plastic deformation, occurring in addition to purely elastic strains, is assumed to result only in a shift of the total indentation depth and not in a change of the nature of the surface deformation near the contact. The final analysis, therefore, is a purely elastic analysis of the (elastic) unloading part of the indentation curve. In principle, the method is thus not applicable to materials exhibiting pile-up or extensive sink-in. In daily practice, calibration procedures involving the fitting of a polynomial function, that describes the relationship between the projected contact area and the indentation depth, indirectly compensate for this flow in the method. However this compensation is only valid for the material used for the calibration, which is usually fused silica.

Pile-up, which may occur in many metals and in polymers, can lead to significant errors in the determination of the contact area. Using finite element simulations, it was shown that the Oliver and Pharr method may significantly underestimate the contact area when the material piles-up [4]. The amount of pile-up depends on the ratio of the elastic modulus to the yield stress and on work hardening properties. For a large ratio and no or little work hardening, the material will exhibit a pronounced pile-up. In contrast, an increase in work hardening will tend to inhibit the pile-up. Compared to Berkovich indentation, the situation is more complex for spherical indentation as the amount of pile-up is a function of the indentation depth [5]. It should be mentioned, that the numerical model used in reference [5] to study pile-up is based on an elasto-plastic constitutive model with strain hardening, which is appropriate for a class of metals.

Compared to metals, glassy polymers possess a more complex intrinsic behavior, namely a more pronounced strain rate dependence of the yield stress and a post yield



region displaying strain softening as well as strain hardening. These intrinsic properties result in an evolution of the contact area during indentation that cannot be described with common metal models since these do not capture these specific intrinsic features.

In the last 20 years, considerable effort has been made to model the post yield behavior of glassy polymers and a number of 3D numerical models were developed and validated, by Boyce *et al.* at MIT [6-8], Paul Buckley *et al.* in Oxford [9-11] and our own group in Eindhoven [12-14]. Common factors of these models are the application of a stress dependent viscosity to capture the deformation kinetics and the use of rubber elasticity to model strain hardening.

We will use our numerical model to investigate the evolution of the contact area during spherical indentation on polycarbonate. The simulations will be validated using a recently developed technique, the instrumented indentation microscope [15, 16], which enables the direct measurement of the contact area during indentation.

## 4.2. Mechanical properties of glassy polymers: phenomenology

Intrinsic behavior is defined as the response of the material under homogenous deformation. In general the intrinsic behavior of amorphous polymers, like polycarbonate, polystyrene, or polymethylmethacrylate, exhibits a non-linear viscoelastic regime at low deformation followed by yielding and complex post yield behavior. After yielding, the true stress drops with increasing the plastic strain (strain softening) and finally increases again at larger deformation (strain hardening).

This response is dependent on temperature, pressure and thermodynamic state. An illustration of the influence of deformation rate on polycarbonate (PC) is shown in Figure 4.2a. With an increasing strain rate the yield stress increases leading to a shift of the total plastic response to higher stress. Contrary to the yield stress, the strain softening is rate independent. Figure 4.2b shows the influence of the material's thermal history on the plastic response. By annealing the sample, the yield stress and the strain softening increase. It should be noticed that the response at large deformations is independent of the thermal history. At large deformations, namely, the effect (of the thermal-history) has been erased by the plastic deformation, i.e. the material returns to the rejuvenated state. In such a state, the intrinsic response of amorphous polymers exhibits no strain softening as is illustrated in Figure 4.2b.

## 4.3. Modeling

### 4.3.1. Constitutive modeling

In previous work we developed an 3D elasto-viscoplastic constitutive equation that accurately captures the deformation characteristics of polymer glasses [12, 13, 17, 18]. The basis of this constitutive model is the division of the total stress into two

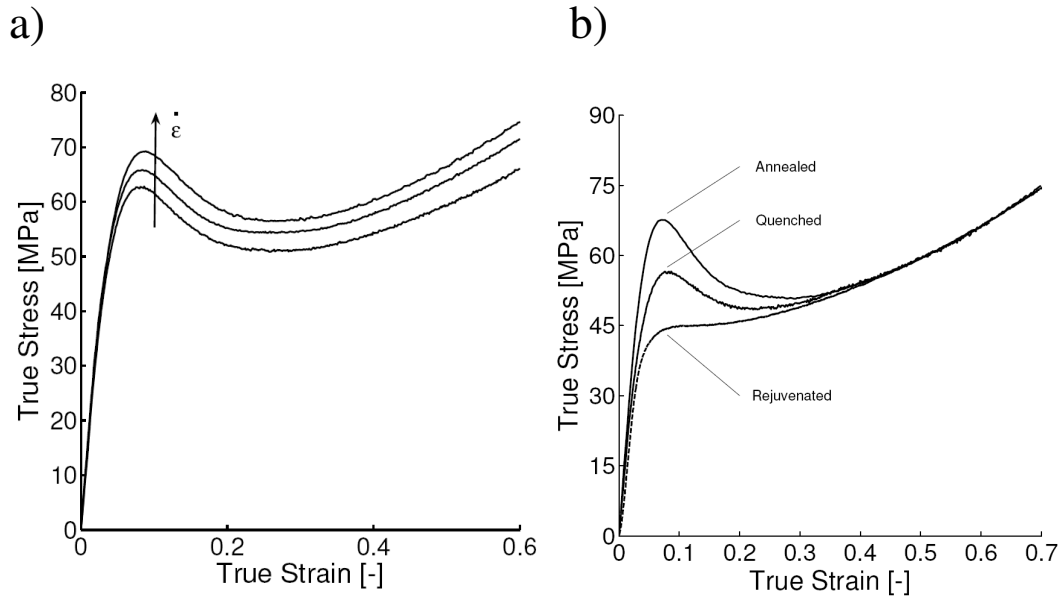


**Figure 4.2:** Intrinsic behavior of amorphous polymer: a) under the influence of different true strain rates and; b) at different thermal histories.

contributions, first proposed by Haward and Thackray [19]:

$$\boldsymbol{\sigma} = \boldsymbol{\sigma}_s + \boldsymbol{\sigma}_r \quad (4.4)$$

in which  $\boldsymbol{\sigma}_r$  denotes the strain hardening contribution that is attributed to molecular orientation of the entangled network, modeled using a Neo-Hookean elastic expression [13, 20]:

$$\boldsymbol{\sigma}_r = G_r \tilde{\mathbf{B}}^d \quad (4.5)$$

where  $G_r$  is the strain hardening modulus,  $\tilde{\mathbf{B}}^d$  is the isochoric left-Cauchy-Green deformation tensor, and the superscript  $d$  denotes that we take the deviatoric part.

The so-called driving stress  $\boldsymbol{\sigma}_s$  in Equation 4.4 accounts for the rate-dependent plastic flow response, attributed to intermolecular interactions on a segmental scale [12, 18] and is represented by a compressible Leonov model [17, 21]:

$$\boldsymbol{\sigma}_s = K(J - 1)\mathbf{I} + G\tilde{\mathbf{B}}_e^d \quad (4.6)$$

where  $K$  is the bulk modulus and  $G$  is the shear modulus. The relative volume change  $J$  and the isochoric elastic left Cauchy Green deformation tensor  $\tilde{\mathbf{B}}_e$  are implicitly given by:

$$\dot{J} = J \cdot \text{tr}(\mathbf{D}) \quad (4.7)$$

$$\tilde{\mathbf{B}}_e^{\circ} = (\mathbf{D}^d - \mathbf{D}_p^d) \cdot \tilde{\mathbf{B}}_e + \tilde{\mathbf{B}}_e \cdot (\mathbf{D}^d - \mathbf{D}_p^d) \quad (4.8)$$

The left hand side of Equation 4.8 represents the (objective) Jaumann derivative of the isochoric elastic left Cauchy Green tensor. The tensor  $\mathbf{D}$  denotes the rate of deformation tensor, and  $\mathbf{D}_p$  the is plastic rate of deformation tensor. To complete the constitutive description the plastic deformation rate is expressed in the Cauchy stress tensor by a generalized non-Newtonian flow rule:

$$\mathbf{D}_p = \frac{\boldsymbol{\sigma}_s^d}{2\eta(\bar{\tau}, p, S_a)} \quad (4.9)$$

Under isothermal conditions the nonlinearity of the model is completely governed by the stress-, pressure- and state-dependent viscosity  $\eta$ , defined as [18]

$$\eta(\bar{\tau}, p, S) = \eta_{o,r} \underbrace{\frac{\bar{\tau}/\tau_0}{\sinh(\bar{\tau}/\tau_0)}}_{(I)} \underbrace{\exp\left(\frac{\mu p}{\tau_0}\right)}_{(II)} \underbrace{\exp(S_a(t) \cdot R_\gamma(\bar{y}_p))}_{(III)} \quad (4.10)$$

Here the parameter  $\eta_{o,r}$  represents the zero-viscosity for the completely rejuvenated (unaged) state. The part marked (I), with  $\bar{\tau}$  being the equivalent stress [22], represents the stress dependent part of the viscosity governed by the parameter  $\tau_0$ . Part (II) is the pressure dependent part, governed by the pressure dependence parameter  $\mu$  and the hydrostatic pressure  $p$  [23]. The combination of part (I) and (II) gives a rate dependent plastic flow response according to the pressure modified Eyring flow expression [24, 25]. Finally, part (III) represents the dependence of the viscosity on physical aging and rejuvenation (strain softening) this on the temperature- and deformation history. The parameter  $S_a$  can be regarded as a state parameter that uniquely determines the current

state of the material. Evolution of  $S_a$  with time allows us to capture the change of mechanical properties over time as a result of physical aging. In the present investigation, we will only consider materials with different initial  $S_a$  values (obtained by application of different thermal histories).

The function  $R_\gamma$  in Equation 4.10 describes the strain softening process that is the erasure of thermal history by plastic deformation. It is expressed as:

$$R_\gamma(\bar{\gamma}_{pl}) = \frac{\left(1 + (r_0 \cdot \exp(\bar{\gamma}_p))^{r_1}\right)^{\frac{r_2-1}{r_1}}}{\left(1 + r_0^{r_1}\right)^{\frac{r_2-1}{r_1}}} \quad (4.11)$$

where  $r_0$ ,  $r_1$  and  $r_2$  are fitting parameters, and  $\bar{\gamma}_p$  denotes the equivalent plastic strain [26].

The essence of the influence of physical aging and of strain softening, modeled by the state parameter  $S_a$  (Equation 4.10), is illustrated in Figure 4.3a which shows the strain-rate dependence of the yield stress resulting from Equation 4.10. In the reference state, i.e. the fully rejuvenated state, the parameter  $S_a$  is initially equal to zero. With physical aging (also during processing) the value of  $S_a$  increases, which leads to a shift of the yield stress- strain rate along the log (strain rate) axis. At a constant strain rate, the

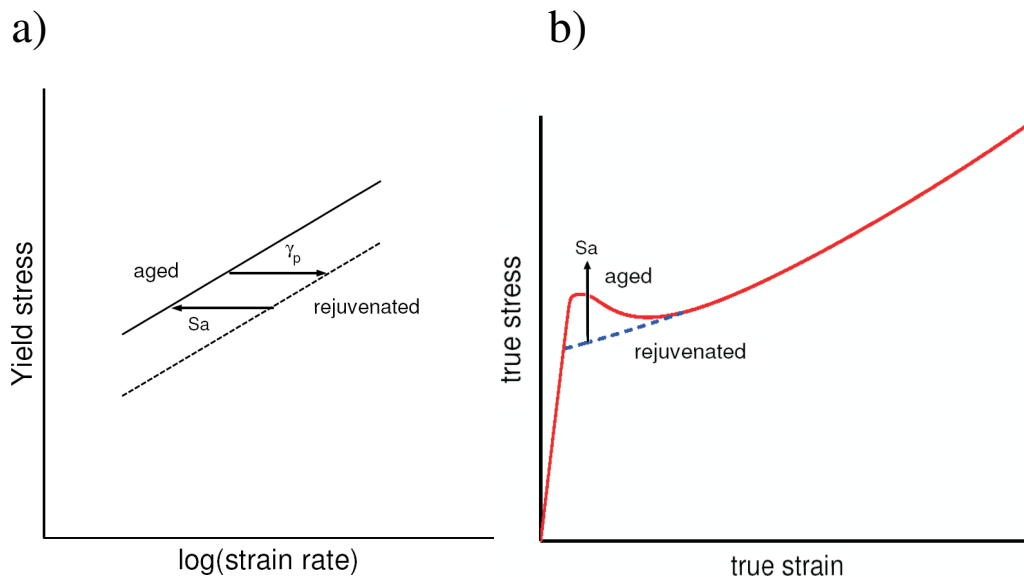


**Figure 4.3:** a) influence of the thermal history and strain softening on the strain rate dependence of the yield stress; b) intrinsic stress-strain curve indicating the influence of the physical aging.

result is an increase in yield stress compared to that of the rejuvenated state. Upon deformation, the increasing equivalent plastic strain  $\bar{\gamma}_p$  triggers strain softening (Equation 4.11) and the yield stress shifts back to that of the rejuvenated state. As a result of rejuvenation due to deformation, the yield stress drops with increasing strain and the intrinsic stress-strain curve evolves back to that of the rejuvenated state at large strains (see Figure 4.3b).

For polycarbonate (PC) the parameters in the model (see Table 4.1 [18]) prove to be independent of the molecular weight distribution and the key parameter, needed to adjust for differences in thermal history (illustrated in Figure 4.2b), is the initial value of the state parameter  $S_a$ .

**Table 4.1:** Material parameters used for the numerical simulation of tensile and compression tests on PC.

$K$ [MPa]	$G$ [MPa]	$G_r$ [MPa]	$\eta_{o,r}$ [MPa·s]	$\tau_o$ [MPa]	$\mu$	$S_a$ [-]
3750	321	26	$2.1 \cdot 10^{11}$	0.7	0.08	-

### 4.3.2. Indentation modeling

In the present model, the elastic regime is approximated with compressible, linear-elastic behavior. To correctly describe post-yield response, the elastic modulus is generally chosen such that the yield strain is accurately predicted, see Figure 4.4a. This is justified

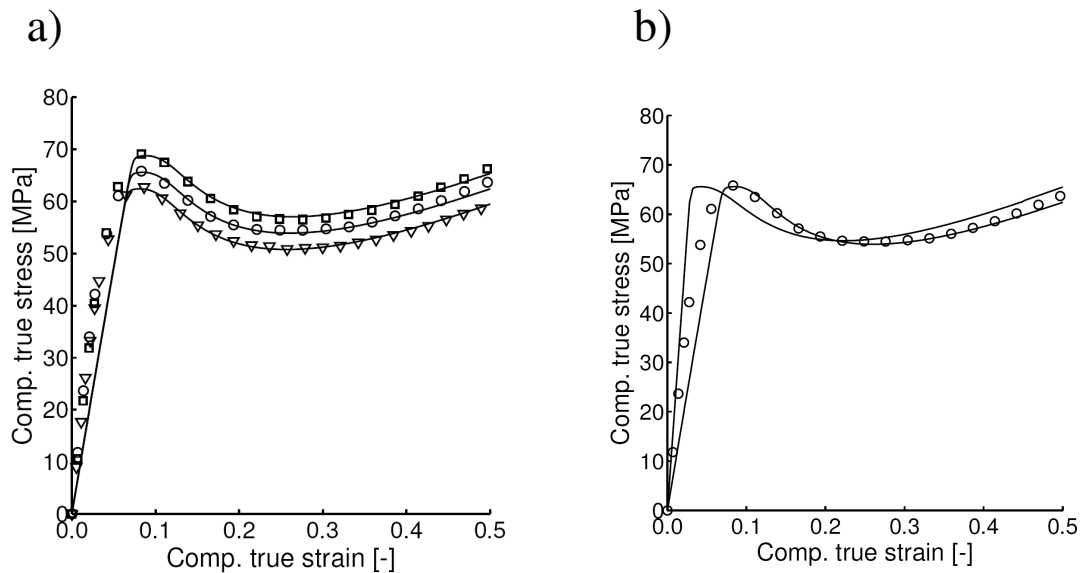


**Figure 4.4:** Compression tests: a) experiments (open symbols) compared with the numerical simulation (solid lines) using material parameters presented in Table 4.1 for three different true strain rates:  $10^{-2} \text{ s}^{-1}$  ( $\square$ ),  $10^{-3} \text{ s}^{-1}$  ( $\circ$ ),  $10^{-4} \text{ s}^{-1}$  ( $\nabla$ ); b) simulated compression tests (solid lines) for two different values of the elastic modulus ( $E = 900 \text{ MPa}$  and  $E = 2.2 \text{ MPa}$ , see Table 4.2) compared with the experiments ( $\circ$ ).

for problems in which large strains are predominant. For polycarbonate, this yields a value of 900 MPa [14] which is much smaller than the 2200-2400 MPa generally observed. For indentation, where the elastic deformation also significantly contributes at larger depth, a drastic underestimation of the material resistance is obtained when the modulus is chosen too low. Two possibilities are available to solve this problem. The first is to use a multimode version of the model to describe the complete pre-yield viscoelastic behavior. In previous work we showed that the behavior can be accurately captured by a parallel arrangement of eighteen modes [12]. Unfortunately, this solution increases the computation time tremendously and will therefore not be used. The second possibility consists of a simple increase of the elastic modulus, which requires adaptation of another single parameter,  $\eta_0$ , to assure that the post yield response remains identical, see Figure 4.4b. In that case the modeled yield strain is smaller than the experimental one. The new set of parameters used for the indentation simulation is presented in Table 4.2.

Simulations are performed using the Marc / Mentat finite element package. The finite element mesh used for the simulation is depicted in Figure 4.5. Axisymmetric quadrilateral linear elements are used. The total domain shown in Figure 4.5a has dimensions 1 mm x 1 mm and consists of 2192 nodes and 2061 elements. The mesh becomes more refined towards the region of contact (Figure 4.5b) and the size of the elements which come into contact with the indenter is about 300 nm. The indenter is modeled as a rigid sphere with a radius of 100  $\mu\text{m}$ , and the contact is assumed to be frictionless. The contact radius is estimated by the y coordinate of the last node in contact.

**Table 4.2:** Material parameters used for the numerical simulation of indentation tests on PC.

$K$ [MPa]	$G$ [MPa]	$G_r$ [MPa]	$\eta_{0,r}$ [MPa·s]	$\tau_0$ [MPa]	$\mu$	$S_a$ [-]
3750	784	26	$2.8 \cdot 10^{12}$	0.7	0.08	-

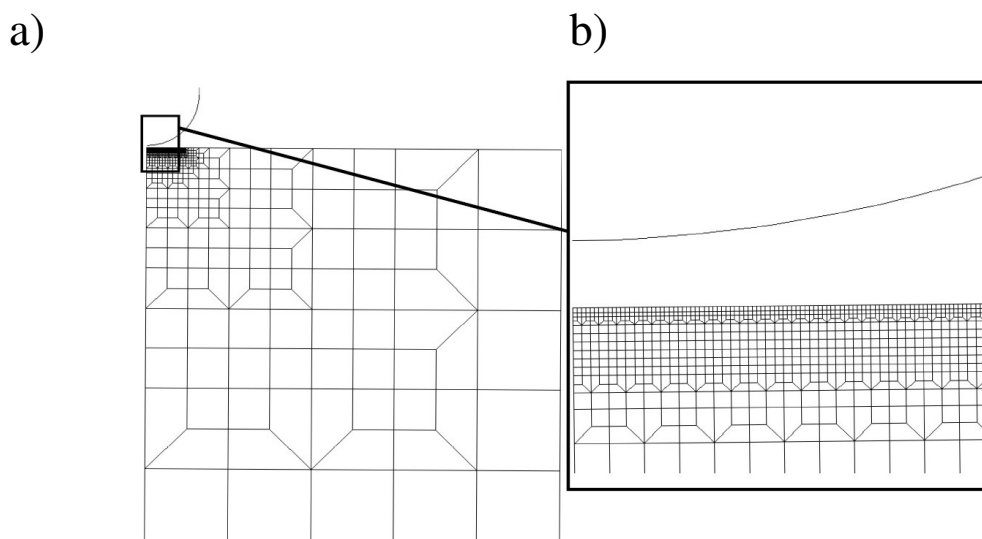


**Figure 4.5:** Finite element mesh used to simulate the indentation tests.

## 4.4. Materials and experimental methods

### 4.4.1. Materials

The material used in this study is polycarbonate (Makrolon, Bayer), obtained in the form of extruded sheet of 3 mm thickness. Prior to the indentation tests, the sheet roughness is determined by using a commercial Atomic Force Microscope (Digital Instruments, Nanoscope IIIa) operating in tapping mode. A mean roughness,  $R_a$ , of about 5 nm is measured.

From the extruded sheet, samples with a size of 10 mm x 10 mm are cut. For half of the samples no further heat treatment is applied prior to indentation. The other half is annealed at 130°C for 24 hours in an air circulated oven and subsequently cooled down slowly to room temperature.

### 4.4.2. Optical indentation microscope

In order to make *in situ* observations of the contact area during indentation tests, a unique indentation device has been designed where a transparent indenter is coupled with a microscope and a CCD camera (see Figure 4.6) [15, 16]. The tip of the indenter is optically aligned to a microscope and a CCD-video-camera and the contact area is observed through the indenter tip. At the maximum magnification, the inaccuracy in the lengths measured on video-images is  $\pm 0.5 \mu\text{m}$ . The depth of penetration ( $h$ ) is measured by a couple of linear transducers and the indentation load ( $P$ ) is monitored by a load cell. A diamond cone indenter (the apex angle of 90 degree) with a tip radius of  $100 \mu\text{m}$  is used. This tip geometry offers the possibility to fully exploit the advantage of the axisymmetry condition for the numerical simulation and to reduce the number of elements. Using the instrumented indentation microscope, the contact area can be determined directly without approximation or assumption.

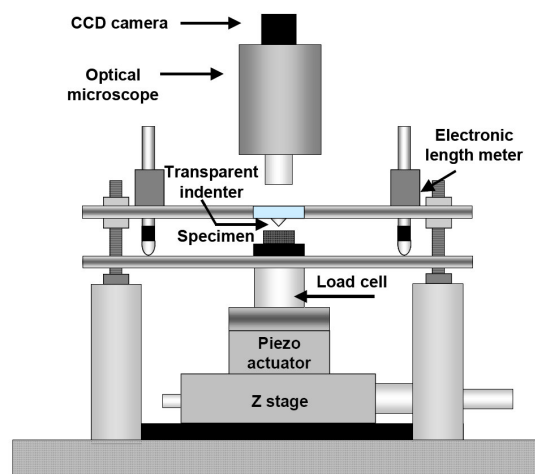


**Figure 4.6:** Instrumented indentation microscope set up.

Indentation tests are performed at a displacement rate of  $0.1 \mu\text{m}\cdot\text{s}^{-1}$ ,  $1 \mu\text{m}\cdot\text{s}^{-1}$  and  $5 \mu\text{m}\cdot\text{s}^{-1}$  up to a maximum load of approximately 1 N, followed by unloading with the same displacement rate. Since the main interest is in the loading, no holding time at the maximum of the loading is applied.

For the load relaxation tests, the indenter penetrated into the sample at a speed of  $1 \mu\text{m}\cdot\text{s}^{-1}$  until a maximum force of approximately 1.1 N is reached. The depth of penetration is then fixed at the value at the peak load during the load relaxation.

## 4.5. Results and discussion

### 4.5.1. Experimental determination of the contact area

Using the instrumented indentation microscope, the contact area is continuously recorded during indentation tests. Figure 4.7a shows the development of the contact area during the loading. The images are captured *in-situ* during indentation tests on PC. Figure 4.7b shows the state of the deformation corresponding to the images. As expected the contact area increases gradually with an increasing indentation depth, see Figure 4.7a.

The diameter of the contact radius is determined from the pictures, using an image processing program. From the contact radius  $a$  obtained, the contact area  $A_p$  is subsequently calculated as  $A_p = \pi a^2$ , and then plotted against the penetration displacement  $h$  in Figure 4.7c. For the lower indentation depths (up to  $1.8 \mu\text{m}$ ), the experimental contact area as function of the displacement shows a linear dependence, indicating an Hertzian contact (Figure 4.7c). At deeper indentation depth, this trend gradually deviates from the linearity, indicating the occurrence of plastic deformation.

### 4.5.2. Numerical simulation vs. experiments

To complete the constitutive model for our materials, the state parameter  $S_a$  must be determined in addition to the already known parameters listed in Table 4.2. This is done by carrying out macroscopic tensile tests on the as received and on the annealed materials. Experiments are performed at an engineering strain rate of  $10^{-3} \text{s}^{-1}$  on samples with geometry according to ISO 527. Numerical simulations of the tensile tests are performed using the 3D tensile bar geometry and  $S_a$  values are subsequently increased until the simulated yield stress agree well with the experimental one. For the as received PC a yield stress of 63 MPa leads to a value of 31.7 for  $S_a$ . For the annealed material, a yield stress of 71 MPa corresponds to a value of 39 for  $S_a$ .

The experimental indentation tests, performed with the optical indentation microscope, are simulated using these values for the state parameter. A direct comparison between the numerical simulation and experiments, shown in Figure 4.8, proves that the model can perfectly predict the experimental load-displacement curves (Figure 4.8a) as well as the evolution of the experimental contact areas during the indentation tests (Figure 4.8b). At small indentation depth, the contact follows a Hertzian description, hence it is purely elastic. In contrast, at deeper indentation depth, the curves gradually



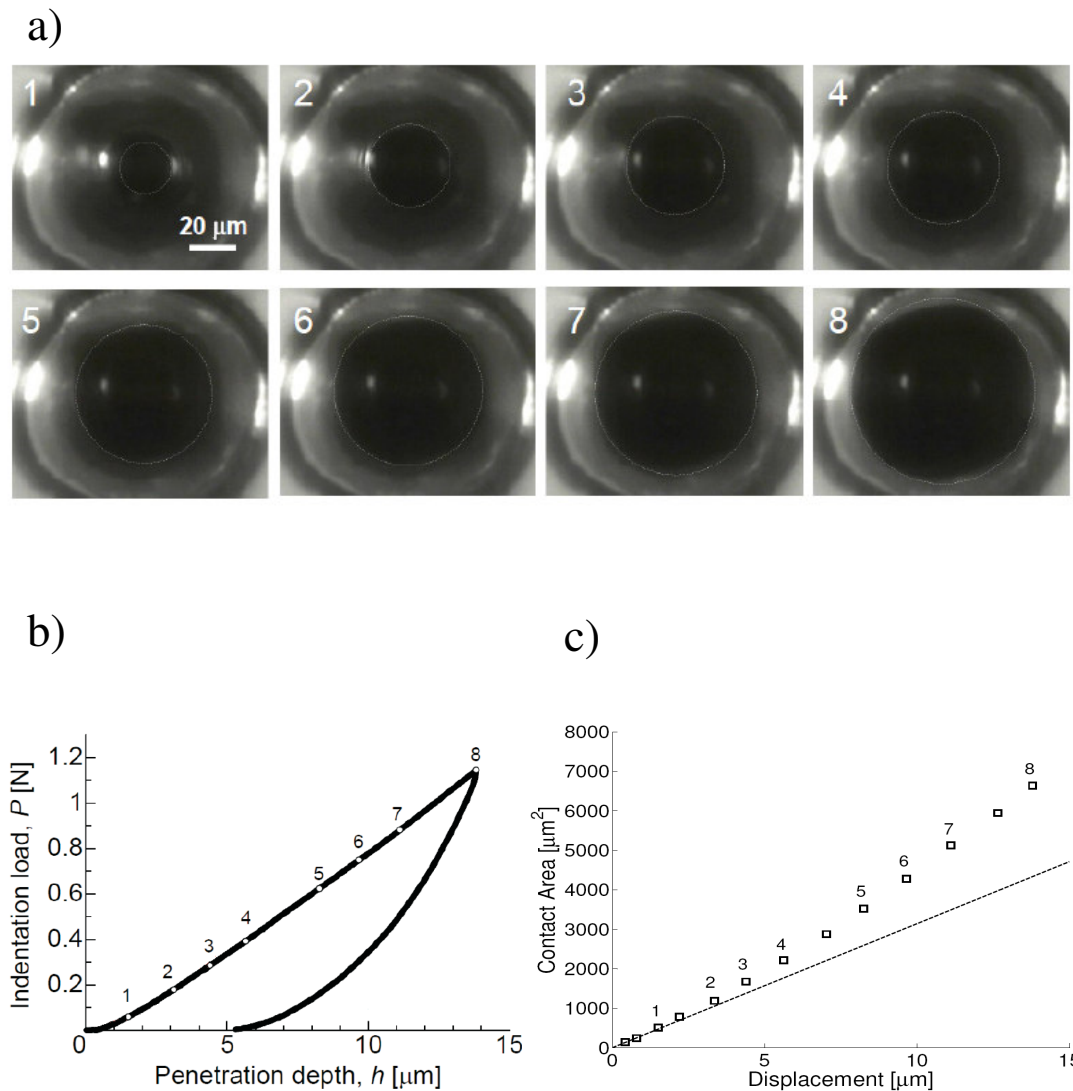


**Figure 4.7:** Contact area measurements: a) pictures of the contact area obtained *in situ* during indentation tests; b) load displacement curve indicating at which state of the deformation the pictures were recorded; c) experimental contact area ( $\square$ ), determined from the pictures, as function of the indentation depth. The dashed line corresponds to a Hertzian contact.

deviate from the the Hertzian contact due to onset of plastic deformation. In addition, it is observed that annealing leads to a shift of the load-displacement curve towards higher force at the same indentation Hertzian contact due to onset of plastic deformation. In addition, it is observed that annealing depth and a shift towards a deeper indentation depth for the same contact area (Figure 4.8). In general, these observations are in agreement with an extension of the elastic range due to an increase of the yield stress.

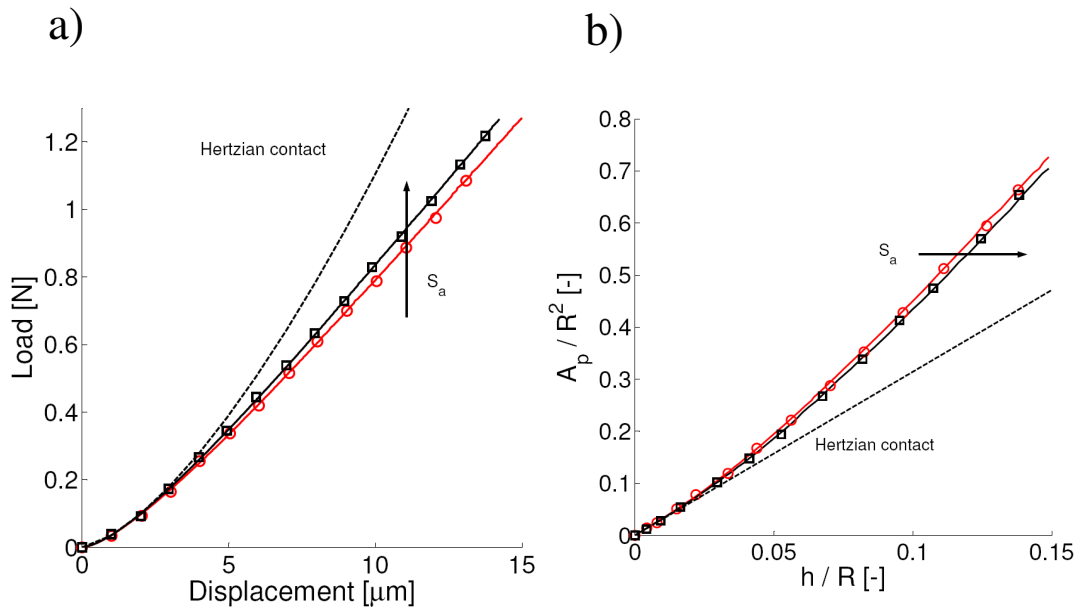


**Figure 4.8:** Indentation experiments (open symbols) compared with the numerical simulation (solid line) for two different thermal histories: annealed ( $\square$ ) and as received ( $\circ$ ): a) for the load-displacement and; b) for the contact area normalized with the square of the tip radius as function of the displacement normalized with the radius ( $100 \mu\text{m}$ ).

Annealing leads to an increase of the yield stress and it therefore extends the elastic range.

Since mechanical properties of glassy polymers are time-dependent, the effect of the indentation speed on the evolution of the contact area is also investigated. Simulation of indentation tests on the as-received polycarbonate at different speeds ( $0.1 \mu\text{m}\cdot\text{s}^{-1}$  and  $5 \mu\text{m}\cdot\text{s}^{-1}$ ) are therefore performed and compared with the experiments. Figure 4.9 presents this comparison and shows that the model perfectly predicts the experimental load-displacement curves, see Figure 4.9a, as well as the evolution of the contact areas during indentation at different speeds (Figure 4.9b). Again the curves follow the Hertzian contact at low displacement, and gradually deviate at larger displacement after the onset of plastic deformation. Moreover, an increase in speed leads to an increase in yield stress and therefore to a prolonged elastic range during the indentation.

A difference of a factor 50 in speed leads to a difference of 5 MPa in the yield stress. Besides the difference in yield stress between the “as received” and annealed PC is 8 MPa. Although the influence on the yield strength of the annealing step is more pronounced than that of the indentation speed (in the range between  $0.1 \mu\text{m}\cdot\text{s}^{-1}$  and  $5 \mu\text{m}\cdot\text{s}^{-1}$ ), it can be seen from a comparison between Figures 4.8 and 4.9, that the thermal-history effect induces a slightly smaller effect on the evolution of the contact area than the speed. This agrees well with the fact that by increasing the speed the complete

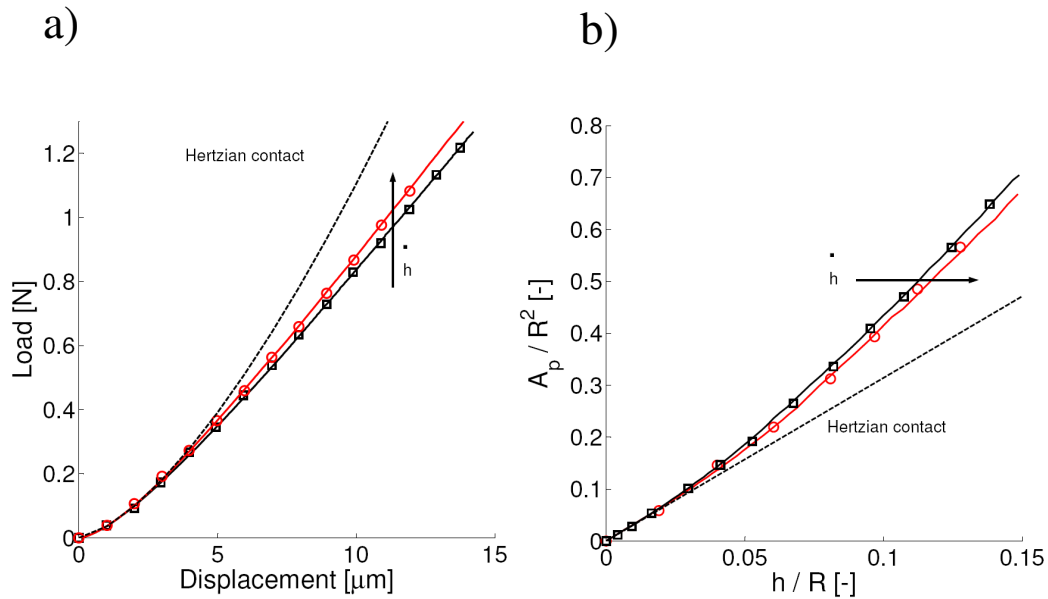


**Figure 4.9:** Indentation experiments (open symbols) compared with the numerical simulation (solid line) for two different speeds:  $\dot{h} = 0.1 \mu\text{m}\cdot\text{s}^{-1}$  ( $\square$ ) and  $5 \mu\text{m}\cdot\text{s}^{-1}$  ( $\circ$ ): a) for the load-displacement and b) for the contact area normalized with the square of the tip radius as a function of the displacement normalized with the radius.

intrinsic response of the PC is shifted to higher stress whereas the thermal-history only induces differences in the intrinsic response close to the yield stress (see Figure 4.2).

#### 4.5.3. Large deformation investigation: pile-up

To further investigate the effect of thermal history on the evolution of the contact area we perform numerical simulations of indentations to large indentation depths for two extreme values of  $S_a$ ; 0, which is the completely rejuvenated state, and 30, further referred as slightly annealed, for a speed of  $0.1 \mu\text{m}\cdot\text{s}^{-1}$ . The difference in intrinsic behavior between these two materials is illustrated in Figure 4.2b. Figure 4.10a presents the calculated contact-area evolution during indentation for both cases. At indentation depths smaller than  $20 \mu\text{m}$  (i.e.,  $h / R < 0.2$ ), the curves exhibit a similar trend as that observed in Figure 4.8b, i.e. a shift of the contact area evolution towards larger depths with increasing value of  $S_a$ . Remarkably, however, this trend is inverted for larger indentation depths ( $>20 \mu\text{m}$ ), i.e. a shift of the contact area evolution towards *smaller* depths with increasing value of  $S_a$ .

The occurrence of this trend inversion is clearly coupled to the presence of strain softening in the case of  $S_a=30$ , and not to a simple increase of the yield stress. This is supported by the results in Figure 4.10b of simulations of indentation of the rejuvenated

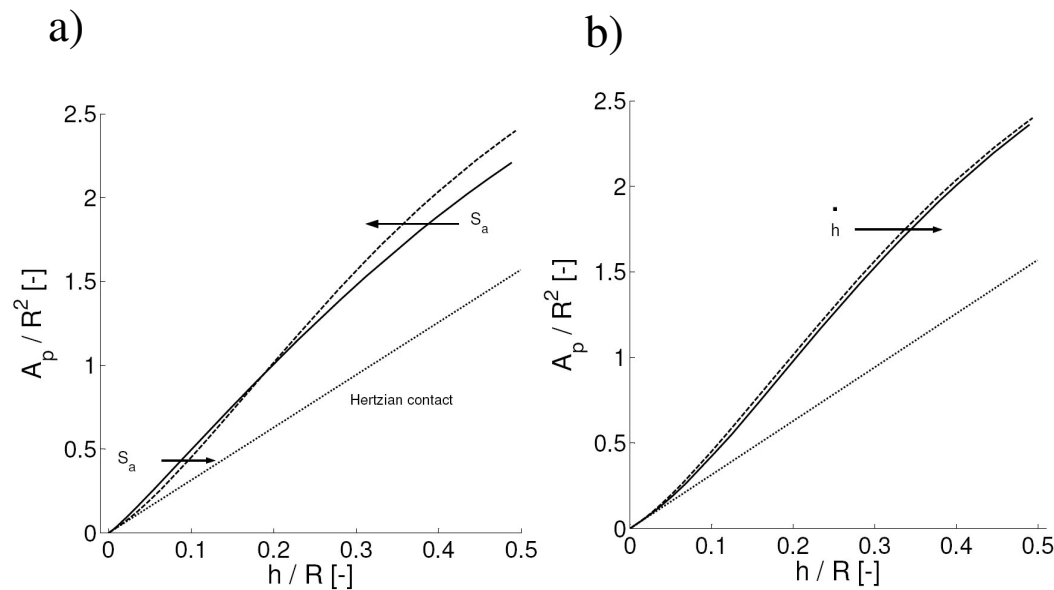


**Figure 4.10:** Normalized contact area as function of the normalized indentation depth: a) for two different thermal-histories modelled by two different  $S_a$  values: 0 (rejuvenated) for the solid line and 30 (annealed) for the dashed line; b) for two different speeds ( $S_a=0$ ):  $10 \mu\text{m}\cdot\text{s}^{-1}$  for the solid line and  $0.1 \mu\text{m}\cdot\text{s}^{-1}$  for the dashed line.

material ( $S_a=0$ ) at two different speeds ( $0.1 \mu\text{m}\cdot\text{s}^{-1}$  and  $10 \mu\text{m}\cdot\text{s}^{-1}$ ). The increase of indentation speed leads to an increase in yield stress, but for both speeds strain softening is absent ( $S_a=0$ ).

Since the evolution of the contact area is related to the contact geometry, i.e. pile-up or sink-in, we now plot the surface profile in the vicinity of the tip obtained for  $S_a=0$  and  $S_a=30$  at different indentation depths, see Figure 4.11. This figure shows that, at low depths, the surface exhibits the same sink-in profile for both the annealed and rejuvenated

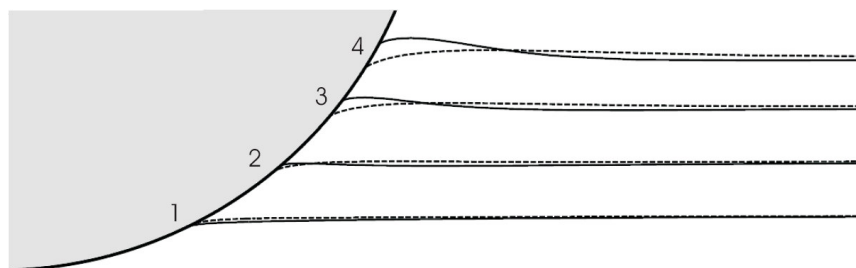


**Figure 4.11:** Contact profile for the slightly annealed material (solid line) and the rejuvenated material (dashed line) at different indentation depths ( $12.5 \mu\text{m}$  for profile number 1,  $25 \mu\text{m}$  for number 2,  $37.5 \mu\text{m}$  for number 3 and  $50 \mu\text{m}$  for number 4).

material. At large indentation depth, the simulations show that the annealed material piles-up whereas the rejuvenated material sinks-in near the tip. Therefore the trend inversion in the contact area evolution observed in Figure 4.10a, results from the difference in the contact geometry, which is determined by the post-yield behavior. In general, strain softening promotes the occurrence of strain localization phenomena [27]. The occurrence of pile-up for the annealed material appears to be a related phenomenon. This becomes especially clear if we look at Figure 4.12. This figure represents the surface profile at the maximum depth. It can be seen that for both materials, the surface piles-up but the effect is much more pronounced for  $S_a=30$ . Moreover, even if the surface piles-up for the rejuvenated material, it does not affect the contact area evolution. Reason is that the first contact point between the surface and the tip (D in Figure 4.12) is lower than the free surface. Therefore, this indicates a sink-in contact which is consistent with observations from Figure 4.11. For the slightly annealed material an opposite situation is observed. The differences between the two materials are caused by the strain softening behavior of the annealed material that localizes the deformation close to the contact region, whereas the absence of strain softening for the fully rejuvenated sample distributes the deformation over a larger volume of the material.

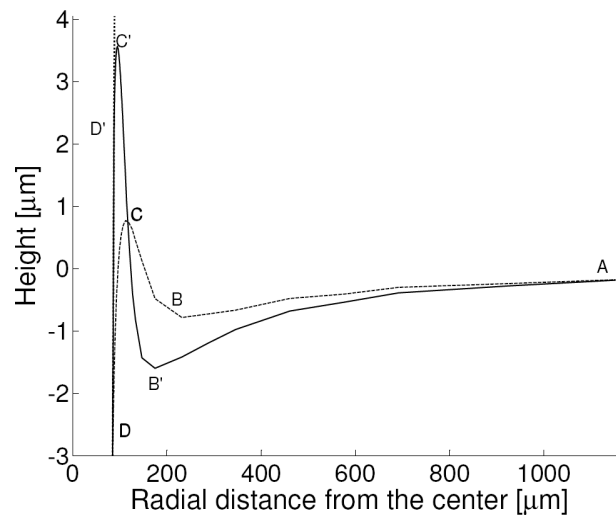


**Figure 4.12:** Simulated contact profile as function of the radial distance from the center: for the rejuvenated PC (dashed line: ABCD) and slightly annealed PC (solid line: AB'C'D') at an indentation depth of 50  $\mu\text{m}$ . The dotted line on the left represents the tip profile

#### 4.5.4. Relaxation

Load relaxation indentation has been performed and simulated for an as-received polycarbonate sample for which no further heat treatment has been applied, using the

experimental conditions described in the section 4.3.2. It should be noticed that our model takes into account only plastic effects, and no viscoelastic relaxation is incorporated, given the only one-mode version used here. The intention is to have an estimation of the contribution of plasticity to stress relaxation during indentation. Figure 4.13 represents the simulation of the load relaxation test, using only a plastic model, compared with the experiments. It is shown that the simulated plastic contribution represents 40% of the observed force relaxation, which is quite substantial.

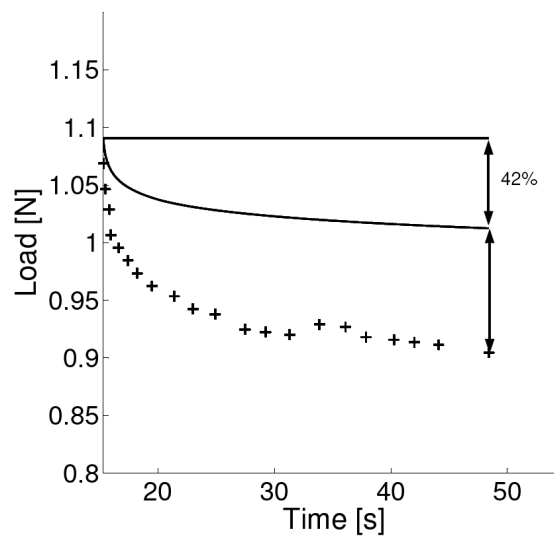


**Figure 4.13:** Experimental indentation load relaxation test result (+) compared with the simulation (solid line) using a one mode version of the model that incorporates only plasticity, but no viscoelasticity.

## 4.6. Conclusions

The evolution of the contact area between a spherical indenter and a polycarbonate surface was measured *in-situ* using a specially designed instrumented indentation microscope. Indentations on PC samples with two different thermal histories were performed at two different speeds and, subsequently compared with numerical simulations carried out using an advanced elasto-plastic constitutive model for polycarbonate. The parameters used in the constitutive model were determined using tensile tests. For all cases, the numerical model perfectly predicted the development of the contact area during indentation. The results show that by annealing or by increasing the speed, the purely elastic range is extended during indentation due to the increase of the yield stress, which leads to a decrease in contact area at equal indentation depths.

Using numerical simulation, it is also shown that the post yield behavior of the material has a dominant influence on the contact geometry, which may exhibit pile-up or

sink-in. Particularly, pile-up results from localization effects and it is therefore promoted by strain softening.

Finally, in load-relaxation indentation of polycarbonate, using our model, we found that approximately half of the total relaxation is constituted by plasticity, on top of possible viscous effects.

## References

- [1] H. Hertz, *Über die Berührung Fester Elastischer Körper (On the contact of elastic solids)*. J. Reine Angew. Math., 1881. **92**: p. 156-171.
- [2] W.C. Oliver and G.M. Pharr, *An improved technique for determining hardness and elastic-modulus using load and displacement sensing indentation experiments*. J Mater. Res., 1992. **7**(6): p. 1564 - 1583.
- [3] J.S. Field and M.V. Swain, *A simple prediction model for spherical indentation*. J Mater. Res., 1993. **8**(2): p. 297-306.
- [4] A. Bolshakov and G.M. Pharr, *Influence of pileup on the measurement of mechanical properties by load and depth sensing indentation techniques*. J. Mat. Res., 1998. **13**(4): p. 1049-1058.
- [5] B. Taljat and G.M. Pharr, *Development of the pile-up during spherical indentation of elastic-plastic solids*. Int. J. of Solid and Structures, 2004. **41**: p. 3891-3904.
- [6] M.C. Boyce, D.M. Parks, and A.S. Argon, *Large inelastic deformation of glassy polymers. Part I: Rate dependent constitutive model*. Mech. of Mat., 1988. **7**: p. 15-33.
- [7] E.M. Arruda and M.C. Boyce, *Evolution of plastic anisotropy in amorphous polymers during finite straining*. Int. J. Plast., 1993. **9**: p. 697-720.
- [8] O.A. Hasan and M.C. Boyce, *A constitutive model for the nonlinear viscoelastic viscoplastic behaviour of glassy polymers*. Polym. Eng. Sci., 1995. **35**: p. 331-344.
- [9] C.P. Buckley and D.C. Jones, *Glass-rubber constitutive model for amorphous polymers near the glass transition*. Polymer, 1995. **36**: p. 3301-3312.
- [10] P.J. Dooling, C.P. Buckley, and S. Hinduja, *The onset of the nonlinear viscoelasticity in multiaxial creep of glassy polymers: a constitutive model and its application to PMMA*. Polym. Eng. Sci., 1998. **38**: p. 892-904.
- [11] C. Gerlach, C.P. Buckley, and D.P. Jones, *Development of an integrated approach to modelling of polymer film orientation processes*. Trans. Inst. Chem.

- Eng. Part A, 1998. **76**: p. 38-44.
- [12] T.A. Tervoort, E.T.J. Klompen, and L.E. Govaert, *A multi-mode approach to finite, three-dimensional, nonlinear viscoelastic behaviour of glassy polymer*. J. Rheol., 1996. **40**: p. 779-797.
- [13] L.E. Govaert, P.H.M. Timmermans, and W.A.M. Brekelmans, *The influence of intrinsic strain softening on strain localization in polycarbonate: modeling and experimental validation*. J. Eng. Mat. and Tech., 2000. **122**: p. 177-185.
- [14] E.T.J. Klompen, T.A.P. Engels, L.E. Govaert, and H.E.H. Meijer, *Modelling of the post-yield response of glassy polymers: influence of thermomechanical history*. Macromol., 2005. **38**: p. 6997-7008.
- [15] T. Miyajima and M. Sakai, *Optical indentation microscopy - a new family of instrumented indentation testing*. Phil. Mag., 2006. **86**(33-35): p. 5729-5737.
- [16] M. Sakai, N. Hakiri, and T. Miyajima, *Instrumented indentation microscope: A powerful tool for the mechanical characterization in microscales*. J. Mat. Res., 2006. **21**(9): p. 2298-2303.
- [17] T.A. Tervoort, R.J.M. Smit, W.A.M. Brekelmans, and L.E. Govaert, *A constitutive equation for the elasto-viscoplastic deformation of glassy polymers*. Mech. Time-Dep. Mater., 1998. **1**(3): p. 269-291.
- [18] E.T.J. Klompen, T.A.P. Engels, L.C.A. van Breemen, P.J.G. Schreurs, L.E. Govaert, and H.E.H. Meijer, *Quantitative Prediction of Long-Term Failure of Polycarbonate*. Macromol., 2005. **38**: p. 7009-7017.
- [19] R.N. Haward and G. Thackray, *Use of a mathematical model to describe isothermal stress-strain curves in glassy thermoplastics*. Proc. Royal Soc. London A., 1967. **302**: p. 453-472.
- [20] T.A. Tervoort and L.E. Govaert, *Strain hardening behavior of polycarbonate in the glassy state*. J. Rheol., 2000. **44**(6): p. 1263 - 1277.
- [21] F.P.T. Baaijens, *Calculation of residual stresses in injection molded products*. Rheol. Acta, 1991. **30**: p. 284-299.
- [22] Defined as  $\bar{\tau} = \sqrt{\frac{1}{2} \text{tr}(\sigma_s^d \sigma_s^d)}$
- [23] Defined as  $p = -\frac{1}{3} \text{tr}(\sigma_s)$
- [24] I.M. Ward, *The yield behaviour of polymers*. J. Mater. Res., 1971. **6**: p. 1397-1417.
- [25] R.A. Duckett, B.C. Goswami, L.S.A. Smith, I.M. Ward, and A.M. Zihlif, *The yielding and crazing behaviour of polycarbonate in torsion under superposed hydrostatic pressure*. Brit. Polym. J., 1978. **10**: p. 11-16.



[26] Defined as  $\dot{\gamma}_p = \sqrt{\text{tr}(\mathbf{D}_p \cdot \mathbf{D}_p)}$

[27] H.G.H. Van Melick, L.E. Govaert, and H.E.H. Meijer, *Localization phenomena in glassy polymers: influence of thermal and mechanical history*. Polymer, 2003. **44**: p. 3579-3591.

## Chapter 5

# Viscoelastic film properties determined using indentation and conventional testing: a comparison

---

### Abstract:

Instrumented indentation is used to determine the linear viscoelastic properties of two acrylate films with different glass transition temperatures ( $T_g$ ). The results are compared to data obtained with a classical rheological method, DMTA. The creep compliance and relaxation moduli are predicted from the dynamical properties obtained from DMTA tests by using the linear viscoelastic theory. In addition, these properties are measured using indentation-creep and indentation relaxation (quasi-static) measurements, as well as from dynamic indentation testing. For the lower-  $T_g$  material, that exhibits a stronger time dependency, the viscoelastic properties determined under quasi-static and dynamic conditions are comparable to those obtained from DMTA. A difference of about 10 % between the two methods is generally found. On the contrary, the creep compliance and loss modulus for the higher-  $T_g$  material differs significantly from the DMTA data. This may be explained by the fact that the hard material has a weak time dependency and therefore the measurements are more sensitive to experimental errors.

## 5.1. Introduction

In instrumented indentation testing, an indenter is pressed into the surface of a material, meanwhile continuously monitoring the force applied and the displacement of the indenter. From the resulting load-displacement curves, mechanical properties like elastic modulus and hardness are determined [1, 2], as well as fracture behavior [3-8] and residual stresses [9-12]. Existing models used in those analyses are only valid when the time-dependency of the material is weak and can be neglected.

Many materials such as polymers, amorphous metals and inorganic glasses may, however, deform in a viscoelastical way, and the time dependency cannot be neglected. The extent of this time-dependency of course depends on the temperature applied and the experimental time-scale. For small displacements, the material viscoelastic response is often linear implying that the material state is not altered by the applied stress or strain.

In principle, time-dependent material properties can be probed by using quasi-static loading or dynamic loading. Some effort has been given to the development of analytical models to determine linear viscoelastic properties for quasi static [13-23] and dynamic loading [24-27]. Only few studies, however, are dedicated to compare viscoelastic properties obtained from indentation to results from conventional mechanical tests [28, 29]. These studies show a substantial discrepancy between the bulk rheometry characterization and instrumented indentation technique under quasi-static testing conditions [28], but a good agreement between dynamic indentation and the bulk rheological method [29].

Here we carry out a comparative study of viscoelastic properties obtained with indentation and the properties found with conventional DMTA testing. Dynamic and quasi-static indentation tests are carried out for two acrylate films with different glass transition temperatures. The linear viscoelastic properties obtained from indentation, like storage and loss moduli, as well as creep compliance and relaxation modulus, are compared to the properties obtained from the DMTA tests.

## 5.2. Theory

Linear viscoelastic problems can often be solved using the so-called correspondence principle. This method consist of removing the time dependence in the equations governing a viscoelastic problem by application of the Laplace transform. As a result the corresponding elastic problem with the same initial and boundary conditions is obtained. If the elastic problem can be solved, the viscoelastic solution is obtained from the elastic solution by applying the inverse Laplace transform. However, the correspondence principle is limited to the cases for which the boundary conditions are independent of time. Therefore, for contact problems in which the contact area increases with time this approach cannot be used in general, and viscoelastic solutions therefore can generally not be obtained from the associated elastic solution by replacing the elastic constant by the viscoelastic operator. Nevertheless, Lee and Radok [13] have shown that correct viscoelastic solutions still can be obtained using such an approach, if the contact area is monotonically increasing. Later, Ting [14, 15] and Graham [16, 17] used a different

approach and proposed a solution allowing for the contact area to pass through one or more maxima.

During so-called indentation-creep tests, a constant load, fixed in time, is applied while the change of the displacement is measured. In that case, for spherical creep indentation, the load and the displacement are related by the following equation [14, 15, 23]:

$$\frac{8}{3}\sqrt{R}h^{3/2}(t) = 2P_0(1-\nu^2)D(t) \quad (5.1)$$

where  $R$  is the tip radius,  $P_0$  is the constant applied load,  $h$  is the time dependent displacement,  $\nu$  is the Poisson's ratio and  $D(t)$  is the creep compliance. In contrast to the creep indentation experiment, in an indentation-relaxation experiment the displacement is kept constant while the time-evolution of the force is measured. In that case, the following relation describes the linear viscoelastic spherical indentation problem [14, 15, 23]:

$$P(t) = \frac{8}{3}\sqrt{R}h_0^{3/2}\frac{E(t)}{2(1-\nu^2)} \quad (5.2)$$

in which  $h_0$  is the constant displacement,  $P$  is the load, and  $E(t)$  the relaxation modulus. In Equations 5.1 and 5.2 the Poisson's ratio is assumed to be independent of time.

Another approach to obtain linear viscoelastic properties is to perform dynamic indentation tests [24-27]. In such tests, an oscillatory load, superposed on a fixed finite load, is applied and the resulting oscillating displacement is measured. The oscillatory load and resulting oscillating displacement are given by:

$$P(t) = P_0 e^{i(\omega t)} \quad (5.3)$$

$$h(t) = h_0 e^{i(\omega t + \varphi)} \quad (5.4)$$

where  $P_0$  is the force amplitude,  $h_0$  is the displacement amplitude,  $\omega$  is the frequency and  $\varphi$  is the phase shift of the displacement with respect to the oscillating force.

The dynamic instrument-sample interaction is represented by a damped harmonic oscillator model consisting of a combination of a spring and a dashpot [1, 25-27]. Since all motions are restricted to 1-D, the equation for the motion is a simple harmonic oscillator subjected to a force:

$$P(t) = m\ddot{h}(t) + D\dot{h}(t) + Kh(t) \quad (5.5)$$

where  $K$  is the equivalent stiffness (defined as a combination of the contact stiffness, the load frame stiffness and the support spring stiffness) and  $D$  is the damping factor in both indenter head and sample (defined as the sum of the damping factor of the indenter and the damping factor of the sample).

The stiffness,  $S$ , and the damping factor,  $D_s$ , are calculated from Equation 5.5 with the oscillating force and displacement expressed in Equation 5.3 and 5.4. The stiffness and the damping are then given by:

$$S = \left[ \frac{1}{\left| \frac{P_0}{h_0} \right| \cos \varphi - (K_s - m\omega^2)} - \frac{1}{K_f} \right]^{-1} \quad (5.6)$$

$$D_s \omega = \left| \frac{P_0}{h_0} \right| \sin \varphi - D_i \omega, \quad (5.7)$$

where  $K_s$  is the support spring stiffness,  $K_f$  is the load frame stiffness and  $D_i$  the damping factor of the indenter.

The storage and loss moduli are related respectively to the stiffness and the damping factor by assuming an elastic solution to the tip-sample contact. For a Berkovich indentation, the elastic solutions are those obtained by Oliver and Pharr [30]:

$$E_r = \frac{\sqrt{\pi} S}{2\beta\sqrt{A}} \quad (5.8)$$

where  $A$  is the contact area,  $\beta$  is a correction factor (=1.034) that takes into account the deviation in stiffness caused by the lack of axial symmetry of the Berkovich tip [31] and  $E_r$  is the reduced modulus, given by:

$$E_r = \frac{E}{1-\nu^2} \quad (5.9)$$

with  $E$  is the storage or loss modulus of the specimen and  $\nu$  is the Poisson's ratio (Equation 5.9 is valid only for the case where the sample is much more compliant than the indenter).

The reduced storage modulus  $E_r'$  and reduced loss modulus  $E_r''$  are then given by [25]:

$$E_r' = \frac{\sqrt{\pi}S}{2\beta\sqrt{A}} \quad (5.10)$$

$$E_r'' = \frac{\sqrt{\pi}D_s\omega}{2\beta\sqrt{A}}, \quad (5.11)$$

Equations 5.10 and 5.11 are obtained from Equation 5.8 by replacing the elastic constant by the viscoelastic operators. According to White *et. al.* [29] the correspondence principle is not properly used in this case since it can be used only when the contact area is monotonically increasing (which is not the case for dynamic contacts). Nevertheless they found a good agreement between dynamic indentation and DMTA [29].

### 5.3. Materials and methods

Samples investigated were two different acrylate films with a thickness of 100  $\mu\text{m}$ . The glass transition temperature of the two films was 323 K, (further referred as the soft material) and 353 K (hard material), respectively.

Quasi-static indentation tests were performed using a micro indenter custom-designed and made at Philips Research Laboratories in Eindhoven. Forces and displacements are measured by means of coils at the bottom of the indenter column with an accuracy of 2 mN and 20 nm respectively. We used a sapphire sphere indenter with a radius of 150  $\mu\text{m}$ . The compliance of the apparatus was determined by a reference measurement on silica glass with an elastic modulus of 72 GPa and a Poisson's ratio of 0.3. The compliance, determined from the experimental curve, was  $6 \cdot 10^{-2} \mu\text{m} \cdot \text{N}^{-1}$ .

During indentation creep tests, a constant applied force of 30 mN and 50 mN was reached in 0.4 s and maintained at this value for 1000 s meanwhile recording the displacement response. For relaxation tests, a displacement of 1.5  $\mu\text{m}$  for the soft material and 2.2  $\mu\text{m}$  for the hard material (reached in 0.4s) was kept constant during 1000 s while recording the load response. In order to minimize effects of thermal drift, the indenter was placed inside a cabinet and experiments were conducted in a temperature-controlled room. In order to stabilize the temperature, a waiting period of 1000 s was applied prior to the start of an experiment. All creep and relaxation tests were performed at a temperature of 299 K.

Dynamic indentation tests were carried out using a nano-indenter DCM (MTS Nano-Instruments, Oak Ridge, Tennessee). A Berkovich tip was used and pressed into the sample with a strain rate of  $0.05 \text{ s}^{-1}$  (defined as the speed divided by the depth) until a depth of 100 nm or 400 nm was reached. The tip was accordingly kept at this depth during the frequency sweep measurements. The range of frequencies investigated was from 1 to 300 Hz with a displacement amplitude of 1nm. Finally five indentation tests were performed at each indentation depth. The indentation tests were performed at a temperature of 298 K.

The DMTA measurements were performed in tension with a TA Instruments RSA-III dynamic mechanical analyzer in a frequency sweep mode. The temperature range was from 273 K to 348 K, with a step of 5 K. The frequency range was from 0.1 to 10 Hz.

## 5.4. Results and discussion

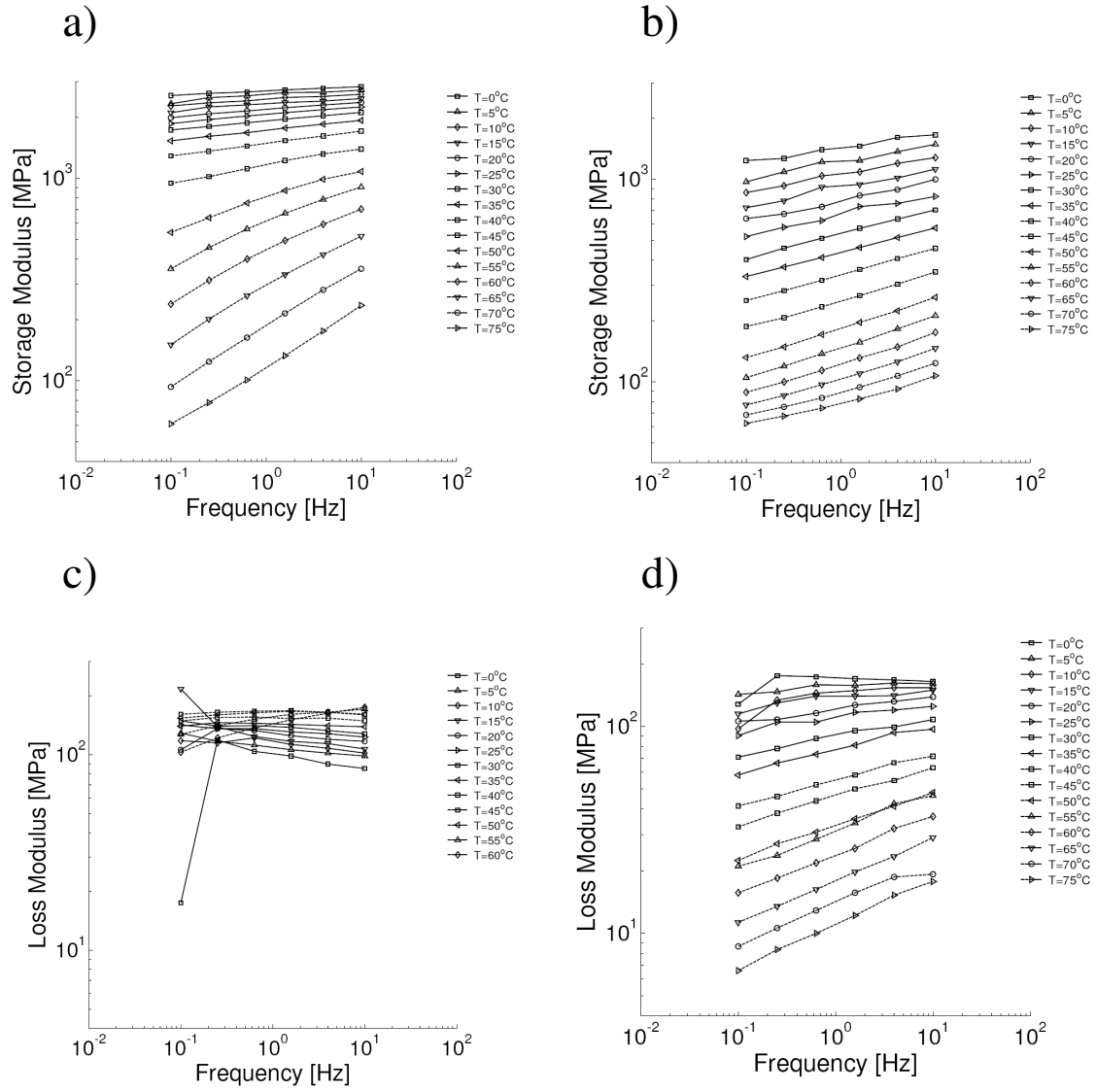
### 5.4.1. Macroscopic viscoelastic characterization

Figure 5.1 shows the storage and loss moduli obtained from the DMTA experiments at several temperatures. Master curves are obtained using the time-temperature superposition principle (see Figure 5.2). The shift factor  $a_T$  is determined to achieve the closest superposition and is found to obey the Williams- Landel -Ferry relation [32]:

$$\log(a_T) = \frac{-C_1(T - T_0)}{C_2 + T - T_0} \quad (5.12)$$

where  $C_1$  and  $C_2$  are constants, determined to be respectively 91 and 550 for the soft film and 100 and 523 for the hard film.  $T_0$  is the reference temperature at which the master curves are constructed (in our case 298 K for both materials). It is checked and confirmed that the vertical shift, applied to compensate for the elastic modulus change with temperature [33], is small and therefore the effect can be ignored [34].

The dynamic modulus obtained from DMTA is then subsequently converted into the time domain to obtain the relaxation modulus. This is done using the standard software package IRIS, and details of the method can be found in the work of Baumgartel and Winter [35-37]. The storage modulus and loss modulus master curves are first fitted using a Maxwell model (i.e. a spring and a dashpot in series) with twenty two modes for the hard material and twenty three modes for the soft material (see Table 5.1 in Appendix). Figure 5.2 represents the Maxwell fit of the experimental master curves. The relaxation modulus can be described using Equation 5.13:



**Figure 5.1:** DMTA results at several temperatures. Storage modulus obtained on a) hard material and b) soft material. Loss modulus obtained on c) hard material and d) soft material.

$$G(t) = \sum_k G_k \exp\left(-\frac{t}{\tau_k}\right) \quad (5.13)$$

where the relaxation times,  $\tau_k$ , and  $G_k$  are obtained from the fit of the dynamic measurements.

The storage  $G'$  and loss  $G''$  moduli can be inverted to obtain the corresponding compliance by:



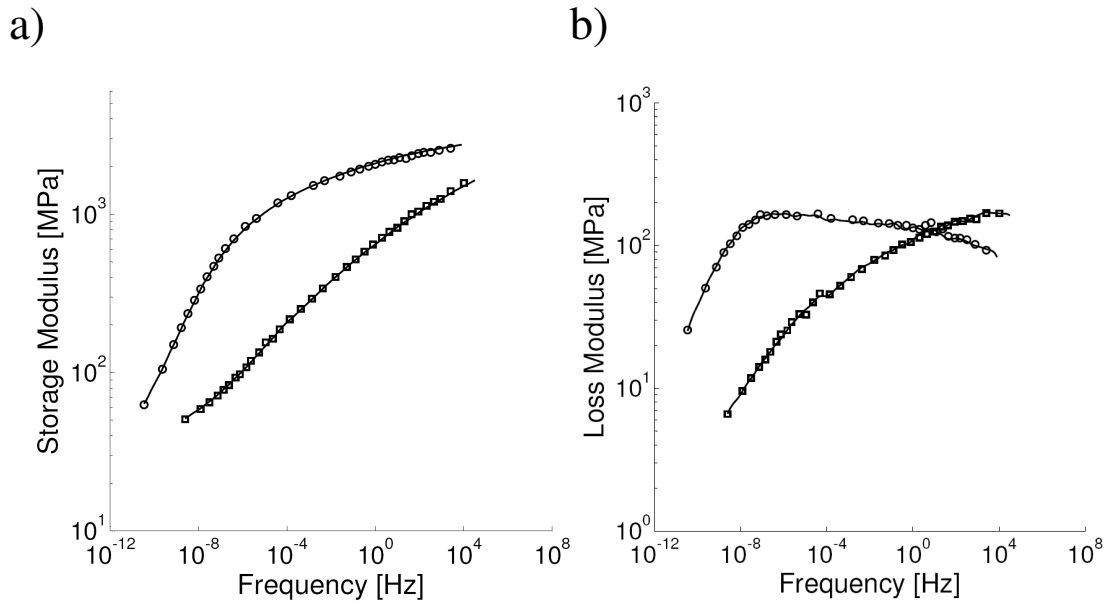


**Figure 5.2:** DMTA master curves fitted using a Maxwell model (solid lines) compared with the experimental curve for the hard material (○) and the soft material (□): a) storage modulus; b) loss modulus.

$$J'(\omega) = \frac{G'}{G'^2 + G''^2} \quad (5.14)$$

$$J''(\omega) = \frac{G''}{G'^2 + G''^2} \quad (5.15)$$

The storage and loss compliance can be fitted with a Kelvin-Voigt model (i.e. a spring and a dashpot in parallel) with twenty one elements for the hard material and twenty two elements for the soft material (see Table 5.2 in the Appendix). The results of the fit are given in Figure 5.3. The creep compliance can be described using:

$$J(t) = J_g + \sum_i J_i \left[ 1 - \exp\left(-\frac{t}{\tau_i}\right) \right] \quad (5.16)$$

where retardation times,  $\tau_i$ , and  $J_i$  are obtained from the fit of the dynamic measurement.

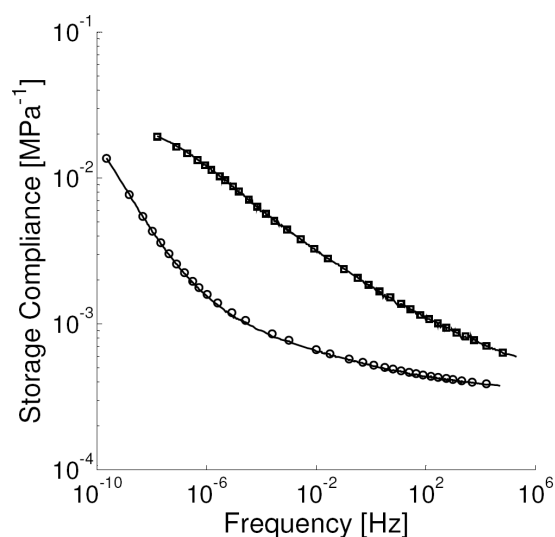


**Figure 5.3:** Storage compliance fitted using Maxwell model (solid lines) compared with the experimental curve for the hard material (○) and the soft material (□).

#### 5.4.2. Linear viscoelastic indentation

##### *Dynamic indentation*

In order to determine the tensile storage and loss moduli, dynamic indentation tests are performed on the two acrylate films. From the experimental data, consisting of the load and displacement amplitudes and the phase angle, the tensile storage and loss moduli are computed using Equations 5.10 and 5.11. Figure 5.4, presenting the tensile storage and loss moduli as a function of the frequency, shows that the method is sensitive enough to capture the frequency dependence of the moduli for the two acrylate films. Moreover, it is shown that the dynamic properties of each material, obtained at a depth of 100 nm are equal to those obtained at a depth of 400 nm. This indicates that the linear viscoelastic conditions are not violated. Finally, it is important to notice from Figure 5.4, that the experiments are reproducible (the experimental error is represented by the size of the symbols).

In order to validate the dynamic indentation analysis we compare the tensile dynamic properties obtained from the two methods: indentation and DMTA (see Figure 5.4). This figure shows that the frequency dependence of the storage and loss moduli are correctly captured by indentation for both the soft and the hard material. An exception seems to be the loss modulus, which is somewhat overestimated by the indentation tests. Quantitatively, the storage modulus obtained from the indentation technique differs from the DMTA results by 10-12% for the hard material and 3-7% for the soft material. The loss modulus obtained from indentation differs 8-15% from the DMTA results for the soft material and 5-40% for the hard material. The source of the discrepancy for the loss

modulus of the hard material might be due to the fact that the time dependence is not pronounced and thus more sensitive to the noise or limitation in the force measurement accuracy, rather than the surface detection or imprecise determination of the contact area.

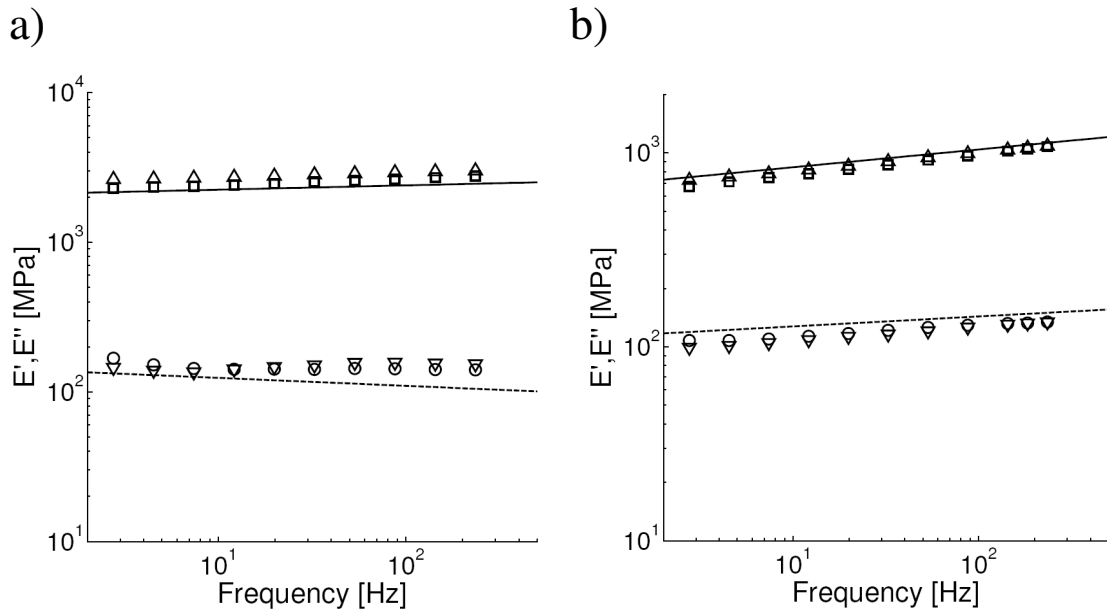


**Figure 5.4:** Indentation storage modulus obtained at a depth of 100 nm ( $\Delta$ ) and 400 nm ( $\square$ ) and loss modulus obtained at a depth of 100 nm ( $\nabla$ ) and 400 nm ( $\circ$ ) compared to the DMTA storage modulus (solid lines) and loss modulus (dashed lines) for a) the hard material and; b) the soft material. The size of the symbols corresponds to the experimental error.

### *Creep indentation*

Since the time dependence can also be represented in the time domain, quasi static indentation tests are performed. For indentation creep tests, typical creep responses are depicted in Figure 5.5. The creep response of the hard material is noisier and less reproducible than that of the soft material. A maximum noise of 20 nm in displacement is usually found. From the experimental data, the tensile creep compliance is computed using Equation 5.1. Figure 5.6 represents the experimental mean creep compliance obtained under two different forces for the hard material and the soft material. This figure shows that the method is sufficiently sensitive to capture the time dependence of the mechanical properties. Moreover, it is observed that the estimated creep compliance is hardly affected by the creep force. This supports the validity of the assumption of linear viscoelastic response in this particular range of forces and displacements. Additionally, it is also observed that the creep compliance remains unchanged with the indentation depth, indicating that for these values of the indentation depths the film thickness has no influence on the mechanical properties.

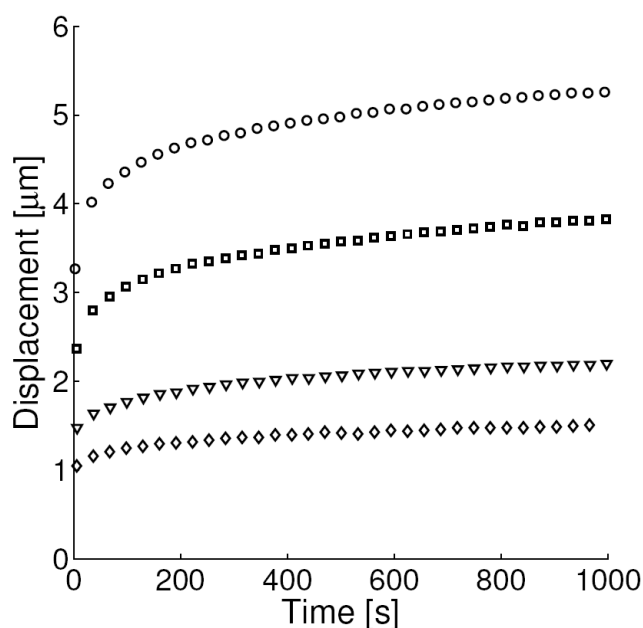


**Figure 5.5:** Indentation creep response for the hard material at a constant force of 30 mN (◇) and 50 mN (▽) and for the soft material at a constant force of 30 mN (□) and 50 mN (○).

The creep compliances predicted from indentation are compared with those obtained from the DMTA measurements in Figure 5.6. The time-dependent mechanical properties for the soft material are correctly determined by the indentation, since the slopes of the curves are the same. Moreover, the creep compliance predicted from the DMTA is always equal to that determined from the indentation, within the range of the experimental error. For the hard material, the comparison is less favorable since the time dependence is overestimated by the indentation, especially for longer times. A discrepancy of 5 to 35 % was found between the two methods. This difference can be explained by the limitation in accuracy of the force measurement by the indenter combined with the relatively small force change at long waiting times.

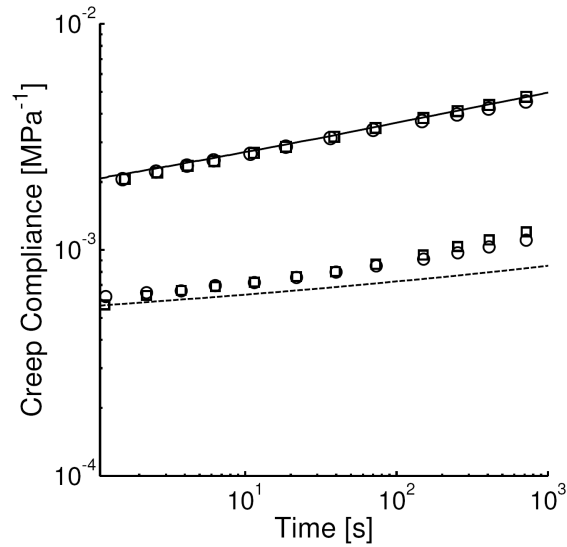


**Figure 5.6:** Indentation creep compliance obtained at a constant force of 30 mN (○) and 50 mN (□) compared with the DMTA prediction for the hard (solid line) and soft material (dashed line). The size of the symbols corresponds to the error.

#### *Relaxation indentation*

Complementary to the creep indentation tests, we also perform relaxation indentation tests, see Figure 5.7 that shows a typical stress relaxation response of the soft and the hard material. These stress relaxation experiments show less reproducibility than creep experiments. The noise level, measured during the experiments, was 2 mN. Since we already have shown for the creep indentation test, that the conditions for linear viscoelasticity are fulfilled in this particular range of forces and displacements, the relaxation compliance can be computed from the measured loads and displacements by using Equation 5.2. Figure 5.8 presents the results of the relaxation modulus plotted as function of time. The method is sufficiently sensitive to capture the time dependence of the mechanical properties, like for the creep tests. A direct comparison in Figure 5.8 shows that the tensile relaxation moduli obtained from indentation are in good agreement with those obtained from DMTA tests in a quantitative manner for the soft material. On the contrary, the relaxation modulus for the hard material from the DMTA is 4-18% higher than that obtained from indentation. Nevertheless, it still provides a satisfactory estimation of the relaxation modulus. Therefore, we can conclude that the relaxation moduli predicted from the indentation are in good agreement with those obtained from DMTA.

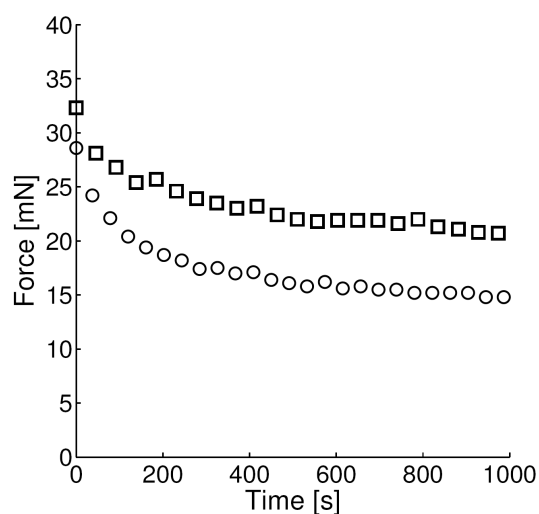


**Figure 5.7:** Indentation relaxation response for the hard (□) and soft (○) material.

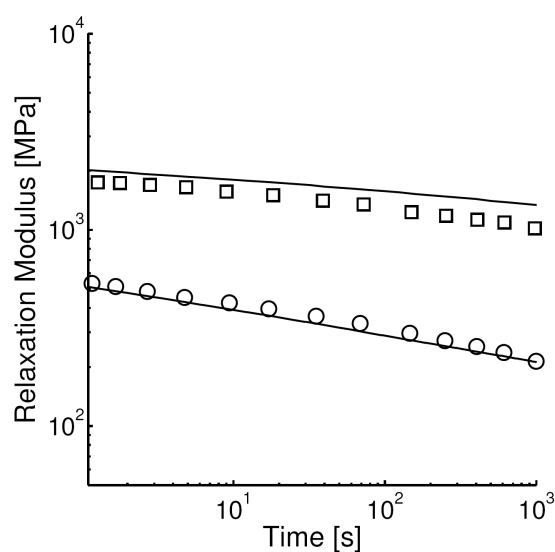


**Figure 5.8:** Indentation relaxation modulus (open symbols) compared with those derived from DMTA (solid lines), of the hard (□) and soft (○) material. The size of the open symbol corresponds to the error.

## 5.5. Conclusions

We have demonstrated that, in the linear viscoelastic regime, the mechanical properties determined by the instrumented indentation technique are comparable with those obtained from conventional DMTA testing. We have found a difference of about 10 %

between the results of indentation experiments and those of DMTA performed on a low-T<sub>g</sub> acrylate film for quasi-static and dynamic tests. The creep compliance and loss modulus for a higher-T<sub>g</sub> acrylate show deviations from the data obtained with DMTA, although the obtained result may still be satisfactory. The deviations can be explained by the fact that the hard material exhibits a less pronounced time-dependency than the soft material and therefore is more sensitive to experimental errors.

## References

- [1] A.C. Fischer-Cripps, *Nanoindentation*. Second ed. 2004: Springer.
- [2] K.L. Johnson, *Contact mechanics*, Cambridge University Press. 1985, Cambridge.
- [3] B.R. Lawn, A.G. Evans, and D.B. Marshall, *Elastic/plastic indentation damage in ceramics: the median/radial crack system*. J. Am. Ceram. Soc., 1980. **63**: p. 574-581.
- [4] G.R. Anstis, P. Chantikul, B.R. Lawn, and D.B. Marshall, *A critical evaluation of indentation techniques for measuring fracture toughness: I Direct crack measurements*. J. Am. Ceram. Soc., 1981. **64**: p. 533-538.
- [5] M.T. Laugier, *Palmqvist indentation toughness in WC-CO composites*. J Mater. Sci. Lett., 1987. **6**: p. 897-900.
- [6] R. Dukino and M.V. Swain, *Comparative measurement of indentation fracture toughness with Berkovich and Vickers indenters*. J. Am. Ceram. Soc., 1992. **75**: p. 3299-3304.
- [7] J.S. Field, M.V. Swain, and J.D. Dukino, *Determination of fracture toughness from the extra penetration produced by indentation pop-in*. J. Mater. Res., 2003. **18**: p. 1412-1416.
- [8] J.M.J. den Toonder, J. Malzbender, G. de With, and A.R. Balkenende, *Fracture toughness and adhesion energy of sol-gel coatings on glass*. J. Mat. Res., 2002. **17**(1): p. 224-233.
- [9] T.Y. Tsui, W.C. Oliver, and G.M. Pharr, *Influences of stress on the measurement of mechanical properties using nanoindentation. 1. Experimental studies in an aluminium alloy*. J. Mater. Res., 1996. **11**: p. 760-768.
- [10] A. Bolshakov, W.C. Oliver, and G.M. Pharr, *Influences of stress on the measurement of mechanical properties using nanoindentation. 2. Finite element simulation*. J Mater. Res., 1996. **11**: p. 760-768.

- 
- [11] Y.H. Lee and D. Kwong, *Residual stress in DLC/Si and Au/Si systems: Application of a stress -relaxation model to nanoindentation techniques*. J Mater. Res., 2002. **17**: p. 901-906.
- [12] J.G. Swadener, B. Taljat, and G.M. Pharr, *Measurement of residual stress by load and depth sensing indentation with spherical indenters*. J Mater. Res., 2001. **16**: p. 2091-2102.
- [13] E.H. Lee and J.R.M. Radok, *The contact problem for viscoelastic bodies*. Journal of Applied Mechanics, 1960. **30**: p. 438-444.
- [14] T.C.T. Ting, *The contact stresses between a rigid indenter and a viscoelastic half-space*. Journal of Applied Mechanics, 1966. **33**: p. 845-854.
- [15] T.C.T. Ting, *Contact problems in the linear theory of viscoelasticity*. Journal of Applied Mechanics, 1968. **35**: p. 248-254.
- [16] G.A.C. Graham, *The contact problem in the linear theory of viscoelasticity*. Int. J. of Eng. Sci., 1965. **3**: p. 27-46.
- [17] G.A.C. Graham, *The contact problem in the linear theory of viscoelasticity when the time dependent contact area has any number of maxima and minima*. Int. J. of Eng. Sci., 1967. **5**: p. 495-514.
- [18] G.A.C. Graham and J.M. Golden, *The three-dimensional steady-state viscoelastic indentation problem*. Int. J. of Eng. Sci., 1988. **26**: p. 121-126.
- [19] L. Cheng, X. Xia, W. Yu, L.E. Scriven, and W.W. Gerberich, *Flat punch indentation of viscoelastic material*. Journal of Polymer Science B: polymer physics, 2000. **38**(1): p. 10-22.
- [20] H. Lu, B. Wang, J. Ma, G. Huang, and H. Viswanathan, *Measurement of creep compliance of solid polymers by nanoindentation*. Mech. of Time-dependent Materials, 2003. **7**: p. 189-207.
- [21] Shuang Yang, Yong-Wei Zhang, and Kaiyang Zeng, *Analysis of nanoindentation creep for polymeric materials*. J. of App. Physics, 2004. **95**(7): p. 3655-3666.
- [22] M.L. Oyen, *Analytical techniques for indentation of viscoelastic material*. Phil. Mag., 2006. **86**(33-35): p. 5625-5641.
- [23] J.M.J. den Toonder, Y. Ramone, A.R. van Dijken, J.G.J. Beijer, and G.Q. Zhang, *Viscoelastic characterization of low-dielectric-constant SiLK films using nano-indentation in combination with finite element modeling*. Journal of Electronic Packaging, 2005. **127**: p. 267-285.
- [24] J.L. Loubet, W.C. Oliver, and B.N. Lucas, *Measurement of the loss tangent of low-density polyethylene with nanoindentation technique*. J Mater. Res., 2000. **15**: p. 1195-1198.
- [25] S.A.S. Asif, K.J. Wahl, and R.J. Colton, *Nanoindentation and contact stiffness measurement using force modulation with a capacitive load-displacement transducer*. Rev. Sci. Instrum., 1999. **70**(5): p. 2408-2413.



- 
- [26] J.L. Loubet, B.N. Lucas, and W.C. Oliver. *Conference proceedings: International workshop on instrumented indentation*. 1995. San Diego, NIST Spec. Publ. 896. p. 31-34.
- [27] B.N. Lucas, W.C. Oliver, and J.E. Swindeman. *The Dynamics of frequency specific depth-sensing indentation testing*. in *Spring MRS Meeting*. 1998. San Francisco, CA. **522**: p. 3-14.
- [28] M.R. Vanlandingham, N.-K. Chang, P.L. Drzal, C.C. White, and S.-H. Chang, *Viscoelastic characterization of polymers using instrumented indentation. I. Quasi-static testing*. J. Polym. Sci.: Part B: Polym Physics, 2005. **43**: p. 1794-1811.
- [29] C.C. White, M.R. Vanlandingham, P.L. Drzal, N.-K. Chang, and S.-H. Chang, *Viscoelastic characterization of polymers using instrumented indentation. II. Dynamic testing*. J. Polym. Sci.: Part B: Polym Physics, 2005. **43**(1812-1824).
- [30] W.C. Oliver and G.M. Pharr, *An improved technique for determining hardness and elastic-modulus using load and displacement sensing indentation experiments*. J Mater. Res., 1992. **7**(6): p. 1564 - 1583.
- [31] W.C. Oliver and G.M. Pharr, *Measurement of hardness and elastic modulus by instrumented indentation: Advances in understanding and refinements to methodology*. J. Mat. Res., 2004. **19**(1): p. 3-20.
- [32] L. Malcom, R. Williams, F. Landel, and J.D. Ferry, *The Temperature Dependence of Relaxation Mechanisms in Amorphous Polymers and Other Glass-forming Liquids*. J. Amer. Chem. Soc., 1955. **77**: p. 3701-3707.
- [33] J.D. Ferry, *Viscoelastic properties of polymers*. third ed. 1980, New York: Wiley.
- [34] I.M. Ward, *Mechanical properties of solid polymers*. 1971, New York: Wiley-Interscience.
- [35] M. Baumgartel and H.H. Winter, *Determination of discrete relaxation and retardation time spectra from dynamic mechanical data*. Rheol. Acta, 1989. **28**: p. 511-519.
- [36] M. Baumgartel and H.H. Winter, *Interrelation between continuous and discrete relaxation time spectra*. J. Non-Newtonian Fluid Mech., 1992. **44**: p. 15-36.
- [37] H.H. Winter, *Analysis of dynamic mechanical data: Inversion into a relaxation time spectrum and consistency check*. J. Non-Newtonian Fluid Mech., 1997. **68**: p. 225-239.

## Appendix

**Table 5.1:** Value for the Maxwell parameters.

Soft Material		Hard Material	
$G_k$ [Pa]	$\tau_k$ [s]	$G_k$ [Pa]	$\tau_k$ [s]
7.74E+07	4.13E-06	4.25E+07	2.28E-05
4.32E+07	1.80E-05	2.89E+07	1.13E-04
5.37E+07	6.67E-05	2.92E+07	4.65E-04
3.29E+07	9.97E-04	3.54E+07	1.63E-03
4.41E+07	2.50E-04	3.16E+07	8.15E-03
4.52E+07	2.74E-03	4.06E+07	2.52E-02
3.22E+07	1.45E-02	5.39E+07	1.43E-01
2.51E+07	2.89E-02	5.79E+07	1.10E+00
3.68E+07	1.03E-01	5.21E+07	3.37E+01
3.43E+07	5.52E-01	4.92E+07	6.20E+00
2.86E+07	2.64E+00	5.17E+07	7.38E+02
2.16E+07	4.01E+01	5.99E+07	4.34E+03
1.53E+07	1.51E+02	5.68E+07	2.20E+04
1.53E+07	5.59E+02	5.85E+07	1.22E+05
1.77E+07	3.50E+03	5.57E+07	5.85E+05
1.11E+07	1.88E+04	5.52E+07	2.78E+06
8.41E+06	8.14E+04	5.00E+07	1.48E+07
2.05E+07	1.03E+01	3.21E+07	8.20E+07
6.35E+06	3.95E+05	1.96E+07	4.30E+08
4.59E+06	1.80E+06	4.62E+07	1.66E+02
3.34E+06	8.37E+06	1.18E+07	2.61E+09
3.03E+06	4.88E+07	1.81E+07	1.15E+11
1.59E+07	7.79E+09		

**Table 5.2:** Value for the Kelvin-Voigt parameters.

Soft Material		Hard Material	
$J_i$ [Pa <sup>-1</sup> ]	$\tau_i$ [s]	$J_i$ [Pa <sup>-1</sup> ]	$\tau_i$ [s]
2.31E-10	4.72E-06	4.97E-11	2.38E-05
1.68E-10	1.96E-05	3.70E-11	1.17E-04
2.58E-10	7.51E-05	3.96E-11	4.81E-04
2.75E-10	2.79E-04	5.30E-11	1.70E-03
2.27E-10	1.09E-03	4.94E-11	8.48E-03
4.46E-10	3.16E-03	7.27E-11	2.66E-02
3.25E-10	1.60E-02	1.09E-10	1.54E-01
4.14E-10	3.21E-02	1.36E-10	1.20E+00
7.35E-10	1.22E-01	1.38E-10	6.73E+00
9.22E-10	6.60E-01	1.74E-10	3.71E+01
1.10E-09	3.15E+00	1.85E-10	1.82E+02
1.12E-09	1.20E+01	2.58E-10	8.29E+02
1.64E-09	4.86E+01	3.77E-10	5.05E+03
1.70E-09	1.78E+02	5.01E-10	2.61E+04
2.53E-09	6.82E+02	7.17E-10	1.50E+05
4.40E-09	4.65E+03	1.07E-09	7.51E+05
4.76E-09	2.38E+04	1.89E-09	3.89E+06
6.06E-09	1.02E+05	3.77E-09	2.34E+07
7.02E-09	4.90E+05	6.46E-09	1.33E+08
7.81E-09	2.18E+06	1.18E-08	7.20E+08
8.24E-09	9.90E+06	2.40E-08	4.52E+09
1.08E-08	5.85E+07		

## **Chapter 6**

### **Conclusions and recommendations**

---

## 6.1. Conclusions

Mechanical properties of materials are usually determined using macroscopic tensile or compression tests. Instrumented indentation testing represents an alternative in the case that the latter cannot be used, for example for thin films or small specimens. In this thesis we studied the ability of instrumented indentation testing to determine mechanical properties of polymers. As a verification test, we compared indentation results to those of macroscopic tests. Three main topics were considered: the practical issue of misalignment between indenter and sample, characterization of the large deformation properties of glassy polymers, and the estimation of linear viscoelastic properties from indentation.

The influence of misalignment on the indentation has been presented in Chapter 2. It was found that misalignment is important only for the flat punch indenter where the stiffness measured decreases with an increasing misalignment angle. By using a specially designed alignment tool, we were able to perfectly quantify and correct the misalignment regardless of the different tip geometry and the origin of the misalignment. This is a major practical requirement for sound flat-punch indentation experiments.

In Chapter 3 indentation experiments have been combined with numerical simulations to probe glassy polymers in the large deformation, plastic, regime. The flat-tip micro-indentation response, obtained on two materials (polycarbonate and poly(methyl methacrylate)) at various loading speeds and thermal histories, was numerically predicted using a constitutive model, that quantitatively captures intrinsic behavior of glassy polymers. In the model, a single parameter, the state parameter  $S_a$ , is used to uniquely determine the initial yield stress of the material, incorporating all variations in its thermal history. For PC the yield stress increases proportionally with the logarithm of strain-rate, whereas for PMMA, a characteristic change in slope can be observed at higher strain rates. We demonstrate that the flat-tip indentation response at different indentation speeds can be described accurately for both materials. Moreover, it is shown that the parameter set obtained for each material is also representative for the mechanical response on a *macroscopic* scale. This implies that the thermodynamic state of PC and PMMA can now be determined by fitting a single parameter on a single indentation test. Moreover, it was found that the pressure dependence of the yield stress can also be obtained by combining indentation tests and compression tests on the same samples.

The development of contact area during indentation tests of glassy polymers has been studied in Chapter 4 using the combination of numerical modeling and an optical indentation microscope enabling the *in-situ* measurement of the contact area. It is shown that the model can perfectly predict the development of the contact area. Furthermore, we found that the contact area follows the Hertz theory at small indentation depth from which it gradually deviated when plastic deformation occurs. In addition to this, numerical simulation showed that the pile-up which occurs at large deformations results from localization effects and is therefore promoted by strain softening. Strain hardening, on the contrary, tends to promote sink-in.

In Chapter 5 we have shown that the linear viscoelastic properties of polymers, at small deformations, can be determined from instrumented indentation testing. The results obtained from both quasi-static and dynamic indentation measurements turned out to agree favourably with results obtained from conventional DMTA testing.

## 6.2. Recommendations

The constitutive model used in this thesis has been developed to describe large strain deformation of polymers and thus, in the present single mode version, the small deformation pre-yield regime is not very well represented. Stress and strain are linearly related through an elastic modulus and no time dependence is incorporated. The elastic modulus used to simulate the macroscopic tests, is tuned in order to correctly describe the yield strain and due to this it is lower than the generally accepted value. Chapter 3 shows that for indentation, this value has to be increased to correctly describe the indentation tests. However, using this approach, the unloading curve is not correctly described. Therefore a model that combines a viscoelastic multimode approach with the viscoplastic implementation is needed to fully describe both the loading and the unloading curves. The straightforward extension of the present single mode approximation to multi-mode, as previously proposed by Tervoort *et al.* [1], performed well in describing the non-linear viscoelastic response of polycarbonate and its implementation would be a significant improvement in modeling indentation.

In Chapter 3, the indentation load-displacement curves were used to determine only the state parameter,  $S_a$  which takes into account the thermal history dependence of the yield stress and the pressure dependence parameter  $\mu$ . Parameters that cover the rate dependence were determined from macroscopic compression tests. The next step should be to fully characterize the material from the indentation experiments. For instance, indentation tests at different speeds could be used to determine the rate dependence of the yield stress if performed on the rejuvenated state material. In addition, different tip geometries could be combined. This would allow the determination of the pressure dependence parameter using only indentation tests.

It has been proved that the indentation data set is equivalent to the data set generated by macroscopic tests when performed on bulk materials. Very thin films as well as small volumes of material are known to exhibit size effects, i.e. their material properties deviate from bulk properties. Since we have proven the soundness of instrumented indentation for determining bulk mechanical properties, as a next step indentation on thin films or small volumes of material could be performed with confidence in order to study in detail length scale effects.

## References

- [1] T.A. Tervoort, E.T.J. Klompen, and L.E. Govaert, *A multi-mode approach to finite, three-dimensional, nonlinear viscoelastic behaviour of glassy polymer*. J. Rheol., 1996. **40**: p. 779-797.



## Samenvatting

---

Geïnstrumenteerde indentatie is een techniek die lokaal mechanische eigenschappen van films en/of bulkmaterialen meet. Een indenter met een goed gedefinieerde geometrie wordt in het oppervlak van een materiaal gedrukt, terwijl indentatiekracht én penetratiediepte worden gemeten. Mechanische eigenschappen zoals elasticiteitsmodulus en vloeispanning kunnen uit deze data worden bepaald. Vooral bij toepassing op polymeren wordt deze analyse echter belemmerd doordat zowel het contactoppervlak als de indringdiepte niet voldoende nauwkeurig bekend zijn. Kwantitatieve analysemethoden ontbreken. Dit proefschrift beschrijft de ontwikkeling van een numeriek-experimentele methodologie voor de kwantitatieve interpretatie van indentatie-metingen op polymere materialen.

Het proefschrift bestaat uit twee delen. In het eerste deel concentreren wij ons op de karakterisering van het deformatiegedrag van glasachtige polymeren bij hoge rekken, in het bijzonder poly(carbonaat) (PC) en poly(methylmethacrylate) (PMMA). Indentatie experimenten werden uitgevoerd met een vlakke indenter, omdat hiermee de overgang van het elastische naar het plastische gebied duidelijk tot uiting komt in de gemeten kracht-diepte relatie. De bestaande indentatie-opstelling is uitgebreid met een nieuw ontworpen module waarmee de uitlijning van de indenter ten opzichte van het materiaaloppervlak nauwkeurig kan worden ingesteld, waardoor het contactoppervlak constant is tijdens de gehele meting. De module maakt het tevens mogelijk de invloed van scheefstand van indenter ten opzichte van materiaal te analyseren, hetgeen belangrijk is voor de interpretatie van resultaten verkregen met standaard indentatiemethodes.

In het plastisch deformatiegebied vertonen glasachtige polymeren een complex intrinsiek gedrag; de vloeispanning is in sterke mate afhankelijk van druk en deformatiesnelheid en het *post-yield* gedrag vertoont zowel *strain softening* als *strain hardening*. Teneinde het indentatieproces numeriek te voorspellen gebruiken we het in onze onderzoeksgroep door de jaren heen ontwikkeld constitutief model dat het intrinsieke deformatiegedrag kwantitatief beschrijft. Het model bevat slechts één parameter, de toestandsparameter  $S_a$ , om de initiële vloeispanning, en dus de leeftijd, van het polymeer te kwantificeren, daarbij de volledige thermische geschiedenis van het materiaal meenemend. Er zijn vlakke indentatiemetingen, bij verschillende deformatie snelheden, uitgevoerd op PC en PMMA, met verschillende thermische geschiedenissen. De vloeispanning van PC neemt evenredig toe met de logaritme van reksnelheid (thermoreologisch eenvoudig gedrag). PMMA laat een kenmerkende verandering in helling zien voor hogere reksnelheden (thermoreologisch complex gedrag). Wij tonen aan dat, met een juiste definitie van de viscositeitsfunctie, indentatiemetingen bij



verschillende snelheden nauwkeurig kunnen worden beschreven voor beide materialen. De aldus verkregen materiaalparameters beschrijven tevens het *macroscopisch* deformatiegedrag van de polymeren. Dit impliceert dat de thermodynamische toestand van PC en PMMA kan worden beschreven door één enkele parameter, bepaald uit één enkele indentatiemeting.

De ontwikkeling van het contactoppervlak is bestudeerd gebruikmakend van een optische microscoop uitgerust met een indentatie set-up en een bolvormige indenter. Het numerieke model voorspelt deze ontwikkeling correct, zowel in het elastische als in het plastische deformatiegebied, met inbegrip van de invloed van thermische geschiedenis en deformatiesnelheid. Ophoping van materiaal rondom de indenter wordt veroorzaakt door lokalisatie-effecten en wordt bevorderd door *strain softening*.

Het tweede deel van het proefschrift behandelt de karakterisering van lineaire viscoelastische eigenschappen van polymeren gebruikmakend van dynamische indentatie. Gebruikmakend van een Berkovich indenter zijn metingen uitgevoerd op twee acrylaat films met een groot verschil in glasovergangstemperatuur. De dynamische eigenschappen aldus gemeten zijn in overeenstemming met macroscopische DMTA metingen. Met het lineair-viscoelastische correspondentie-principe worden de verkregen relaxatietijdspectra gebruikt voor het kwantitatief voorspellen van kruip en spanningsrelaxatie tijdens indentatie zoals gemeten met een bolvormige indenter.

## Acknowledgement

---

This thesis is based on work carried out at Department of Mechanical Engineering, Technical University Eindhoven. Herewith I would like to take this opportunity to express my gratitude to a number of people for their work and support:

Dr. Ir. Leon Govaert for his supervision, deep involvement and guidance throughout my work.

Prof. Dr. Ir. Jaap den Toonder for his supervision, constant support and discussions.

Prof. Dr. Ir. Han Meijer, for his important support and constructive criticism.

All co-authors of the papers presented in this thesis. Special thanks are given to Tom Engels, Lambert van Breemen and Roel Janssen for their important contribution with regard to the Chapter 3.

Excellent working atmosphere and collegiality between the members of the Polymer Technology group were very much appreciated.



## Curriculum Vitae

---

Christophe G.N. Pelletier  
born in Saint-Rémy, France  
on June 12, 1975

1993                      High School “Lycée Polyvalent Mathias”, Chalon-Sur-Saône,  
France

1999:                      University of Bourgogne, Dijon, France  
Bachelor’s Degree in Physical Chemistry  
Project: *Study of organic crystals growth and characterization by AFM,*  
University of Nijmegen, The Netherlands

2001                      DESS University of Lille 1, France,  
Master’s Degree in Material’s Science  
Project: *State-of-the-art on thermo-mechanical characterization of*  
*polymer thin films*, Philips Semiconductors, Nijmegen, The Netherlands

2002-2007                PhD, Section Materials Technology, Department of Mechanical  
Engineering , Eindhoven University of Technology  
Project: *Mechanical characterization of glassy polymers using*  
*instrumented indentation.*



## List of publications

---

### Refereed journal publications:

J. Baranowska, S.E. Franklin, C.G.N. Pelletier, *Tribological behaviour and mechanical properties of low temperature gas nitrided austenitic steel in relation to layer morphology*, *Wear*, 2005, 259 (1-6), p. 432-438.

C.G.N. Pelletier, E.C.A. Dekkers, L.E. Govaert, J.M.J. den Toonder, H. E. H. Meijer, *The effect of the indenter-surface misalignment on the indentation results*, *Polymer Testing*, **26**(7), 949-959, (2007).

C.G.N. Pelletier, J.M.J. den Toonder, L.E. Govaert, N. Hakiri, M. Sakai, *Quantitative assessment and prediction of the contact area development during spherical tip indentation of glassy polymers*, submitted to *Philosophical Magazine*.

C.G.N. Pelletier, P.A.M. Steeman, L.E. Govaert, J.M.J. den Toonder, H.E.H. Meijer, *Viscoelastic film properties determined using indentation and conventional testing: a comparison*, to be submitted to *Polymer Testing*.

C.G.N. Pelletier, L.C.A. van Breemen, T.A.P. Engels, R.P.M. Janssen, L.E. Govaert, J.M.J. den Toonder, *Numerical simulation of flat-tip micro-indentation of glassy polymers: influence of loading speed and thermodynamic state*, to be submitted.

### Refereed proceedings:

C.G.N. Pelletier, H.J.L. Bressers, G.Q. Zhang, K.M.B. Jansen, V. Gonda, L.J. Ernst, *The State-of-the-art of thermo-mechanical characterisation of thin polymer films*, in 3rd International Conference on Benefiting from Thermal and Mechanical Simulation in (Micro)-Electronics, Paris, Cercle Républicain, France, 293-300, (2002).

C.G.N. Pelletier, H.G.H. van Melick, L.E. Govaert, H.E.H. Meijer, *Micro- and Nano-indentation as a probe for mechanical properties of glassy polymers*, in 12th International Conference on Deformation, Yield and Fracture of Polymers, Cambridge, Churchill College, United Kingdom, 265-268, (2003).

C.G.N. Pelletier, T.A.P. Engels, L.C.A. van Breemen, L.E. Govaert, J.M.J. den Toonder, *Predicting the macroscopic response of glassy polymers using flat-tip micro-indentation*, in 13th International Conference on Deformation, Yield and Fracture of Polymers, Rolduc Abbey, Kerkrade, The Netherlands, 479, (2006).

